RETINAL VESSEL SEGMENTATION USING TEXTONS

LEI ZHANG

A thesis submitted to the University Of East Anglia School Of Computing Sciences in fulfilment of the requirements for the degree of Doctor of Philosophy.

© This copy of the thesis has been supplied on condition that anyone who consults it is understood to recognise that its copyright rests with the author and that no quotation from the thesis, nor any information derived therefrom, may be published without the author's prior written consent.

Abstract

Segmenting vessels from retinal images, like segmentation in many other medical image domains, is a challenging task, as there is no unified way that can be adopted to extract the vessels accurately. However, it is the most critical stage in automatic assessment of various forms of diseases (e.g. Glaucoma, Age-related macular degeneration, diabetic retinopathy and cardiovascular diseases etc.). Our research aims to investigate retinal image segmentation approaches based on textons as they provide a compact description of texture that can be learnt from a training set. This thesis presents a brief review of those diseases and also includes their current situations, future trends and techniques used for their automatic diagnosis in routine clinical applications. The importance of retinal vessel segmentation is particularly emphasized in such applications. An extensive review of previous work on retinal vessel segmentation and salient texture analysis methods is presented. Five automatic retinal vessel segmentation methods are proposed in this thesis. The first method focuses on addressing the problem of removing pathological anomalies (Drusen, exudates) for retinal vessel segmentation, which have been identified by other researchers as a problem and a common source of error. The results show that the modified method shows some improvement compared to a previously published method. The second novel supervised segmentation method employs textons. We propose a new filter bank (MR11) that includes bar detectors for vascular feature extraction and other kernels to detect edges and photometric variations in the image. The *k*-means clustering algorithm is adopted for texton generation based on the vessel and non-vessel elements which are identified by ground truth. The third improved supervised method is developed based on the second one, in which textons are generated by *k*-means clustering and texton maps representing vessels are derived by back-projecting pixel clusters onto hand labelled ground truth. A further step is implemented to ensure that the best combinations of textons are represented in the map and subsequently used to identify vessels in the test set. The experimental results on two benchmark datasets show that our proposed method performs well compared to other published work and the results of human experts. A further test of our system on an independent set of optical fundus images verified its consistent performance. The statistical analysis on experimental results also reveals that it is possible to train unified textons for retinal vessel segmentation. In the fourth method a novel scheme using Gabor filter bank for vessel feature extraction is proposed. The

method is inspired by the human visual system. Machine learning is used to optimize the Gabor filter parameters. The experimental results demonstrate that our method significantly enhances the true positive rate while maintaining a level of specificity that is comparable with other approaches. Finally, we proposed a new unsupervised texton based retinal vessel segmentation method using derivative of SIFT and multi-scale Gabor filers. The lack of sufficient quantities of hand labelled ground truth and the high level of variability in ground truth labels amongst experts provides the motivation for this approach. The evaluation results reveal that our unsupervised segmentation method is comparable with the best other supervised methods and other best state-of-the-art methods.

Acknowledgements

First and foremost, I wish to express my deepest gratitude to my supervisor Dr Mark Fisher who has been a tremendous mentor for me. You gave me the encouragement, motivation and understanding to start my Ph.D. research and undertake this challenging task.

I would like to thank and express my big gratitude to my co-supervisor Dr Wenjia Wang for his patient guidance and valuable support. I appreciate all his contributions of time, and advices to make my research experience substantial and efficient.

I would like to thank Dr Tim Morris, Manchester University and colleagues at Manchester Royal Eye Hospital for allowing us to use the MREH fundus image data set.

I would also like to thanks my best friend Zhi for the memorable moments shared with me.

Finally, but not the least, I would like to express my special thanks to my parents, father-in-law and mother-in law for all their love and encouragement. No words can express how grateful I am to my parents for all of the sacrifices that you've made on my pursuits. And most of all for my loving, supportive wife Yuan whose constant support during the period of my study is so appreciated.

Lei Zhang

University of East Anglia

June 2014

Publications

[1] M. Fisher, L. Zhang, An improved method of blood vessel segmentation in retinal images, *International Journal of Computer Assisted Radiology and Surgery*, vol. 7, pp. s361-s362, 2012.

[2] L. Zhang, M. Fisher and W. J. Wang, Compensating for Drusen in Retinal Vessel Segmentation, In 16th Conf. on Medical Image Understanding and Analysis, pp.185-190, 2012.

[3] L. Zhang, M. Fisher, W. J. Wang, Locating blood vessels in retinal images using unified Textons, In 17th Conf. on Medical Image Understanding and Analysis, pp. 213-218, 2013.

[4] L. Zhang, M. Fisher and W. J. Wang, Retinal vessel segmentation using Gabor filter and textons, In 18th Conf. on Medical Image Understanding and Analysis, pp.155-160, 2014.

[5] L. Zhang, M. Fisher and W. J. Wang, Comparative performance of texton based vascular tree segmentation in retinal images, in IEEE international conference on image processing, pp.952-956, 2014.

[6] L. Zhang, M. Fisher and W. J. Wang, A new texton based retinal vessel segmentation method using Gabor filter and Derivative of SIFT, *computerized medical imaging and graphics*, 2014. Submitted

Glossary

A/V ratio: vein/artery ratio

AMD: Age-related Macular Degeneration

AUC: The Area Under the Curve

C/D ratio: Optical Cup/Disc ratio

CAD: Computer-Assisted Diagnostic

CCD: Charge-Coupled Device

CMF: Classic Matched Filter

DHHS: The U.S. Department of Health and Human Services

DMD: Dry Macular Degeneration

DME: Diabetic Macular Edema

DoG: Difference of Gaussian

DR: Diabetic Retinopathy

FPF: False Positive Fractions

GLCM: Grey Level Co-occurrence Matrix

IOP: Intraocular Pressure

IRMA: Intra-Retinal Microvascular Abnormality

LBP: Local Binary Pattern

MA: Microaneurysms

MRF: Markov random fields

MRI: Magnetic resonance imaging

OD: Optic Disc

ONH: Optic Nerve Head

ROC: Receiver Operating Characteristic curves

SIFT: Scale Invariant Feature Transform

SLO: Scanning Laser Ophthalmoscopy

TPF: True Positive Fractions

WHO: World Health Organization

WMD: Wet Macular Degeneration

Contents

List of Figures

List of Tables

CHAPTER 1

1. Introduction

1.1 Overview

In recent decades, the assessment of retinal images has become increasingly important in early medical diagnosis of several diseases such as diabetes, hypertension and cardiovascular disease etc. [2]. Images of the ocular fundus are now routinely captured during retinal examinations as they allow pathological changes of retinal vasculatures such as diameter, length, and branching angle to be measured as these features, together with other anomalies enable clinical experts to diagnose and assess the progression of a range of diseases [2]. Because of this, the routine screening of these images is viewed as particularly important but human assessment of retinal vessels and the detection of anomalies is a skilled time consuming task [1]. For instance, diabetic retinopathy (DR) is a serious eye disease that affects the vision of patients with diabetes and even causes adult blindness by affecting and damaging the retinal vasculature structures inside the eye. However, it's hard to detect DR in its early stage until vision loss occurs. Imaging and analysing the optic fundus of patients at regular intervals, is one solution that could prevent this by detecting the changes of retinal vessels and treating the disease at an early stage. Computer based assessment of retinal vessels is seen as an important tool in undertaking population-based diagnoses of DR and this has motivated research into automatic assessment techniques.

Many automatic assessment procedures initially require the segmentation of the vessels from the background and this task plays a very important role in the success of the subsequent computer assisted diagnosis stages. It is a crucial stage which produces basic material that can be analysed and assessed. The completeness and accuracy of vessel segmentation determines the practicality of automated detection of relative diseases (see sub-section 1.2.4). However, in practice, automatic accurate retinal vessel segmentation is still a great challenge because of the complex nature of fundus images and effects such as noise,

low contrast between vessels (capillaries) and background, some abnormal regions (pathologies), illumination (vessel reflection), the variety of vessel structures (different width, length, cross) etc. All of these factors may influence the accuracy of segmentation. For instance, low contrast between the capillaries and the background could result in a failure to detect smaller capillaries or some abnormal non-vessel objects (exudates) to be segmented as vessels.

Our research aims to design and develop accurate retinal vessel automatic segmentation approaches based upon investigating texture analysis techniques. The motivation of our research focuses on structural texture analysis techniques using textons as we have found this approach to be under represented in the retinal vessel segmentation methods published within this research specialism. Work elsewhere in computer vision has demonstrated the advantages of using texture in providing significant information to distinguish the various patterns that present different visual features. For example, texture based segmentation methods in natural image segmentation and feature analysis has been widely studied and researchers have achieved some successes on problems of content based image retrieval. With this in mind, we believe that this research makes a significant contribution in filling a gap in the retinal vessel segmentation research field by investigating structure based texture analysis techniques (textons) to achieve accurate retinal vessel segmentation. This thesis particularly focuses on investigating texton-based approaches which have been a significant branch of texture analysis process since the term *texton* was introduced by Julesz in the 1980's [3].

In the following sections, we introduce the background relating to retinal vessel segmentation and include knowledge of the optical fundus image and descriptions of elements in retinal images relevant to vessel network segmentation. We also describe the diagnosis of common diseases using analysis of retinal fundus images followed by corresponding reviews of automated disease detection techniques using fundus images in recent years emphasizing the importance of retinal vessel segmentation in automated computer aided diagnosis system. Finally the corresponding contributions of the research are summarized and the overall outline of the thesis is described.

1.2 Retinal images

1.2.1 Eye Anatomy

This thesis focuses on the retina. Firstly, we describe eye anatomy related background knowledge. Figure 1.1 illustrates a brief review of eye structure. The visible parts of eye have a number of components which include cornea, sclera, iris, pupil, lens, vitreous body, retina, optic nerve and choroid. The cornea looks like a clear window at the front of the eye which allows light to transmit into the eye. The sclera is normally known as the 'white of the eye' and forms a part of the supporting wall of the eyeball. The iris is a colored circular muscle. It regulates the amount of light that is allowed to enter the eye by controlling the size of pupil, depending on the intensity of incoming light.

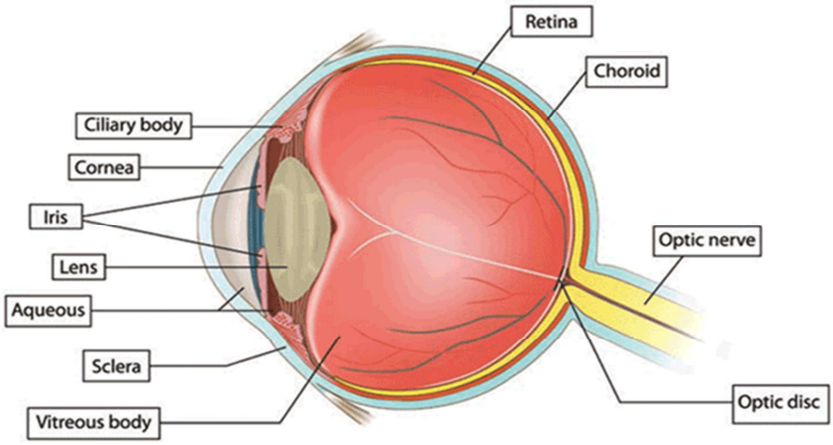

Figure 1.1 Cross sectional illustration of eye structures.[4]

The lens is a transparent structure that converges and focuses light waves onto the retina. The vitreous body fills the middle of eye between the lens and retina. It is filled with a viscous substance. The retina is the nerve layer that lines the back of eye. Here, light impulses are sensed and changed into electrical signals that are sent though the optic nerve to the brain. In the center of the retina, there is a small and highly light-sensitive yellow spot, which is known as the macula. It's a critical part of retina responsible for transforming the light into a nerve signal. The fovea is located near the center of the macula and responsible for detailed central and high resolution vision. The optic nerve transfers the electrical signals generated by the retina to the visual cortex of the brain. All of these components form three

different layers: the external layer is formed by the sclera and cornea, the intermediate layer is formed by the iris, ciliary body and choroid, the internal layer is the retina [5].

The process of vision is described as follows. Light waves enter the eye first through the cornea (external layer), the light then focus through the pupil, the size of it is controlled by the iris (intermediate layer). The light is directed by the pupil to the lens, which focuses the light and projects it on the retina (internal layer); the retina forms the light into electrical signals sent to cortex of the brain though the optic nerve.

Many prevalent diseases can be studied by analyzing pathological information extracted from the internal layer (retina), such as diabetic, diabetic retinopathy, glaucoma, and cardiovascular disease [2]. Hence visualisation of the retina has attracted great interest for a long time. Due to the availability of digital fundus cameras retinal imaging techniques have developed rapidly during the past several decades.

1.2.2 Fundus imaging

Since the appearance of features on the retina allows detection of diseases that may cause visual loss, such as diabetic retinopathy, and because records of their structural change over time provides objective evidence on the progression of the disease and response to treatment techniques for capturing and analysing images of the retina fundus have attracted great interest amongst scientists and researches during the past years. Today, techniques for imaging the eye are based upon the achievement of Gullstrand who first developed the fundus camera in 1910 [7]. The concept of fundus photography is still used to guide development of recent fundus imaging techniques. Fundus imaging is the procedure for capturing the components (such as retina, optic disc, macula, fovea et.al.) on the internal surface of eyeball [8]. Technically speaking, fundus imaging is the process whereby the 3D internal surface of eyeball is represented as a 2D object projected onto the imaging plane using reflected light [9]. Because of its cost-efficiency, fundus imaging is now commonly adopted in ophthalmology departments as a primary method of retinal imaging [10]. The following modes or techniques are representative categories of fundus imaging.

- **Fundus photography**: Images are obtained by a fundus camera which is equipped with a specialized low power microscope and an attached camera [22]. The basis of using fundus camera is that the imaging light and the corresponding reflectance of the retina can pass

through the pupil in both directions, thus an image of the inside of the eye can be obtained. Images captured by fundus cameras depend on the optical angle of acceptance of the lens. The normal angle of view is 30° which results in an image magnification of approximately 2.5 times. For wider optical angles between 45°-140° the magnification is less [22]. Traditionally, fundus cameras were used for mydriatic photography, so-called because the patient's pupil needs to be dilated using mydriatic eye drops before the retina is photographed. But recently, non-mydriatic fundus cameras have been developed. These cameras enable high quality images to be obtained and are particularly useful for imaging some diabetic patients whose pupils cannot be fully dilated using mydriatic eye drops.

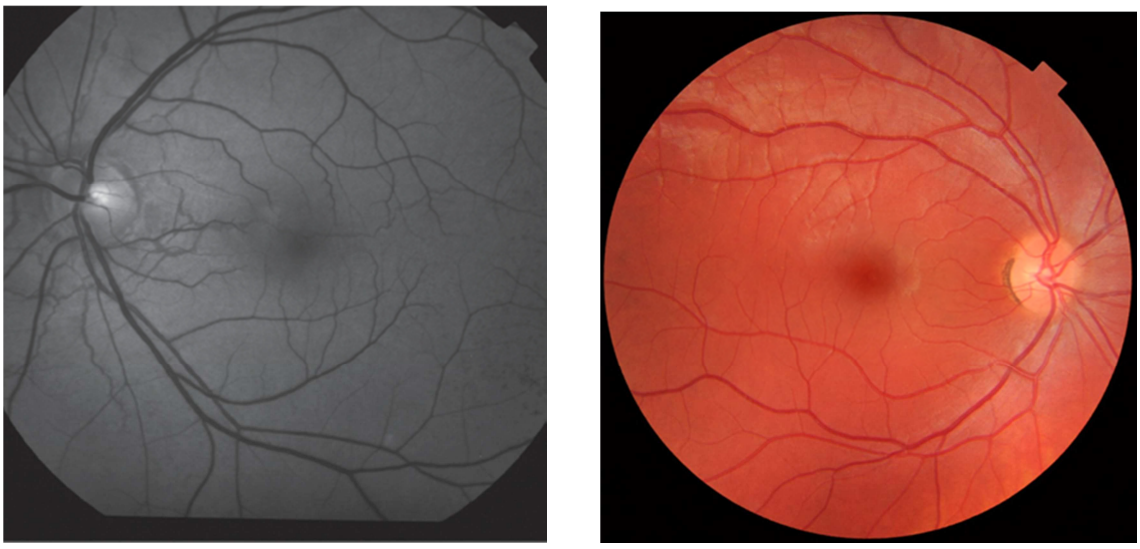

(a) (b)

Figure 1.2 Fundus photographs of normal eyes. (a) A red-free fundus image (left eye) [12]; (b) A colour fundus image (right eye) [11].

Two modalities of fundus photography denoted colour and grey modes (also known as red free) are available. Conventional, red-free fundus photography uses 35 mm film which is subject to special colour filter operations to improve contrast between vessels and other structures. Recently, superior digital images can be obtained using a charge-coupled device (CCD) as the imaging sensor. Colour fundus photography senses three channels; red, green and blue (R G B) of reflected light which are determined by the spectral sensitivity of the sensor [9]. Figure 1.2 (a) illustrates a red-free fundus image of a normal left eye, (b) is an example of a colour fundus image of the right eye obtained from a healthy 25-year old male volunteer.

- **Stereo fundus photography**: stereo-imaging techniques use two or more images captured at different angles to generate depth information of the object's surface, represented using 3-dimensional coordinates (x, y, z). The images can either be captured simultaneously using a specialised fundus camera, or can be collected sequentially by using a standard retinal fundus camera [13]. Stereo fundus imaging is particularly useful for diagnosing and monitoring the pathology of glaucoma (see section 1.2.4). Its clinical use has been guided by both the European Glaucoma Society and the American Academy of ophthalmology [14]. Figure 1.3 illustrates an example stereo fundus image. Both images (left and right) were captured at different angles simultaneously by NAVIS-Lite [15].

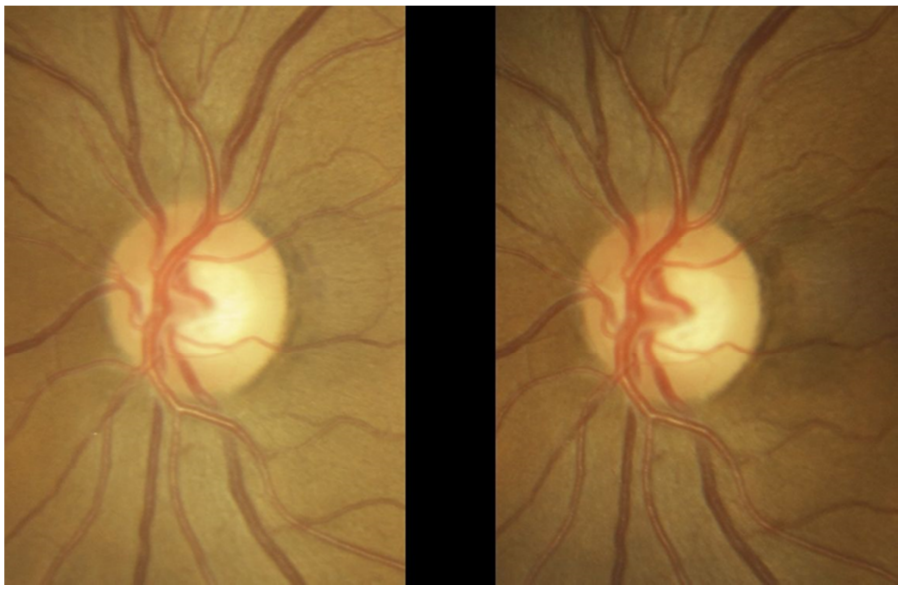

Figure 1.3 Stereo Optic Nerve Head (ONH) image [15]

- **Fluorescein angiography/Indocyanine green angiography**: Fluorescein angiography is an important invention for examining vascular structures on the retina. The principle was first proposed by Maclean and Maumenee [16] and later developed by Novotny and Alvis [17]. The technique is based upon the characteristic of fluorescein which is capable of absorbing light in the blue wavelengths and emitting it in the green wavelengths. Initially, fluorescein dye is injected into vessels and this defuses into the surrounding tissue. Then a fundus camera equipped with excitation and barrier filters is used to capture an image that registers the amount of injected fluorescein dye remaining within the retinal blood flow. The excitation filter allows a blue light to be projected into the eye, thus a green light is emitted from fluorescein. The barrier filter (yellow) blocks any reflected blue light

but allows green light through. A range of different pathologies can be diagnosed by analysing a sequence of images captured during the fluorescein angiography procedure. Figure 1.4 illustrates a fluorescein angiogram image of a normal eye in which we can see that the contrast between vessel and background (other structures) is enhanced.

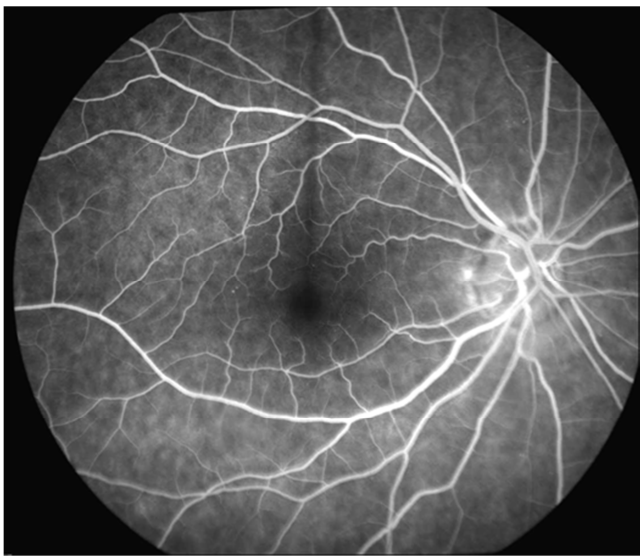

Figure 1.4 Normal Fluorescein Angiogram [18]

A similar technique known as Indocyanine green angiography uses indocyanine green dye (a tricarbocyanine dye) which is sensitive to infrared rays. Consequently the fundus camera is equipped with different filters.

The utilities of Fluorescein angiography/Indocyanine green angiography are common in recent clinical applications because they provide significantly functional information about the retinal circulation.

- **Scanning laser ophthalmoscopy (SLO)**: SLO is a confocal optical system used to obtain a three-dimensional image having plane coordinates (x-axis, y-axis) that are vertical to the optic axis (the z-axis is along the optic axis). Unlike conventional photography, SLO uses a laser beam instead of a bright light to scan each point across the fundus, then the reflections of light at each point are captured on imaging plane (e.g. CCD) through a narrow aperture (a confocal pinhole). The confocal pinhole can minimize image blur and hence a more clearly defined image can be obtained [20]. Recently, Heidelberg Retinal tomography II (HRT II) [19] has been used in a clinical application for diagnosis and monitoring of glaucomatous optic neuropathy and retinal imaging [10]. Figure 1.5 (a)

presents an image of the optical nerve head on the retinal nerve fibre layer, obtained by HRT II. The latest version, the Heidelberg Retinal Tomograph III (Figure 1.5 b) is more compact [21], the software has been upgraded to address an issue within the previous application that required the clinician to manually identify the optic disc resulting in variability of disc outline. Moreover, it is capable of providing a glaucoma probability score (GPS) based on automatic analysis of three scans of the disc [21].

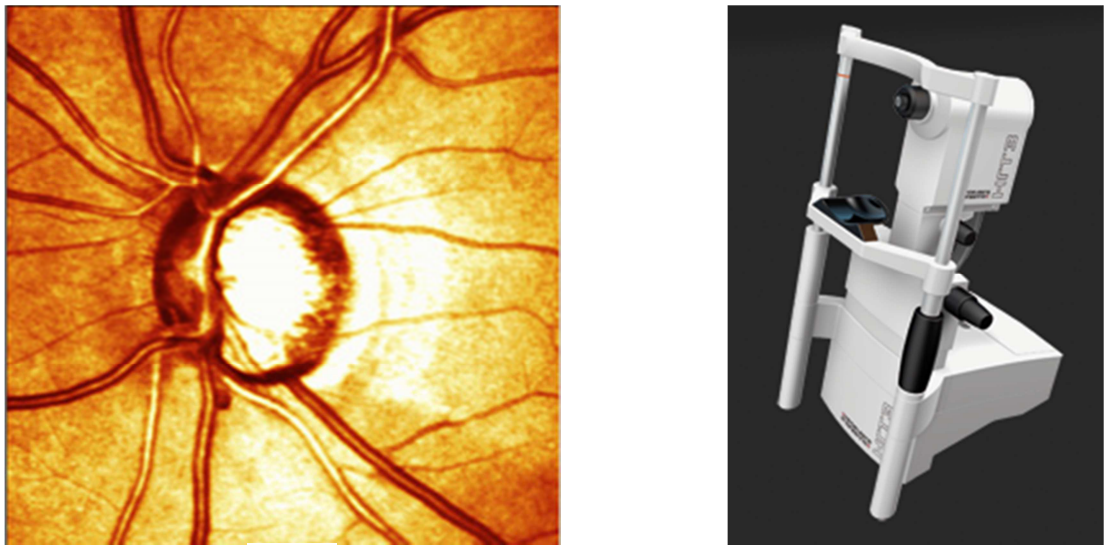

(a) (b)

Figure 1.5 (a) Image at the retinal nerve fibre layer obtained by Heidelberg Retinal Tomogroph II (b) The Heidelberg Retinal Tomogroph III.

Many fundus imaging techniques have been designed and developed for screening the internal retina and much effort has been made to improve the accessibility of the equipment. This overcomes the issue that traditional fundus imaging needs to be operated by experienced ophthalmic photographers. The most common and straight forward solution for improving accessibility is the adoption of a digital sensor (e.g. a charge-coupled device (CCD)) to record reflected light instead of using the traditional film-based imaging plane. This trend has resulted in widespread use of digital fundus cameras for routine clinical applications in ophthalmology departments. Moreover, the adoption of digital fundus cameras is consistent with technologies such as the Picture Archiving and Communication Systems (PACS) [23] which provides an economical storage solution for effective management, convenient distribution and presentation of medical images and rapid image retrieval etc.

Although new techniques such as tomographic imaging methods (SLO) can provide more detailed and specific images, there is still a role for conventional fundus photography. The safety, cost-effectiveness and accessibility of the digital fundus camera, and the acceptance of fundus photography as the primary fundus imaging technique for various ophthalmologic applications, drives research in retinal image processing and analysis .

1.2.3 Landmarks of fundus photography

Fundus photography (producing fundus images) has been employed in routine clinical therapy for a very long time. Many ophthalmological departments of hospitals in the UK are equipped with fundus cameras. Due to its relatively low cost, clinical diagnosis via fundus image analysis is still the most prevalent way to detect ophthalmic disease or assess some systemic diseases (these diseases are further described in section 1.2.4). The potential utilities of CAD offer an ability to analyse large numbers of fundus images and report corresponding diagnoses automatically. Consequently, accurate diagnostic reporting depends on reliable techniques for landmark identification and investigation.

A fundus photograph contains several important elements which could be used in various clinical applications. Primarily, these elements include the macula, optic disc (OD) also known as the optic nerve head (ONH), vessels and background structures.

Figure 1.6 illustrates an example retinal image used in a routine ophthalmic application. The image is captured from the left eye. The left bright circle is the optic disc and its cross-sectional view is illustrated in figure 1.1. It's generally called the physiological blind spot because it allows optic nerves to pass though and transfers the signal to the brain. This component is extremely important in clinical applications involving the diagnosis of glaucoma. The dark area located near the centre of the image is the macula which aggregates visual pigments. Much research focuses on detecting its pathology (e.g. macular degeneration) as this influences vision. The vascular system of the eye which supplies blood to the retina includes invisible parts (e.g. choroid) and visible vessels which lie on the surface of retina.

Normally, retinal blood vessels emerge from the ONH and radiate over the interior surface of the retina in various directions. Their specific characteristics can be described as follows.

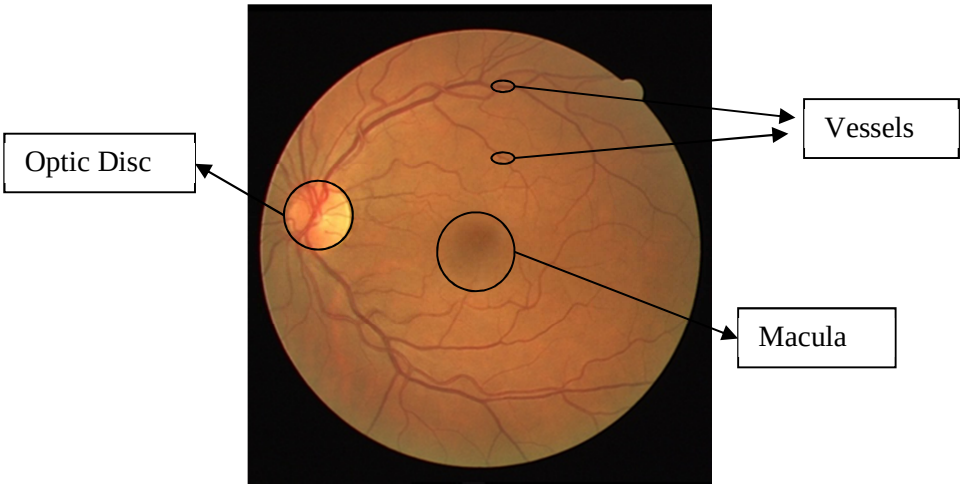

Figure 1.6 An example retinal image (fundus photography) showing anatomic structures.

Anatomically speaking, the retinal blood vessel trees can split into different types: arteries, veins, arterioles, venules and capillaries, which are characterized by their diameters. Usually the arteries and veins are characterised by larger calibres and the arterioles and veinules are smaller. In fact, the arterioles and venules are of equal width during childhood. However, for an adult, the calibre of the arterioles is narrower but diameters of venules are enlarged, because of fibrosis of tissue caused by the physical pulse of the circulation system [24]. The capillaries are the small branches at the end of the vessel tree. Some of them just appear as 2-4 pixels wide in a retinal image. Many diseases can cause pathological changes of these vascular structures and this in turn influences their visual appearance. For example, hypertension results in leakage of the vascular blood also known as haemorrhage due to rising blood pressure. The leakage of plasma and blood that permeates the surface of the retina will influence visual function. Retinopathy, such as venous changes, (e.g. distortion and dilatation of the retinal vein) and breaks in capillaries can be found in diabetics. The pathological changes in capillaries may result in leakage which may extend to the fovea area leading to loss of vision. In section 1.2.4 we will describe specific diseases which can be analysed and studied using retinal images. In many clinical cases, it is extremely important and significant to isolate and study retinal blood vessels for diagnosis and treatment of related diseases.

There are several specific characteristics that can be used in retinal vessel studies. However, some of them may hinder distinguishing the vessels from other organs.

- The vessels are treelike and tubular structures. Each structure is supposed to be connected.

- Vessels appear in low contrast against the background. The appearance of blood vessels is dimmer than the background in colour fundus photography. The colour of vessels normally is dark red, and the background is close to orange. In a grey level image, their appearance is close to the other elements in the background (e.g. the macula). The appearance of capillaries may be very similar to that of the background.

- Because of the illumination, the vessels may contain specular effects located on the centre of vessel objects.

- In grey level images, the grey level of vessels is continuous and does not change abruptly.

- The vessel is a piecewise linear shape. The curve of the outline is relatively smooth without abrupt changes of orientation.

- Vessels are not all the same size. The width of a vessel covers a wide range of diameters and they can be extended along their length at any orientations.

- Vessel cross-sectional intensity profile approximates a Gaussian shape [85].

- Some specific shapes may characterise specific vessel pathologies. For instance, nipping of the arteriovenous crossing [24] may be presented in a fundus image of a hypertensive patient and spot shapes (microaneurysms) [25] may be found around the vessels in a diabetic patient's fundus image.

1.2.4 Review of common diseases using analysis of retinal fundus images

Because many pathological abnormities in the retina manifest some systemic diseases and some ophthalmic diseases are caused by pathologies of the retina, the diagnosis of disease, either systemic or ophthalmic, based upon observing and documenting changes of eye tissues in fundus images has become particularly prevalent. In order to further discuss the important utilization of fundus images in clinical application, we summarise the most common diseases which have been studied based on the analysis of fundus images. The following provides a brief overview.

- **GLAUCOMA**

Glaucoma is a significant disease that leads to 12% of overall blind registrations in the UK, it's been diagnosed particularly in the elderly, i.e. those in the 65 plus age group. Studies have reported glaucoma to be a common problem affecting 0.5% of the total population including 1% in the over 45s and 6.6% in the over 75s [25]. Glaucoma is the third leading cause of blindness in the U.S. [26]. It is a primary optic neuropathy that manifests the loss of nerve fibres which may associate with raised intraocular pressure. Visually, the hallmark of this optic neuropathy is a characteristic change in the optic nerve head known as cupping of the optic disc (Figure 1.7). The pressure on the nerve head may reduce the blood supply to the rim. As a result the axons of the retina may be damaged. This process will appear as an enlargement of the central cup or as defects of the nerve fibre layer in the focal area.

In routine practice, there are three characteristic measurements that can be tested for diagnosis of glaucoma. Firstly, raised intraocular pressure (IOP); Secondly, a characteristic pattern of visual field loss and thirdly pathological changes (cupping) of the optic nerve head [27]. The accurate diagnosis of glaucoma depends on taking all these inter-related features into account, as raised IOP alone may give false positives and testing of the visual field is time-consuming and requires specific equipment [25]. Accurate assessment of cupping of the ONH depends on accurate analysis of the optic disc [28]. The use of fundus images for analysis of the optic disc has been employed to detect early cases of the glaucoma before deterioration of the visual field develops using characteristic features of the disc and signs of vascular changes.

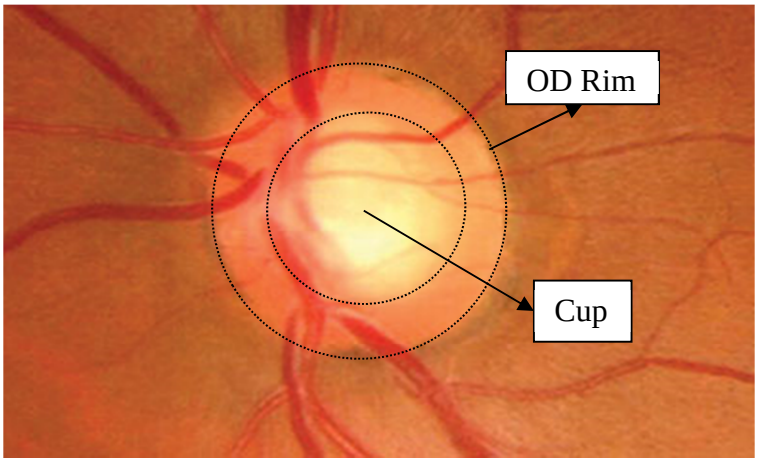

Figure 1.7 A fundus image of glaucoma patient. Diagnostic: focal nerve fibre loss.[27]

An important indicator for assessing the cup is the cup/disc ratio which is measured by judging the cup's vertical height against the vertical height of the optic disc. In normal eyes the cup/disc ratio is generally below 0.5 except in some special cases that represent congenitally enlarged disc with a large cup. Difference in the cup/disc ratio between both eyes of 0.2 or more is a risk indicator for glaucoma. Moreover, a vertical cup/disc ratio larger than the horizontal ratio combined with an OD that does not have an increased vertical diameter is a sign of neural rim damage. Besides assessing the pathological changes of the OD, a fundus image based glaucoma analysis procedure, needs to assess the vascular changes around the OD, so that the progression of glaucoma can be recorded and measured. For example, evidence of vascular haemorrhage on or around the optical disc is a common clinical sign in patients with progressive glaucoma. In advanced glaucoma, other morphological features of vessels may be detected, such as a narrowing in the appearance of the retinal arterioles. Abnormal distortion of vascular shape (e.g. the appearance of so-called z bend also known as bayoneting) may signify local erosion of the neural rim [28].

- **Age-related macular degeneration (AMD)**

Age-related macular degeneration (AMD) is a common eye disease that causes irreversible vision loss (such as blurred vision or slight distortion) in adults older than 50 years of age. In AMD, the macula (see Figure 1.6) degenerates with age and this results in vision blur or more severely loss of central vision. According to an NHS report, up to 500,000 people are affected by some form of AMD in the UK [30]. It is also reported to be the most common optical disease causing visual loss in the U.S. Approximately 7,300,000 Americans have some form of AMD [31]. Patients with AMD suffer no pain in the early stages of the disease, hence it is difficult for patients to perceive symptoms until they get the blurred vision or loss of central vision, (i.e. they cannot see objects in front of them clearly) [29]. Normally, AMD is classified as being one of two forms: early stage AMD- Dry macular degeneration (DMD) and advanced stage-Wet macular degeneration (WMD). DMD usually manifests itself by the appearance of drusens (small yellowish-white blobs), which are the deposits of epithelial cell waste located beneath the retina. WMD also known as choroidal neovascularization is indicative of abnormal growth of the choroidal vascular structure into or around the macula. These new vessels are weak and easily bleed [32]. Drusen are present in both forms of AMD and are classified as two types, hard and soft (Figure.1.8). Hard drusen (Figure.1.8-a) are characterised by a clear boundary that can be easily defined. Hard drusen are generally less

harmful than soft drusen (Figure.1.8 -b). These present a fuzzy boundary, which may be accompanied by other abnormalities such as new growth of the vascular structure.

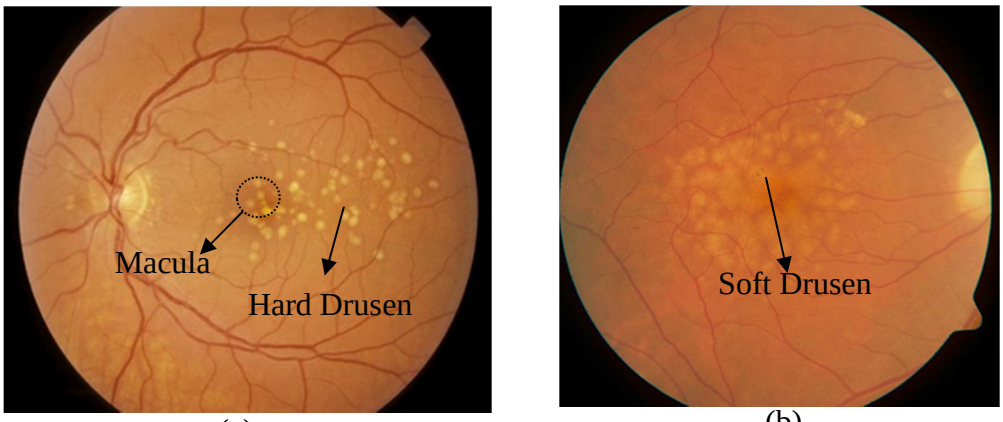

(a) (b)

Figure 1.8 Two forms of age-related macular degeneration (AMD). The bright spots in (a) are hard drusen; (b) is wet AMD with soft drusen.

The dursen can be gradually formed into any shape, size and number during the development of AMD, hence identification of dursen's characteristics are used by ophthalmologists to assess the progress of AMD so patients can receive appropriate treatment without delay. It is extremely significant to detect hard drusen in the early stage of AMD so that one is able to stabilize the pathogenic condition.

Currently, routine clinical identification and evaluation of drusen is implemented with the aid of fundus colour images which provide important signs for diagnosis. Many efforts in computer-assisted analysis of AMD have been made to achieve large population-based diagnoses of patients. In particular those studies which concern automated drusen detection and assessment based upon fundus images have been reported in much of the literature [34][35][36][37][38][39].

- **Vascular disorders**

The blood supply of the retina is through the choroid and retinal vessels which lie on the top of the retina. The retinal vessel is the only visible part of the blood circulation system. Observing the changes of the vascular characteristics can give information about the health of vessels, moreover pathological features of retinal vessels can manifest the risk of cardiovascular disease, such as hypertension, atherosclerosis and retinal vein/artery occlusion.

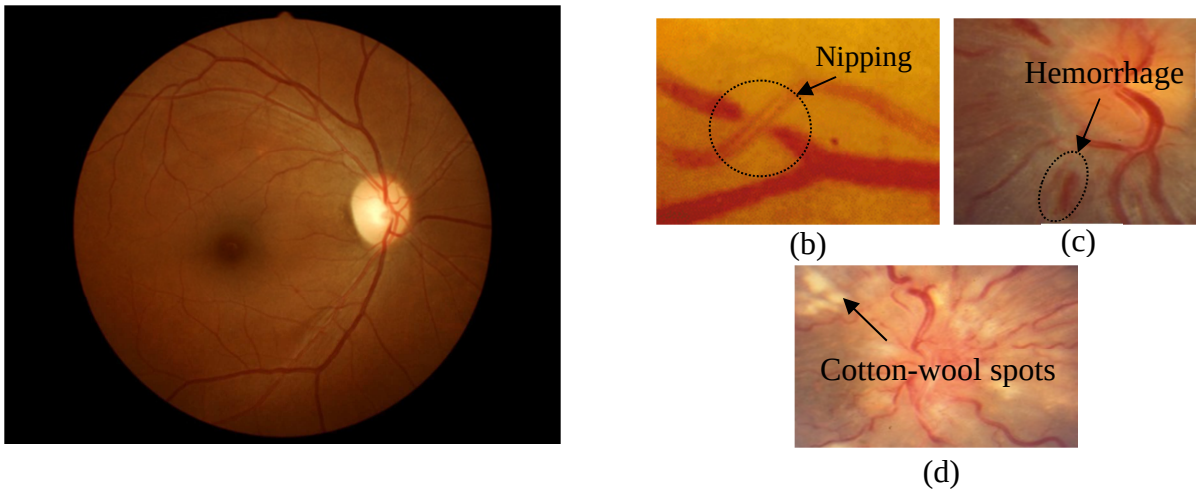

Figure 1.9 Manifestations of hypertensive retinopathy in fundus images. (a) A decrease A/V ratio; (b) nipping characteristic; (c) example of flame haemorrhages; (d) pale cotton-wool spots [42].

Vascular disorders can affect the eye by various forms, for instance, new vessel formation in the OD and the macular, and acute ischemia, which cause cotton wool spots and the appearance of flame haemorrhage on the surface of the retina, etc. [24]. Some features that appear in fundus images of hypertensive patients can reflect the seriousness of hypertension thereby indicating whether the patient demands immediate treatment. In the early stage, the nipping or nicking of the arteriovenous crossing (crossing points of arteries and veins) is defined as early evidence of hypertension (Figure 1.9-b), whilst the appearance of scattered flame haemorrhages (Figure.1.9-c) is a classic indication of hypertension [24][25][41]. The narrowing of the arteries and the dilation of veins are symptomatic of patients at risk of subsequent development of hypertension [40]. Figure 1.9-a illustrates the appearance of mild narrowing and sclerosis of retinal arteries resulting in a decreased overall A/V ratio [42]. In practice, a decreased ratio between diameters of arteries to those of veins also known as the A/V ratio is used to assess the risk of hypertension. For those patients who have hypertension, the appearance of pale cotton-wool spots (Figure1.9-d) in the fundus image suggests urgent treatment is needed [25][41][42].

Retinal vein or arterial occlusion is a complication associated with hypertension or diabetes. The former is more common, however occlusion of retinal arteries is more severe as it is irretrievable. In a pathological fundus image, signs of retinal vein occlusion are characterised by dilated and tortuous veins, which may be accompanied by massive

haemorrhage. The range of these haemorrhages depends on the type of retinal venous occlusion, which is classified as either central or branch. The central retinal vein occlusion presents global haemorrhages, whilst the haemorrhages of branch retinal venous occlusion occur in the local area of the fundus image. Retinal arterial occlusion is characterised by the appearance of pale embolus around the area at the artery branch. Patients suffering from this condition are at risk of a retinal stroke which may block the blood flow to the retina and therefore result in retinal death.

- **DIABETIC RETINOPATHY**

Currently, the diagnostic criteria for diabetes is defined by the world health organization (WHO) to be a patient who has a fasting level of plasma glucose $\geq$ 7.0mmol/l (126mg/dl) or 2–hour plasma glucose $\geq$ 11.1mmol/l (200mg/dl) [43]. Approximately 171 million people in the world were diagnosed with diabetes in the year 2000. This number is estimated to increase in the next decades, and is predicted to increase to 366 million by 2030 [44]. Approximately 3.5% of the UK population are affected by diabetes [10] and the U.S. Department of health and human services (DHHS) reported that 9% of adults (aged 18 and over) had been diagnosed with diabetes [45]. Diabetes manifests as a rise in blood glucose which many cause damage to vascular walls. Consequently, it results in diabetic complications known as diabetic retinopathy which may cause loss of vision. Diabetic retinopathy is the leading causes of blindness or visual loss within the working age group [46]. According to a clinical study report [47], in England and Wales, approximately 7.6% of patients who registered as vision impaired during year 1999-2000 are affected by diabetic retinopathy, resulting in 6.3% blindness for this patient group. A report presented by 'prevent blindness America' [48], indicates that diabetic retinopathy affects approximately 7.7 million U.S. people aged 40 and older in 2010. Routine screening for diabetic retinopathy and early detection of sight-threatening changes can be used in early diagnosis. A laser treatment called photocoagulation, can be prescribed to prevent the consequent loss of vision [25][49][50][51].

The prevalent forms of diabetic retinopathy can be typed as mild or severe depending on whether the pathological abnormalities are associated with damage to the macula or fovea. It can also be classified as non-proliferative retinopathy or proliferative retinopathy by considering how the abnormalities and pathological changes present new growth of tissue (vessels). The progress or deterioration of diabetic retinopathy is a gradual procedure. Normally, background retinopathy (Figure 1.10-a) can be detected at an early stage of

diabetes and it is less harmful. It is characterised by the appearance of microaneurysms, scattered haemorrhages and retinal exudates. Microaneurysms are a specific sign of diabetes and manifest themselves as small red dots, occurring in areas around the macula. The haemorrhages are caused by leakage within small weak vessels (capillaries) that can be observed from retinal fundus images as flame blots. In early stages of retinopathy, these haemorrhages normally appear as a few isolated components, distant from macula or fovea rather than the mass of haemorrhages indicative of severe retinopathy (Figure 1.10-c). The leakage of fat and protein from weak vessels may form yellow white blots in the retina called retinal exudates or hard exudates (Figure 1.10-a). They are characterised by a clear identified boundary, appearing as brighter blots than background, but these do not affect the macula or fovea. However, in some severe cases of retinopathy (diabetic maculopathy), normally occurring in type II diabetes, there are increased numbers of exudates with an enlarged size, spreading towards macula or in some cases even aggregated on the macula Figure.1.10-b (so-called macular exudate). Consequently these pathological changes may be accompanied by macular oedema, which has been reported as the most common cause of virtual loss in diabetics [9][25].

Retinal ischemia is an important factor causing severe diabetic retinopathy. Characteristic features such as a mass of haemorrhages, venous tortuosity and dilatation, cotton-wool spots, intra-retinal microvascular abnormality (IRMA), and proliferation can be detected in such fundus images. The size and number of these haemorrhages rapidly increase. The veins are dilated and tortuous because of hypoxia. The cotton-wool spots appear as white patches, fluffy in density with a fuzzy boundary on the retinal nerve fibre layer. This results from accumulations of swelling axon terminals which are caused by stimulation of retinal ischemia [52]. IRMA is characterised by abnormalities of capillaries (dilation and tortuosity).

One or more of these features appearing in a fundus image indicates that retinopathy has deteriorated into the pre-proliferative stage (Figure 1.10-c). This also signifies that the proliferation of IRMA is more likely [24]. However, early detection and treatment in this stage can prevent the further deterioration to the proliferative retinopathy stage (Figure 1.10-d). Although this is not common it is very severe and results in blindness. The characteristics of proliferative retinopathy are the appearance of new growth of blood vessels on the retina or OD. Because of severe hypoxia, the new vessels seek other sources of oxygen by growing in any direction and this may lead to vessel growth on the OD and the area between the lens

and vitreous body. Consequently, this may result in vitreous hemorrhage when blood and other liquids contaminate the vitreous body. This pathological change may even progress and in severe cases may detach the retina. Therefore, it's very important to give laser treatment before vitreous hemorrhage occurs to prevent blindness.

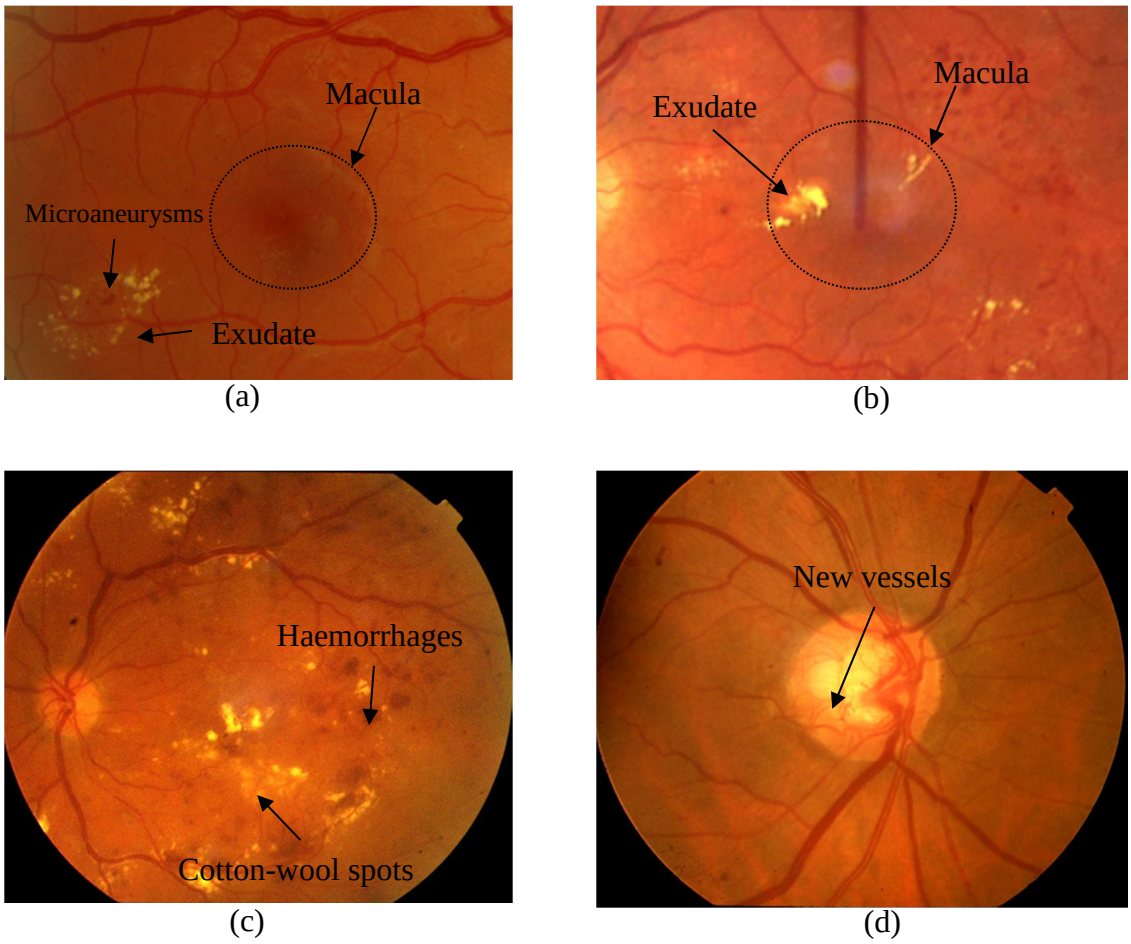

Figure 1.10 Different stages of diabetic retinopathy in (a) background retinopathy; (b) macular exudates; (c) pre-proliferative retinopathy and (d) proliferative retinopathy.

1.3 Automated detection of retinal disease using fundus images

A traditional but prevalent way of retinal disease diagnosis is manual screening and reviewing the images by ophthalmologists in routine clinical diagnosis. However, with the popularized utilities of new optical examination techniques and equipment, an abundance of images have been generated to assist the diagnosis. The quantity of images already exceeds the limit of the clinicians' ability to fully utilize it. Not only because manual diagnosis is a time-consuming procedure and the huge number of patients' demand prompt diagnosis by a

limited number of ophthalmologists before they can receive appropriate treatment. But also the manual diagnosis is experience dependent and high quality clinical detection relies on rich experience. For example, in some cases, changes in the pathology (e.g. the new growth of tinny vessels or microaneurysms in proliferative retinopathy) are difficult to observe and distinguish and therefore decisions are prone to inter and intra-observer variability. This in turn may result in patients missing the best time for treatment. An effective scheme to achieve population-based diagnosis relies on developing automated screening tools or computer-assisted diagnostic (CAD) systems that employ modern advanced computing techniques (image processing and analysis, computer vision techniques, distributed computing etc.). In the past few decades, numerous steps have been undertaken to achieve more accurate automated diagnosis using digital fundus images. A brief review of the latest techniques and their relevance to the specific diseases described in section 1.2.4 is summarized in the following sub-sections.

1.3.1 Automated detection of Glaucoma

Automated classifications of normal or glaucomatous patients need to rely on evaluating the features extracted from the patients' fundus image. In routine clinical glaucoma detection, such features may include cupping of the ONH, nerve fibre layer defects, and peripapillary atrophy etc.. Among those features, cupping of the ONH is the most important sign of glaucoma. As we described in section 1.2.4, the pathological changes of Glaucoma in the optic nerve head (ONH) area which can be observed from a retinal fundus image are primary indicators but they are not limited to this area. Numerous methods have been proposed to automatically detect and combine one or more of these abnormities in the optic disc followed by analysis to determine if they belong to corresponding progressive stages of the disease using a diagnostic criterion (e.g. C/D ratio etc.). Under normal circumstances, to calculate this ratio, the optic nerve head and optic cup need to be detected and extracted. In [55], Nayak et al. proposed an automated glaucoma detection method which employs three features: the C/D ratio, the distance between optic disc centre and the ONH, and the ratio of the total area of the blood vessels in the inferior and superior side of the ONH to the total area of the blood vessels in the nasal and temporal area. Morphological closing and opening operations followed by a thresholding method are adopted for segmentation of the ONH. Vascular tree segmentation is implemented using bottom-hat filtering combined with thresholding. Finally, classification is performed by an artificial neural network (ANN)

classifier. In another article [56], the displacements of blood vessels within the OD are measured. The distances between centroids of the vessels in the superior, inferior and nasal areas to a reference point in the temporal side of the retina is proposed to distinguish normal or glaucomatous subjects. The performance of this method achieved 93.02% sensitivity, 91.66% specificity, and 91.34% accuracy. Further state-of-the-art methods for automated extraction of anatomical features from retinal images for early diagnosis of glaucoma are presented in the survey [57]. Bock et al. [53] proposed a system for automated glaucoma detection using colour retinal fundus images and achieved 80% accuracy. Pre-processing is implemented to address inhomogeneity in the illumination. Vessels localized on the ONH are removed by applying retinal vessel segmentation followed by inpainting of the detected vessel tree. Then three features are generated by different generic image representations, which are used to generate a glaucoma risk index (GRI). Finally, a stand-alone SVM classification scheme combines the GRI to generate a diagnosis. Noronha et al. [54] proposed an automated glaucoma diagnosis system that classified three states of glaucoma (normal, mild and severe) using a support vector machine (SVM) and Naive Bayesian (NB) classifiers based on features derived from higher order spectra (HOS) cumulants extracted from a radon transform of the digital fundus images. The performance of their system reaches 92.65% accuracy.

1.3.2 Automated detection of AMD

Age-related macular degeneration (AMD) is the most common cause of gradual loss of vision in the aged 50 and over group in the UK and U.S.. The critical risk of AMD is that it can't be perceived until vision is impaired. Early detection of AMD may reduce this risk and laser treatments can be used to stop progression of the disease. Five computer-assisted diagnostic systems for detecting and manually grading AMD which have been used in clinical applications are summarized by Zarbin and Chu [58]. These systems have potential to be improved by replacing the manual grading stage with an automatic grading module, thereby allowing the system to meet the demands of an enormous number of patients. During recent years, many efforts have been devoted to studying automated diagnosis of AMD using different features extracted from components in digital colour fundus images of the retina. The methods initially detect abnormalities in retinal fundus image then classify cases as normal or AMD via quantification of those features. Many modern digital image processing and analysis techniques can be employed, e.g. image compression, image enhancement and

image segmentation etc. The most important part of the process is the automated segmentation of drusen, as they are the characteristic sign of AMD.

To some extent, the performance of a system for automated diagnosis of AMD relies on adopting a successful method of segmentation. Bhuiyan et al. [59] proposed a method for the detection and quantification of drusen for early detection of AMD. Initially, a vessel tree and background mask is generated to exclude the vessels and background related interference. Then drusen are detected using the combined local intensity distribution and adaptive intensity threholding. A first order Gaussian derivative filter is employed which works with the mask to generate a magnitude image without vessel and background pixels. This is used to identify edge information of drusen. The severity of early AMD is evaluated by quantifying the drusen occurring in the area of the macula. Their proposed method achieved 100% accuracy of drusen detection in 50 images collected by them. Rapantzikos et al. [60] employed multilevel histogram equalization (MLE) based on sequential applications of histogram equalization to enhance image contrast followed by histogram-based adaptive local thresholding (HALT) for detection of drusen. The advantage of utilizing HALT is that it is capable of extracting features of interest without influencing other components [60] (e.g. haemorrhage, vessel and optical disc). The method presented in paper [61] focuses on automated detection of advanced AMD by detection of the wet drusen and patches indicative of haemorrhage. Three regions of interest: (blood vessels trees and haemorrhages, OD and macula, background) are segmented using the *k*-means clustering algorithm, of which haemorrhages and drusen are related to the first and second regions. The vascular trees are removed by implementing erosion and dilation using cellular neural network (CNN) templates. Boundaries corresponding to regions of interest (ROI) are found using a Sobel operator and these are used for monitoring the progression of the condition. Kose et al. [62] proposed a method which allows ophthalmologists to evaluate if treatment for degeneration is effective or not by automatically monitoring changes in the degeneration. Instead of detecting abnormalities directly, their method first extracts health components from the area containing the macula using a region growing method. Then the vessels are segmented and healthy components in the ROI are eliminated. The final segmented image is obtained from inversing segmented images. Finally, the quantitative results can be generated by comparing the segmented pathological structures (degenerated areas) at different time periods. For the purpose

of automated diagnosis, if the detected degenerated area exceeds a clinical safe threshold value, the diagnosis is positive. A stable feature generated from drusen based information extracted from intensity, colour and gradient information is proposed by Burlina et al. [63]. This is produced by using a hybrid parametric constant false alarm rate (CFAR) detector combined with a non-parametric CFAR detector based on a support vector machine (SVM).

1.3.3 Automated measurement of vascular disorders

Pathological changes of vascular structure caused by medical conditions such as hypertension may lead to retinopathy and therefore affects vision. Abnormalities on the retina also are significant signs of the progression of cardiovascular disease (see section 1.2.4). Morphological characteristics of vascular trees such as atrophy, dilation and tortuosity can be expressed by the A/V ratio and other mathematical terms. These terms are extremely important for automated measurement of the vascular tree and these features can be used in early diagnosis to prevent heart attack, brain stroke etc. Hence automated measurement of vascular structure has attracted a lot of interest by researchers.

Narasimhan et al. [64] proposed a method for diagnosis of hypertensive retinopathy by estimating the A/V radio. Features derived from grey level moments, intensity and colour information were employed for vessel tree segmentation. Vessels are classified by measurement of geometrical widths and the A/V ratio is calculated. This is used as a marker to grade the severity of hypertensive retinopathy. A similar method of A/V ratio measurement is proposed by Niemeijer et al. [65]. In their method, vessel segmentation is implemented by a k-NN classifier. Then the centreline of each vessel is skeletonized from segmented vessels. The local vessel width is measured by finding the left and right vessel edges from the centreline and calculating the distance between them. The A/V radio is calculated by an iterative process. Ortíz et al. [66], implement vessel enhancement by using a Gabor wavelet combined with a Hessian matrix and the resulting images then are binarized using a threshold method (Niblack) to obtain the vessel segmentation. The vascular widths are obtained using the Parr-Hubbar formulas, which is a relative precise measurement. The tortuosity of the vessels is a significant property especially for early detection of retinopathy, and important because it allows early diagnosis to be given such that patients may receive timely treatment. The commonest way to measure the retinal vessel tortuosity is the ratio between curve length

and chord length which is defined as the distance between the curve end points [67]. Chandrinos et al. [68] proposed a mean angle metric based on changes in the local direction of the vessel. Grisan et al. [69] proposed a novel vascular tortuosity measurement method which simulates the procedure of clinical evaluation of tortuosity applied by ophthalmologists. Vessels are decomposed into a set of consecutive segments of constant-sign curvature and each is evaluated by integrating such segments.

1.3.4 Automated detection of DR

With the increasing number of diabetics, there are urgent demands for a computer assisted clinical tool to detect diabetic retinopathy. Such an application would enable those patients suffering from diabetes and any complications of diabetic retinopathy to receive timely treatment. In clinical practice, the early detection of diabetic retinopathy via population screening have been shown to prevent vision loss and blindness [49][50][51]. Towards this direction, international and national guidelines encourage all diabetic patients to have an annual fundus examination. In England and Wales, a national fundus screening program has been recommended by the National screening committee. The same guidelines have been issued by the Haute Autorité de santé (HAS) in France [70]. In the Netherland, over 30000 diabetics were screened since 2001 [9]. In several European countries, systemic programs for early detection of diabetic retinopathy via an expert manually reviewing using digital fundus photography have been integrated into existing health care systems. In an effective application of telemedicine, the fundus image is acquired from the patient by remote imaging and then reviewed by ophthalmologists to assess or grade. However, there are concerns regarding the cost of manual workload, particularly because of projected increases in the size of the diabetic population. In the next few years, it is estimated that the time required to implement the programme will exceed the limit of workloads. This situation stimulates intense research towards an automated population-based DR detection and grading system. Research effort over the past ten years has concentrated on designing automated detection of abnormalities (such as microaneurysms, exudates, cotton-wool spots, etc.) on the retina to diagnose and grade DR. Numerous approaches have been proposed to pursue more reliable schemes for automated detection of DR, since there is no completely independent automated DR program that can be applied in clinical practice. Generally, the research areas for automated DR detection using fundus photography can be divided into three primary categories. The first category is focused on designing systematic DR systems, the second for

developing segmentation and detection of those abnormalities, and the third for measuring the segmented abnormalities relating to different stages of DR.

Dupas et al. [70] measured microaneurysms, haemorrhages, and exudates based on a suite of algorithms for automated detection proposed by Sinthanayothin [71]. These algorithms were incorporated into a computer-assisted diagnostic (CAD) system for grading different stages of DR. The system performs detection of four classes of components (vessel tree, microaneurysms and haemorrhages, macula, and exudates), thus the combination of all four results can be used to assess the severity of DR by referring to specific grading rules. Their evaluation of the system show that for DR detection, the sensitivity and specificity of the algorithm were 83.9% and 72.7%. More specific protocols for clinical DR grading are presented elsewhere in the literature [72]. Yun et al. [73] proposed a DR grading system to classify samples into one of four groups (normal, moderate non-proliferative diabetic retinopathy (NPDR), severe non-proliferative diabetic retinopathy (SNPDR) and proliferative diabetic retinopathy (PDR)). The perimeter and areas of blood vessels and relative defects along the vessels are used as features for classification. The classification was achieved by employing a three-layer feedforward neural network (NN) classifier. They reported results in terms of accuracy, sensitivity, specificity of 84%, 91.7%, 100% respectively. Larsen et al. also present work for automated diagnosis to classify patients in two classes normal or DR [74]. The performance of their system can be adjusted by a so-called visibility threshold parameter (either set to a default value or supplied by user). They achieved 93.1% sensitivity and 71.6% specificity with the parameter set at high sensitivity and 76.4% sensitivity and 96.6% specificity with the parameter set at high specificity. Usher [75] et al. developed a tool for diagnosing patients as normal or DR. Their strategy initially extracts normal components (e.g. OD, vessels) and then excludes these structures using recursive region growing (RRG) combined with an adaptive intensity thresholding (AIT) approach to extract lesions (bright exudates). To extract those dark lesions (e.g. haemorrhages, microaneurysms), they adopted an edge enhancement operator they call a ‘moat operator’ technique. The classification was implemented by an artificial neural network based on the features generated from lesions. They report results of 94.8% sensitivity.

Many efforts have been devoted to automated detection of various abnormalities (e.g. microanrurysms, microaneurysms, exudes, vessels) in order to improve the stability of CAD systems. For instance Walter et al. [76] proposed a microaneurysms (MA) detection method

for use in colour fundus images. Potential MA candidates are detected by a diameter closing operator followed by an automatic threshold scheme. MA (or non-MA) classification is implemented by Bayesian risk minimization that relies on kernel density estimation. The system demonstrates 88.5% sensitivity at an average number of 2.13 false positives per image. In the literature [77], Giancardo et al. proposed a method for diabetic macular edema (DME) detection based on the detection of exudates. Features characterising exudates are extracted based on colour information and wavelet decomposition. Then the generated features are classified with an SVM classifier to automatically diagnose DME. The proposed algorithm is evaluated by AUC, of which the maximum is 0.94. Sánchez [78] proposed a novel method to detect hard exudates from fundus images which is capable of distinguishing hard exudates from other bright lesions. The algorithm uses mixture models to dynamically threshold the images to obtain exudates. Then the extracted exudates are further characterized by edge shape to distinguish them from other bright lesions (cotton wool spots and light reflection of vessels). The evaluation process demonstrated 100% sensitivity with 90% specificity.

1.4 The thesis contributions

Given the importance of retinal vessels for the diagnosis of various forms of diseases, the segmentation of vessels in fundus images remains a great challenge. This is due to the complexity of fundus images and conditions such as image noise, low contrast between vessels (capillaries) and background, some abnormal regions (pathology), illumination (vessel reflection), and the variety of vessels (different width, length). This topic is discussed in detail in chapter 2. Our research aims to design and develop more accurate retinal vessel segmentation methods based upon investigating texture analysis techniques. We particularly focus on texton-based approaches as these build on filter bank schemes that have been successful in earlier work. The primary contributions of this thesis include:

- A hybrid retinal vessel segmentation method that is able to exclude the interference caused by abnormalities in fundus images is proposed. Such anomalies (e.g. drusen) are the primary factor that influences the accuracy of segmentation in this field.

- A novel supervised texton based retinal vessel segmentation method is proposed which employs a new spatial filter bank design (MR11) for vessel feature extraction.

This method significantly improves performance in terms of accuracy and efficiency compared to many other state-of-the-art methods.

- We investigate the effect of different training regimes and provide an experimental basis for training a general textons library for vessel segmentation. Given that the lack of study materials (ground truth) is an open issue in this research field, we built a new dataset (using original data supplied from the Manchester Eye Hospital) that can be used as a resource for future vessel segmentation research. The data set includes 3 sets of ground truth, hand labelled by 3 ophthalmologists.

- Building on experience gained during the development of the MR11 filter bank a supervised texton based vessel segmentation method using an optimized Gabor filter is developed. We show that this approach saves computational cost while maintaining good performance. Finally, a new unsupervised retinal vessel segmentation method is proposed, which achieves a level of performance comparable with other supervised state-of-the-art methods. This unsupervised segmentation method represents a significant contribution since it addresses the problems that arise due to inconsistent ground truth labels in the database.

1.5 Organization of thesis

The rest of chapters in this thesis are organized as follows: Chapter 2 presents a comprehensive survey of previous and current techniques which have been proposed for retinal vessel segmentation. These methods are categorized into four categories and we review them by each category. Chapter 3 provides relative background information on textons and texture analysis techniques, in which an extensive review of prevalent texture measure techniques for image segmentation is presented. Chapter 4 presents a hybrid retinal vessel segmentation method which is able to obtain vessel segmentation that is robust to anomalies in the image. In Chapter 5, three subsets of experiments are described. A supervised texton based retinal vessel segmentation method is described in the first subset of experiments. Then the supervised texton based segmentation method is extended by optimizing the procedure for generating textons. The third subset of experiments comprises a comparative study undertaken in order to qualify the consistent performance of the method. Chapter 6 describes a further texton based segmentation method using optimized Gabor filters and an unsupervised texton based segmentation approach which uses a Derivative of

the Scale Invariant Feature Transform (DSIFT) and multi-scale Gabor filters. Chapter 7 presents conclusions and suggestions for further work.

CHAPTER 2

2. Review of retinal vessel segmentation and evaluation

The segmentation of retinal blood vessels and their extraction from the background in retinal fundus images is an essential stage for automated retinal vessel analysis and can also be a useful pre-processing step, prior to manual screening. The biomedical measurements of retinal vessels are analyzed and evaluated in several routine clinical diagnoses. For example, it is critical to diagnose, screening, and treatment for various ophthalmologic diseases, such as Glaucoma, AMD, diabetic retinopathy (DR) and vascular disorders etc., as discussed previously in section 1.2.4, because these characterise pathologic changes that manifest the progress of various diseases such as hypertension, diabetes, etc., segmenting retinal blood vessels and assessing segmented vessels is particularly important to detecting or grading those diseases. For instance, displacements of blood vessels within the OD are measured in some automated Glaucoma diagnosis systems [55][56]. In some systems used for diagnosis of AMD, Glaucoma and DR, retinal blood vessels are segmented and identified as the normal healthy components and so the system can eliminate these vessels from further stages and related inferences [53][59][61][62][75][78]. The vessels also can play a role by providing reference coordinates to describe the locations of other elements in the images [73]. The morphological characteristics of vascular trees include atrophy, dilation and tortuosity which can be expressed as the A/V ratio (see section 1.2.4 for more details) and in mathematical terms of tortuosity. These terms are extremely important for automated measurement of the vascular tree to prevent diseases such as heart attack, brain stroke etc. [64][65][66]. Moreover, retinal blood vessel segmentation has more specific significance for other applications. For instance, segmented retinal blood vessels can provide a tool for multimodal image registration [79].

Currently, vessel networks presented in retinal fundus images are primarily delineated manually by experts (ophthalmologists). Subsequently, these components can be used as signs to assess corresponding diseases based on particular clinical rules in the screening application or computer-assisted diagnostic system. However, the manual vessel segmentation is quite time-consuming and experience based, whilst the cost of workloads

(training, labour force) has to be considered. Many efforts have been devoted in developing automated vessel segmentation and computer-assisted diagnosis systems, which we have summarized in the previous section (1.3). To some extent, the reliability of those systems especially considering the accuracy of diagnosis is quite reliant on the performance of segmentation methods, as every false segmentation or miss-segmentation may affect accurate measurement of structures. It is commonly accepted by clinicians that automated assessment of vascular structures in the retinal fundus image is a critical stage in the development of a computer assisted diagnostic system for automated detection and grading of various forms of retinopathy.

Although automatic segmentation of the blood vessel networks has been studied widely and a large number of approaches have been proposed, it is still a big challenge and retinal vessel segmentation remains a focus for ongoing research. The challenges faced in accurate automatic retinal vessel segmentation include various factors. We list them as follows.

- Wide range of vessel widths, from large (12-15pixels) to small (2-5 pixels).
- The specific morphological characteristics, such as vessels (veins and arteries) may cross and overlap.
- Presence of noise in fundus images.
- The low and unstable local intensity contrast between vessels and background.
- Presence of pathology elements including haemorrhage, exudates, and microaneurysms etc. and the presence of other anatomic components in the fundus images (such as OD, macular).
- Different optical features in the fundus image; especially, those due to illumination which may result in various artefacts, e.g. light reflected from vessels which may influence the segmentation.

Figure 2.1 illustrates examples of such factors in fundus images which may influence the accuracy of automatic retinal vessel segmentation. The wide range of vascular width can be observed in all the sub-images. In practice, the most difficult task of retinal vessel segmentation is to detect the tiny vessels (capillaries) from the background. To the best of our knowledge no approaches have been proposed that are able to completely segment all vessels. Figure 2.1-b demonstrates the exudates (hard drusens and haemorrhages) which may result in an increase of false positives, namely those abnormalities that may be segmented as vessels. The boundary of the OD in Figure 2.1-c exhibits an extremely large intensity gradient change,

thus it may be mis-segmented as a linear structure (vessel). The vessel reflections may be detected as non-vessel, as its colour intensity is quite different from the normal vessel. Most of proposed methods utilize pre-processing techniques to handle this issue.

All the factors listed above may more or less influence accuracies of segmentation methods which have been proposed previously. Hence automatic retinal vessel segmentation remains a focus for current research.

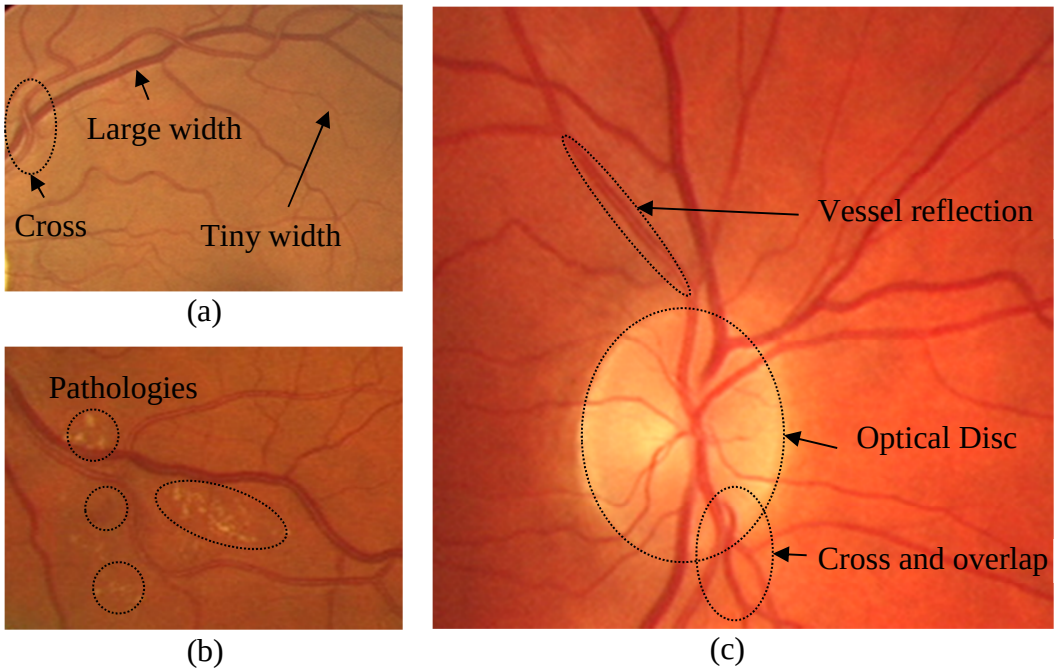

Figure 2.1 A series of factors influence the automatic retina vessel segmentation. (a) illustrates the large and tiny vessel width; (b) demonstrates the exudates, the boundary of the OD in (c) exhibits an extremely large intensity gradient change, vessel cross and vessel reflection are shown in (a) and (c).

A large number of such approaches have been proposed using various modern image processing and analysis techniques. Comprehensive surveys of vessel segmentation approaches in various modalities of medical images are present in the literature [82][83]. Some brief reviews of retinal vessel extraction methods have been presented in the literature [9][80][81], some of which may be particularly utilized as a tool for automated detection of pathologies. Fraz et al. present a survey in [84] that particularly focusses on approaches of retinal vessel segmentation in fundus images. In this chapter, prevalent evaluation methods and the most commonly utilized experimental materials (datasets) are introduced in section 2.1 and 2.2, respectively. We present a review of previous segmentation methods in section 2.3 where numerous approaches are classified into each category. The summarized methods

cover both early state-of-the-art methods and very recent published work. In section 2.4, we summarise the existing approaches, state corresponding problems and discuss the future trends of retinal vessel segmentation in fundus images.

2.1 Evaluation method

In order to evaluate the performance of retinal vessel segmentation methods, two categories of performance measures methodologies are commonly used to qualify the segmentation results. One evaluates the performance in terms of accuracy, sensitivity and specificity, and the other plots a Receiver Operating Characteristic (ROC) curve [131] and reports the segmentation quality by calculating the area under the curve (AUC). Either or both of these evaluation methodologies are used in retinal vessel segmentation methods reported in the previous section to generate comparative results that are able to indicate the merits of the methods. The values of sensitivity, specificity, accuracy and AUC can provide numerical evidence to verify the performance whilst the ROC method also produces curves that can be compared visually to study the performance of different segmentation approaches under the same circumstances. We introduce both evaluation methods in the next subsections.

2.1.1 Sensitivity, Specificity and Accuracy

To explain the terms (accuracy, sensitivity and specificity) clearly, we start by describing some essential properties of classifiers. Given a binary classifier and a candidate instance, there are four possible outcomes. Table 2.1 shows these four outcomes. The real class is labelled as {T, F}, and we use the labels {P, N} for the class predictions. If an instance is positive and it is classified as positive, it is counted as true positive (TP), however if it is classified as negative, it is counted as false negative (FN). Analogously, if the instance is negative and it is classified as negative, it is counted as true negative (TN), but if it is classified as positive, it is counted as false positive (FP). In practice, the real classes are given by the ground truth, The ground truth is normally represented as a binary image in which pixels belonging to vessels have been manually labelled by experts. Sensitivity and specificity are the factors which indicate the rate of success of classifying vessel and non-vessel pixels, respectively. Accuracy, on the other hand, is an overall measure of the ratio of total well classified pixels with respect to ground truth.

Table 2-1 The confusion matrix of measures properties

		Real class	
		T	**F**
Predicted class	**P**	True Positives	False Positives
	N	False Negatives	True Negatives

Taking table 2.1 into account, the terms can be expressed as

$$Sensitivity = \frac{TP}{TP + FN}$$

$$Specificity = \frac{TN}{TN+FP} \quad (2.1)$$

$$Accuracy = \frac{TP + TN}{TP + FP + TN + FN}$$

2.1.2 Receiver operating characteristic (ROC) curves

The receiver operating characteristic (ROC) curve is a general tool to assess the performance of a classifier [203]. In general, a ROC plot is a two-dimensional graph in which false positive fractions (FPF) is plotted on the x axis and true positive fractions (TPF) is plotted on the y axis. For a binary classifier, the output is only a class label (e.g. either T or F, either 1 or 0). Each this classifier produces a pair of TPF, FPF corresponding to a single point in a ROC graph. The point plotted closer to the top left corner presents the better performance of the classifier. For some other classifiers (e.g. Neural network, Native Bayes Classifier), normally the output is an instance probability or score, which can be further used with a threshold to produce a binary classifier, each threshold value produces a different point in ROC. A ROC curve is then constructed according to those points. Here, a ROC curve plots true positive fractions (TPF) versus false positive fractions (FPF) by thresholding the image (e.g. a probability map) with different values starting from 0 up to 1 with a step size of 0.001, where the TPF is calculated by dividing the number of true positives by the total number of vessel pixels in the ground truth and the FPF is the number of false positives divided by the total number of non-vessel pixels of the ground truth (see equation 2.2). TPF (true positive

fractions) is also equal to sensitivity, and FPF (false positive fractions) is equal to (1-specificity). An ROC curve plotted closer to the top left corner is indicative of better performance of the method. Therefore, the increasing value of the area under the curve means better performance, the best value of the AUC is one.

$$TPF = Sensitivity = \frac{TP}{T}$$
$$FPF = (1 - Specificity) = \frac{FP}{F} \quad (2.2)$$

2.2 Available Materials

Standard sets of images make it possible to compare the performance of different segmentation approaches under the same circumstances so comparative measures can be generated. The DRIVE [132] and STARE [133] databases provide such materials as they are publicly available and have been widely used by almost all of the previous methods. A summary of these retinal fundus image databases is presented in the following subsections.

2.2.1 DRIVE database

The DRIVE database was collected by Staal et al. [102], and is publicly available on the website: http://www.isi.uu.nl/Research/Databases/DRIVE/. 40 images were captured by a Canon CR5 fundus camera at a 45^o field of view, each image was digitized with size 565×584, captured at 8 bits per colour plane and compressed, stored as TIFF format. The database is divided into training and test sets, where each set consists of 20 images. The manual segmentations are available for both sets. For the test set, manual segmentations are provided by two observers. In practice, the first set is used as ground truth whilst the other one can be used to provide a reference independent human segmentation, which can be used as a measuring standard to qualify the computer generated segmentation. However, only one set of manual vessel tree segmentations is available in the training set. Additionally, a mask for each image is available for both sets and this can be used to remove the rim border surrounding the field of interest. Compared with the STARE database, the condition of images in the DRIVE database is less complex, since most of the samples are normal cases.

2.2.2 STARE database

The STARE database was originally collected by Hoover et al. [90], and is publicly available on the website www.ces.clemson.edu/ahoover/stare/. The database consists of 81 fundus images captured by the TopCon TRV-50 fundus camera at a 35^{o} field of view. The images are stored as PPM format, 8 bits per colour channel and digitalized with size 700×605. The dataset contains two sets of hand-labelled ground truth made by two observers, each of which contains 40 binary manual segmentations images. No masks are provided. Compared to the DRIVE database, the conditions presented are more complex, as 10 of 20 images contain abnormalities. Also, the number of ground truth images is not as comprehensive as provided in the DRIVE database. However, it has irreplaceable value for retinal vessel segmentation research, since it provides some examples of pathological changes in the fundus image which may appear in routine clinical application and may present more difficulties for automatic vessel segmentation algorithms.

2.3 Retinal vessel segmentation methods

We would like to emphasise that the categorization of reviewed retinal blood vessel segmentation methods presented here does not relate to a strict taxonomy. Many recent retinal vessel segmentation methods normally adopt techniques which have been proposed by earlier researchers to resolve some particular problems (e.g. image smoothing, feature extraction, pattern recognition etc.), and some of them employ hybrid techniques to implement retinal vessel segmentation. In this case, we aggregated the methods which use similar key techniques (algorithms) into the same group when we reviewed them. Here the reviewed retinal vessel segmentation methods are primarily divided into four categories:

(1) Matched filtering;

(2) Vessel tracing/tracking;

(3) Classifiers

(4) Model-based segmentation.

We introduce these segmentation methods by each category in the following sub-sections.

2.3.1 Methods using matched filters

The basis of matched filtering methods for extracting vascular structures is derived from the concept of signal detection, in which a filter kernel is modelled as a template based on the known information in a signal. The modelled template can then be correlated with an unknown signal in order to detect the presence of the template in the unknown signal. For retinal vessel extracting purpose, the approach convolves the retinal fundus image with multiple 2-D kernels (templates) to generate corresponding filter responses which are able to represent vascular features. Those templates (2-D linear kernel) are designed by taking known information into account. (e. g. the vessel cross-sectional intensity profile can be approximated by a Gaussian shaped curve). A classic matched filter (CMF) was proposed by Chaudhuri et al. [85] for retinal vessel segmentation. Because of its simplicity, the CMF has been employed and further studied by other researchers for a long time. Matched filter based methods are normally combined with threshold-based segmentation methods to obtain a final binary segmentation result. There are several limitations of using CMFs. The efficiency of the algorithm may be affected by the size of the filter kernel. A large convolution kernel which needs to be rotated at various orientations results in increased computational costs. Moreover, it is difficult to extract various vessel widths using a filter set at one scale. As such the kernels size is determined by scale parameters which are selected to model a specific range of vessel widths. As a result, if a wide vessel related parameter is selected, many capillaries may fail to be detected. Additionally, the Gaussian kernel of the CMF will recognize non-vessel objects indicative of certain pathologies as vessels structures and this may influence the accuracy of segmentation. Given its advantages and limitations, CMFs have attracted extensive further investigations for retinal blood vessels detection in fundus images. Most of the proposed methods improve the CMF by modifying or optimizing the filter kernel to overcome some of the limitations, while other approaches combine the CMF with other techniques to achieve more accurate performances.

In the literature [86], the Gaussian function model [85] was further studied and an amplitude-modified second-order Gaussian filter was proposed by L. Gang et al. [86]. They optimized the parameters of the matcher filter via mathematical analysis and experimental simulation. In their work, they demonstrate that the optimal Gaussian filter to detect vessels is given when the parameter t equals 3.5, where t is the power of σ in amplitude factor $(\frac{1}{\sqrt{2\pi}\sigma^t})$

of second-order Gaussian filter (referring to the equation 5.5). The most significant contribution of their research is that they show that it is possible to measure the vessel diameter with a matched filter using parameters learned from a training set. Using this methodology in the vessel segmentation process, the success rate of detection can be improved. The proposed method is evaluated on 48 colour fundus images and the authors reported 94.3% of blood vessels can be detected.

M. Al-Rawi et al. [87] also improved the performance of the CMF by optimizing the filter parameters. Three important filter parameters L, σ and T are optimized (L indicates the length of the vessel segment that has the same orientation [85]; σ defines the spread of the intensity profile; T is a parameter used to truncate the long double sided tails of the Gaussian curve). In [85] parameters L, σ and T are 9, 2 and 6, pixels. M. Al-Rawi et al. optimized them to 10.8, 1.9 and 8 pixels respectively by comparing the segmentation results to corresponding ground truth. The term *accuracy* (94.3%) equals the TPR (true positive ratio) minus the FPR (false positive ratio) was used to optimize parameters. This figure represents an important reference when searching for better values of parameters. Meanwhile, their experiment also showed that the green channel is more appropriate than other bands (Red, Blue) for generating more true positive responses. The final segmentation results are obtained by using an automated threshold selection method, which considers different conditions of the number of connected components and Euler number. They present experimental results using the DRIVE database and demonstrate an average accuracy is 0.9535 with 0.9435 AUC.

Cinsdikici and Aydin [88] proposed a hybrid model using a matched filter and ant colony algorithm. Their novel method overcomes an imperfection of the CMF by improving the performance of detecting thin vessels (capillaries). The procedure of vessel segmentation comprises two parallel stages, one using the CMF and the other using the ant algorithm. At the end of the procedure, they combine the segmentation results with a logical OR operation and then use a length filter to remove disconnected segments to get the final segmentation results. Before implementing the vessel extraction, they add a pre-processing step to enhance the contrast between vessels and background, in which, only the green band of a RGB image was obtained. Then they applied a nonlinear intensity transformation on the green band image. Finally, the image is divided into several small size blocks, which are further classified into blocks containing vessels and non-vessels by measuring the entropy value. Those blocks containing vessels are utilized by a vessel extracting process. This method has two limitations:

first, two types of parameters need to be set (parameters relating to the ant colony and the CMF) and this may reduce the robustness of approach. Second, the segmented vessels are thicker than those vessels identified in ground truth (manual annotation of vessels). This tends to increase the FPR, and reduce the practicality of the application, since one of the applications of vessel segmentation is to measure the width of vessels which manifest pathological changes in images.

Zhang et al. [89] proposed a novel extension of the CMF approach named MF-FDOG to detect vessel structures and distinguish the vessels from edges of non-vessel structures. It segments the vessel objects by thresholding the retinal image's response to a zero-mean Gaussian function, whilst using the local mean of the response to the first-order derivative of Gaussian (FDOG) to adjust the threshold level in order to remove the non-vessel edges. The algorithm is developed based on the fact that the cross-section of a vessel is a symmetric Gaussian function but the step edge is asymmetric. Experimental results using MF-FDOG reveal that the MF-FDOG optimizes the CMF by reducing the false detections, whilst the CMF function is enhanced by detecting many fine vessels which are miss-detected by the CMF. A limitation of the method is that the segmentation is sensitive to noise and so some noisy patterns may be detected as vessels.

Hoover et al. [90] proposed a vessel segmentation method based on local and global vessel features. The segmentation is implemented using local vessel attributes and region-based attributes. The responses of the CMF are analysed in pieces and thresholded using an interactive probing technique. At each iteration step, a decision to continue to extend the probe is assessed by region-based attributes in tested pieces whilst pixels in such pieces are segmented as vessel or non-vessel. Pixels which are not detected as vascular candidates by the probe are recycled for further probing. Their comparative evaluation results demonstrate that the proposed method reaches about 80% sensitivity and 90% specificity.

In the literature [91], the matched filter is combined with other categories of filter as a general tool to enhance the vascular structure. Wu et al. particularly focused on dealing with the capability of detecting thin vessels. The framework of their method can be split into three steps: a pre-processing step, a vessel enhancement step and a segmentation step. In the pre-processing step they remove the image noise and smooth the image by a nonlinear diffusion technique, which is able to smooth the image without blurring vessels boundaries. In the vessel enhancement step, they use a compound filter bank which combines Hessian-based

filters, matched filters, and incorporates edge constraints of vessels. The advantage of employing a Hessian based filter is that it can enhance vessels of various sizes and estimate their directions simultaneously. However, Hessian-based filters can't distinguish step edges from vessels effectively. A CMF is employed by considering its effectiveness on distinguishing step edges from vessels. To solve the problem of false detection of edges using the CMF, they analyse the edge information at the boundary of vessels based on an assumption that a vessel should have two edges on each side of it. In the segmentation step, the vessels are tracked by a ridge-based algorithm, in which the multiple seeds are obtained by multiple thresholds of the enhanced image, and the ridges are determined according to the orientation and size information which are obtained from the enhancement filter.

Table 2-2 Performances of matched filtering based retinal vessel segmentation approaches

Method	**Year**	**Database**	**Sensitivity**	**Specificity**	**Accuracy**	**Area under the ROC (AUC)**
Chaudhure et al.[85]	1989	DRIVE	-	-	0.8773	0.7878
Hoover et al.[90]	2000	STARE	0.6751	0.9567	0.9275	-
Wu et al.[91]	2007	DRIVE	0.84	0.81	-	-
Al-Rawi et al.[87]	2007	DRIVE	-	-	0.9535	0.9435
Cinsdikici and Aydin[88]	2009	DRIVE	-	-	0.9293	0.9407
Zhang et al.[89]	2010	STARE	0.7177	0.9753	0.9484	-
		DRIVE	0.7120	0.9724	0.9382	-
Li et al.[92]	2012	STARE	0.8069	0.958	0.9461	-
		DRIVE	0.7154	0.9716	0.9343	-
Odstrcilik et al. [93]	2013	STARE	0.7847	0.9512	0.9341	0.9569
		DRIVE	0.7060	0.9693	0.9340	0.9519

Li et al. [92] proposed multi-scale vessel extraction scheme based on matched filter responses at 3 scales with optimized parameters. Each scale is designed to extract specific widths of vessels, of which the first scale is used to enhance thin vessels and third scale is for wide vessels. The middle scale can generate appropriate responses for both tiny and wide vessels. The parameters are optimized by detecting the maximal filter responses through scale space. The final segmentation is derived from a double-thresholding procedure based on selected responses at two scales. Experimental results demonstrated the performance of their simple and effective method.

More recently, Odstrcilik et al. [93] proposed a novel method for retinal vessel segmentation in which a matched filtering process is improved. After performing illumination correction and contrast equalisation of the fundus image in a pre-processing stage, the pre-processed image is then convolved with each of the filter kernels. Then each maximal response is combined into one map. Five 2-D filters which cover five different blood vessel widths were designed according to blood vessel cross-sectional intensity profiles. These filter kernels are designed by fully considering the vessel reflection issues, whilst each designed filter kernel is rotated into 12 different orientations in order to cover all possible vessels' directions. The segmentation is derived by applying a thresholding method on such a map. The proposed approach is evaluated on their new high-resolution fundus image database (HRF), DRIVE and STARE, respectively.

We summarise the performances of the matched filter based retinal fundus image vessel segmentation approaches we reviewed in table 2.2. To present the comparative performance of those methods under the same circumstance, we list methods which are evaluated on either DRIVE or STARE databases or both. The measurements use either a set of evaluated terms (sensitivity, specificity and accuracy) or a figure representing the area under the ROC (AUC) (see section 2.1 for more details). All data are collected from the respective published papers.

2.3.2 Methods tracing vessel structures

Segmentation approaches that trace retinal vessels are also known as tracking based approaches and tend to work particularly well on a single retinal vessel rather than on a whole image. Commonly, an algorithm starts from initialising points of interest on the vessel or detecting its centreline by connecting each pixel at the centre of the longitudinal cross-section of a vessel. Then the optimized path which matches a vessel profile model according to some local information is traced outwards in directions which the vessels spread. The points of interest in respect of vessels can be detected using vessel feature extraction techniques (e.g. matched filters), whilst different sketching techniques can be adopted for detection of the vessel centreline. The advantage of segmentation techniques that trace vessels is that the corresponding vessel segmentations have accurate width and these features are important signs for pathology assessment, e.g. vessel diameter measurement for diagnosis of hypertension. However, vessel tracing methods have limitations for detecting some branches of vessels, such as arterioles and venules, as vessel crossings produce occlusions which may

interfere with the tracing procedure. Also some branches may be excluded if initial points (seeds) are not identified within those branches.

Echevarria and Miller [94] reported a method that utilizes the level set method [117] to remove the noise followed by using a fast marching method to trace the vessels. Initially, they use a CMF to enhance the contrast of vessels. An iterative tracing process is implemented using the fast marching method, in which initial seeds placed at interfaces within major vessels are spread until all pixels of the image are covered. In this procedure, a double thresholding technique is employed to locate regions of vessels pixels and seed the interface. In the spreading process, a speed function (F) of a seed interface is constructed, which takes into account the gradient of areas in the image and the curvature of the interface. The interface is propagated by solving the boundary formulation differential equation $|\nabla T(x,y)|F = 1$, where $T(x,y)$ donates the time the interface passes through a point(x,y) in the image. The minimum time value of each pixel is used in the tracing step to judge whether the pixel belongs to vessels or not. This procedure runs until all the interfaces are stable. The output of the fast matching method is then revised by a level set method to get the final segmentation.

Wu et al. [95] proposed an automated blood vessel segmentation method which combines a vessel enhancing step, feature extraction step, and vessel tracing step. They employ an adaptive histogram equalization (AHE) technique to enhance the vessel from the background. To classify the blood vessels and non-vessel objects, the different texture features of both vessels and non-vessels structures are obtained by using a shape-based standard deviation filter (GS). The significant function of the feature extraction stage is detecting the small vessels, since these produce a significant response to the GS. The contrast-enhanced map and GS-filtering map obtained from the previous two steps are further used to track the larger and small vessels in the vessel tracing step. In their method, initial seeds are set by combining results obtained through three ways. First, the Sobel detector is applied on the contrast-enhanced map to obtain edges of large vessels. Second, local maximal points are selected from the GS-filtering map as candidates. Third, the local maxima from the responses to a CMF are also calculated as candidates. The tracing process starts from the seeds and proceeds in a forward detection, employing bifurcation identification and backward verification. The drawbacks of this vessel tracing method are firstly the performance depends on the selected seeds. The authors report that most false detections are due to incorrectly identified initial

seeds. Secondly, there are lots of 'rags' on each blood capillary in the segmentation result. The method is evaluated on the STARE database and the authors report 84.3% sensitivity and 96.1% specificity.

Tolias and Panas [96] proposed a new unsupervised fuzzy algorithm to track vessels. In their method, the optic disc (OD) is detected and used as a starting point for the vessel tracing procedure. The pixels on the circular boundary of the optic nerve are detected and formed into a sequence. These detected pixels are further classified into vessel and non-vessel regions using the fuzzy C-means (FCM) clustering algorithm. Within each classified vessel relative region three dark pixels are initially defined as vessels. Then the centres of these regions are defined as seeds. A fuzzy vessel tracking procedure is applied on each selected seed. The vessels are tracked by finding membership functions of two structures (vessels and non-vessels). More vascular memberships of pixels on the profile indicate a higher possibility that the pixel belongs to a vessel. The advantage of the proposed method is that only local intensity information is used unlike other vessel tracing methods which may demand information on more complex profiles (e.g. edge information). This advantage makes the method more automatic and efficient. Additionally, the method has robust performance and is able to deal with vessel junctions. The significance of this method is that it can be used to trace vessels in images from other modalities of angiography [96].

In the literature [97], Chutatape and Zheng proposed a retinal vessel tracking scheme which employs a second-derivative Gaussian, matched filter and extended Kalman filter. The second derivative Gaussian is used to locate initial points and detect the width of vessels. The extended Kalman filter is used to estimate the next possible location of vessel pixels. The vessel tracing process starts from the circular boundary of the optic disc (OD) and local maxima of the response to the matched filter define the centre of the blood vessel sources. In the vessel tracing process, a source pool is constructed, in which every source (seed) is considered as a potential starting point of a vessel, and the Kalman filter is initialized on the start point taking into account its direction. The optimal estimation of the next position is given by the Kalman filter, and then the Gaussian filter locates the next vessel segment based on the estimated position and direction. If the filter detects pixels on branching vessels then these points are added to the source pool as another source seed. This iteration continues until the endpoint is detected by the Gaussian filter.

A novel multi-scale line-tracking scheme is proposed for retinal vessel segmentation by Vlachos and Dermatas [98]. The algorithm starts by selecting potential seeds according to a brightness selection rule and the procedure continues until a cross-sectional profile condition becomes invalid. Multiple individual image maps relating to each scale are combined to generate the multi-scale image map, which contains the estimated confidence of vessels related to pixels. The initial segmentation is obtained by quantising the map which is represented as a multi-scale confidence matrix. The final segmentation is generated by using a median filter to join disconnected vascular fragments followed by a post-processing stage to remove the false positives. The proposed method is evaluated on the DRIVE database by measurements of the sensitivity, specificity and accuracy. The results show that the average accuracy of the proposed algorithm is 0.929 with values of 0.747 sensitivity and 0.955 specificity. The major limitation of the method is that it is sensitive to noise and abnormities in images thus the vessel segmentation results may contain non-vessel objects. This results in correspondingly high misclassification rate.

Delibasis et al. [99] proposed a vessel tracing segmentation method. The tracing routine uses a geometric model to represent the vessel (strip) which is used to discover the relation between the fitted model diameter and vessels diameter. A set of initial seed points located close to the vessel centreline are detected and each candidate is considered by a model matching routine which takes into account the local strip orientation and measurements to constrain the search space. The vessel diameter found by the matching algorithm is used to segment the vessels. The proposed algorithm is very effective however it exhibits a stochastic behaviour which is caused by an initialization procedure that employs random seeds. The proposed method is evaluated on the DRIVE database. The results demonstrated 72.88±0.63 sensitivity, 95.05±0.35 specificity and 93.11±0.34 accuracy.

A principal curve based retinal vessel segmentation approach is proposed by You et al. [100]. The appearances of vessels are enhanced using an isotropic Gaussian kernel and Frangi filter. A multi-scale principal curve projection is applied to associate pixels to vessel ridges and the branches of each ridge are then traced recursively by the principal curve tracing algorithm. The tracing procedure starts from a candidate seed on the principal curve, and then the vessel centre lines can be traced through the tangent subspace according to proper directions and step length. The approach is implemented and evaluated on the DRIVE

database. The corresponding measurements of performance (sensitivity, specificity and accuracy) are 0.8033, 0.9594 and 0.9456, respectively.

Ocbagabir et al. [101] proposed a novel ruled-based tracing algorithm for retinal vessel segmentation, which is called a star networked pixel tracking algorithm. Following a pre-processing and vessel enhancement procedure, each pixel of the entire image is compared with its four neighbouring pixels aligned at 45° in the tracking process. Using local information, pixel connections along eight orientations are checked iteratively and pixels are classified as vessels or not. The major advantage of the tracking algorithm is that it is able to reduce the interference due to noise and artefacts in the image when tracing the vessel structures. The proposed method is evaluated on the DRIVE database and achieved overall 95.83% accuracy.

Table 2.3 illustrates the evaluated performances, the sensitivity, specificity, accuracy and AUC measured on the DRIVE or STARE databases. Some vessel tracing methods reviewed above are excluded from the table, as those methods were evaluated by neither DRIVE nor STARE, or published without any evaluation results.

Table 2-3 Performances of tracing based retinal vessel segmentation approaches

Method	Year	Database	Sensitivity	Specificity	Accuracy	(AUC)
Wu et al.[95]	2006	STARE	0.8430	0.9610	-	-
M. Vlachos and E. Dermatas[98]	2010	DRIVE	0.7470	0.9550	0.9290	-
Delibasis et al.[99]	2010	DRIVE	0.7290	0.9510	0.9310	-
You et al. [100]	2011	DRIVE	0.8033	0.9594	0.9456	-
Ocbagabir et al.[101]	2013	DRIVE	0.7130	0.9820	0.9580	-

2.3.3 Classifier based methods

The basis of classifier based retinal vessel segmentation methods is that an unknown element or pattern within the fundus image is categorized to vessel or non-vessel by algorithms according to various forms of features. Commonly, this procedure is divided into two stages: first, the connected spatial regions with corresponding features are detected by a low-level algorithm. Then those candidate regions are classified into vessel or non-vessel (background) based on the extracted features. According to differences of classifier training schemes, the approaches for vessel segmentation can be divided into two categories: supervised and unsupervised approaches. The supervised retinal vessel segmentation approaches need

information from prior labelling which is provided in a training stage. The labelling information provides indications of vessels or non-vessel structures in a set of training sample images. Conventionally, the experimental training data may provide such segmented reference images known as ground truth which are produced manually by some expert observers. For instance, the ground truth vessels are marked or labelled precisely by one or more ophthalmologists. As the name implies, the unsupervised approaches perform the vessel segmentation without aid of any prior manual labelling information. The classifier or model of unsupervised methods are trained in order to expose the inherent characteristic features of vessel and non-vessel structures in retinal images that subsequently are used as criteria to determine whether a pixel belongs to vessel or not. The following reviews of segmentation methods based on vessel segmenting are categorised into supervised and unsupervised approaches, respectively.

- **Supervised classifier-based retinal vessel segmentation on fundus images**

Staal et al. [102] proposed a classifier based retinal vessel segmentation based on extraction of vessel ridges. The detected ridges are used to extract the vessel primitives (line elements) which are defined as a coordinate frame for partitioning an image into convex set regions by assigning each pixel to the closest line element. For every pixel, features are calculated from a convex set of regions that follows a feature selection scheme using a sequential forward selection method. The kNN classifier is applied for classification of the feature vectors. The method is evaluated on two databases. One is the Utrecht database which is obtained from a screening program in the Netherlands, and the other one is STARE. The results outperform the method proposed by Hoover et al. [90] and it achieved 0.9516 accuracy with 0.9614 AUC.

Soares et al. [103] proposed a scheme using the 2D Gabor wavelet to implement noise filtering and feature extraction. Then they used a Gaussian mixture model (GMM) classifier which is derived from a Bayesian classifier to determine whether a pixel is vessel or not. Each class-conditional probability density functions is described as a linear combination of Gaussian functions. The pixel's feature vectors are composed of the pixel's intensity and 2-D Gabor wavelet transform responses. Extraction of feature vectors is based on a 2-D Gabor wavelet basis which is a complex exponential modulated Gaussian that can be fine-tuned to specific frequencies and is capable of detecting oriented features. The classifier is trained based on manual segmentations of training images. Their experimental results demonstrate

that the GMM classifier has good performance which achieves 0.9466 sensitivity on DRIVE AND 0.9480 sensitivity on STARE.

In paper [104], Ricci and Perfetti proposed a retinal vessel segmentation technique based on a simple line operator. The method is composed of a feature extraction stage and a classification stage. Three categories of features were taken into account to generate feature vectors. Linear features of vessels were calculated based on the average grey level along lines of 15 pixels length passing through the target pixel at 12 orientations. A line of three pixels length which is orthogonal to the main line was employed to discriminate features of inside vessel pixels. Additionally, the grey level of the pixel was considered as a third feature. In the classification stage, they proposed two schemes for vessel classification. They adopted unsupervised classification by thresholding on the basic line detector's responses in the first scheme, which is further developed in the second supervised scheme by employing a linear support vector machine (SVM) as a classifier. The proposed approach only requires a small training set for vessel classification according to the produced features. Experimental results are evaluated on the STARE and DRIVE database, resulting in average accuracy of 0.9646 and 0.9595, respectively. The area under the ROC (AUC) is 0.9680, 0.9633.

Rezatofighi et al.[105] employed the contourlet transform technique to enhance the vessel contrast from background that contributes to detect capillaries from the low contrast fundus image. The features are produced by Local Binary Pattern (LBP) and morphological methods. The classification is implemented by using the adaptive Multi-Layer Perceptron (MLP), Artificial Neural Networks and Adaptive Neuro-Fuzzy Inference System (ANFIS), respectively. The comparative results demonstrate that the performance of ANFIS classifier is better than the MLP classifier, where the MLP classifier achieves accuracy of 0.9221, sensitivity of 0.6944 and specificity of 0.968, however the ANFIS achieves relatively better measurement, with accuracy of 0.9410, sensitivity of 0.7308, and 0.9723 specificity based on evaluation of the DRIVE database.

Moin et al. [106] presented a low dimensional feature vector extraction method for vessel and non-vessel classification. Four features were obtained by implementing Gabor wavelet and Local Binary Patterns (LBP). For extracting those rotation variant features, the Gabor kernels were rotated on 18 different orientations. For extracting rotation and gradient invariant features, rotation invariant LBP was employed. The supervised classification is

based on training the GMM classifier which is the same as Soares et al. employed [103]. Their computational results show the high efficiency of the proposed method.

Lupascu and Tegolo et al. [107] collected various vessel relative features based on the local, spatial and structural properties of vessels. A 41-D feature vector was generated for each pixel in the image. These feature vectors consist of responses of different filters. Features from vessel boundaries were calculated by a Gaussian related filter (first and second order derivative Gaussian) and vessel likelihood features were obtained by matched filters at multiple scales. Spatial features were measured by Frangi, Lindeberg and Staal measurements [107]. Gabor wavelet transforms were employed to enhance vessel contrast. Intensity features were obtained by numerical estimators. The classification is implemented using the AdaBoost classifier which is an iterative boosting algorithm. In this approach a strong classifier is produced by a weighted combination of weak classifiers in the algorithm. The AdaBoost classifier is trained on 789914 gold standard samples of vessel and nonvessel pixels. The proposed method is tested on the DRIVE database and it achieves 0.9561 AUC with 0.9567 accuracy.

Marín et al. [108] proposed a novel supervised method for retinal vessel segmentation in digital retinal images. The method adopts a neural network (NN) to achieve a pixel classification task based on a 7-D feature vector at each pixel which comprises grey-level and moment invariants-based features. The procedure includes four stages: first pre-processing for enhancing the vessels appearance. Second, vessels feature extraction for pixel characterization which can be used in the classification stage. In this stage, each pixel is characterized by a vector in a 7-D vector space. Third, classification is implemented to determine whether the pixels belong to vessels or not. The classification step handles the following two tasks: training and application. The NN configuration is initialized before the NN is trained in the training step. The output of the application task is a vessel probability map. In order to get the binary segmentation, a thresholding scheme on the probability map is employed. Finally, the pixel gaps are filled and over-segmentations are removed in the post-processing stage. The method was evaluated on both DRIVE and STARE databases and the experimental results present accuracy of DRIVE and STARE is 0.9454 and 0.9525, respectively.

Selvathi and P. Lalitha Vaishnavi [109], compare a support vector machine (SVM) classifier and relevance vector machine (RVM) classifier for retinal vessel segmentation.

Each classifier is used to classify each pixel as vessel or non-vessel based on the pixel's feature vectors, which are produced by using a Gabor wavelet combined with the pixel's intensity information. They investigate and compare the two classifiers on the STARE database. As a result, their experimental results suggest that the SVM classifier produces better results than the RVM classifier, which achieves 0.6585 sensitivity, 0.9666 specificity and 0.9447 accuracy, however the RVM takes less time and incurs less computational cost.

Fraz et al. [110] proposed a supervised retinal vessel segmentation method according to a 7-D feature vector. The features for each pixel are extracted using a combination of multi-scale Gabor filters, line strengths and morphological transformation. The Gabor filters and line strengths are sensitive to the area containing pathologies in the fundus image, so the morphological top-hat transformation is employed to deal with such issues. The segmentation is obtained by using a Gaussian Mixture Model (GMM) classifier. The method is evaluated using the images of both DRIVE and STARE databases resulting in average sensitivity of 0.7525, average specificity of 0.9722, and average accuracy of 0.9476 on the DRIVE database and 0.7604 sensitivity, 0.9812 specificity and 0.9579 accuracy on the STARE database. The area under the ROC curve is also measured for each database and the result demonstrates AUCs of 0.9616 and 0.9734 for the DRIVE and STARE databases, respectively.

Condurache and Mertins [111] proposed a novel scheme to design a fast and accurate classifier for binary classification purposes. Several classifiers are designed for segmenting vessel from background in the scheme. Two optimized classifiers are produced: pessimist and optimist, of which the former one represents the high-confidence classifier and works with a practically zero false-positive rate and a high false-negative rate, the latter one is the low-confidence classifier and works with a practically zero false-negative rate and a high false-positive rate. The classification is implemented based on a multidimensional feature vector for each pixel. The vessel relative features are obtained based on five different vessel maps which are generated by employing 5 categories of transforms: Bot-hat transform, Hessian transform at a single scale; multi-scale Hessian transform, Band-pass filter and Laplacian pyramid transform. The proposed scheme is tested and evaluated on both DRIVE and STARE. The experimental results show sensitivity of 0.9094, specificity of 0.9591, accuracy of 0.9516 and AUC of 0.9094 on DRIVE database, whilst sensitivity, specificity, accuracy and AUC of STARE database are 0.9094 0.9094, 0.9591 and 0.9516, respectively.

Table 2-4 Performances of supervised classifier-based retinal vessel segmentation approaches

Method	Classifier	Year	Database	Sensitivity	Specificity	Accuracy	(AUC)
Staal et al. [102]	kNN	2004	DRIVE	0.7194	0.9773	0.9441	-
			STARE	-	-	0.9516	0.9614
Soares et al.[103]	GMM	2006	DRIVE	-	-	0.9466	0.9614
			STARE	-	-	0.9480	0.9671
Ricci & Perfetti [104]	SVM	2007	DRIVE	-	-	0.9595	0.9633
			STARE	-	-	0.9646	0.9680
Rezatofighi et al.[105]	ANFIS	2008	DRIVE	0.7308	0.9723	0.9410	-
Moin et al. [106]	GMM	2010	DRIVE	-	-	0.9447	0.9515
Lupascu et al. [107]	AdaBoost	2010	DRIVE	-	-	0.9561	0.9567
Marín et al. [108]	NN	2011	DRIVE	0.7067	0.9801	0.9454	0.9588
			STARE	0.6944	0.9819	0.9526	0.9769
Selvathi et al. [109]	SVM	2011	STARE	0.6585	0.9666	0.9447	-
Fraz et al. [110]	GMM	2011	DRIVE	0.7525	0.9722	0.9476	0.9616
			STARE	0.7604	0.9812	0.9597	0.9734
Condurache & Mertins et al. [111]	hysteresis -classifier	2012	DRIVE	0.9094	0.9591	0.9516	0.9726
			STARE	0.8902	0.9673	0.9595	0.9791

We summarize measurements of the reviewed supervised classifier-based vessel segmentation method on fundus images in table 2.4, in which the contents are categorized by rows with corresponding authors and classifiers.

- **Unsupervised classification methods**

Salem et al.[112] proposed a radius based clustering algorithm (RACAL) for segmentation of blood vessels from colour fundus images. The proposed algorithm uses a distance based principle to map the distribution of the image pixels, where the number of clusters does not have to be specified. The features extracted from the image can then be clustered by the RACAL. These features include: pixel intensity of the green channel; the local maxima of the gradient magnitude; and the local maxima of the largest eigenvalue of the Hessian matrix. A comparison of the proposed algorithm and a kNN classifier is implemented. As a result, they conclude that the RACAL performs better than the kNN in the case of detecting capillaries. In the segmentation stage, the RACAL is aided by a partial supervision strategy and defined as a classifier for vessel classification, in which the trained clusters are assigned to corresponding manually defined classes of ground truth images. The proposed method achieves sensitivity of 0.8215 and specificity of 0.9750 on the STARE database.

Kande et al. [113] proposed a retinal vessel segmentation method using the pixel intensity information from both red and green channels to adjust the non-uniform illumination in the colour fundus images, followed by a vessel enhancement stage by using matched filtering. Enhanced vessels are segmented by adopting spatially weighted fuzzy C-means cluster based thresholding, which takes the spatial distribution of image pixel intensities into account. The final segmentation is obtained by using label filtering to remove some misclassified pixels. The proposed method is evaluated on the DRIVE and STARE databases and it achieves an area under the ROC (AUC) of 0.9518 and 0.9602, an accuracy of 0.8911 and 0.8976, respectively.

In [114], Oliveira et al. proposed an unsupervised retinal vessel segmentation procedure using a combined filter which includes a matched filter, Frangi filter and Gabor filter. The combined filter is used for vessel enhancement and corresponding feature extraction. The extracted features are then clustered by a fuzzy C-means algorithm (FCM) to implement vessel segmentation based on their observation that the number of non-vessel elements is larger than vessel elements. Consequently, one of the clustering group is used to indicate the group of vessels pixels. The proposed unsupervised retinal vessel segmentation is tested and evaluated on both DRIVE and STARE databases, which achieves accuracies of 0.9580 and 0.9582, respectively.

Wang et al. [115] proposed an unsupervised retinal vessel segmentation method which does not require pre-processing. The vessels are initially enhanced by using a matched filtering with a multi-wavelet kernel in which the multi-wavelet kernel is capable of responding to blood vessels and non-vessel edges. The classification of vessel and non-vessel is implemented by using an iterative multi-scale hierarchical decomposition algorithm based on a two-class decomposition model, which is controlled by one optimal scale parameter. The final binary segmentation is derived from adopting an adaptive thresholding. The proposed novel method is evaluated on both DRIVE and STARE databases. For those images of DRIVE, it achieves an accuracy of 0.9441 and AUC of 0.9543, whilst the performance measurement, accuracy and AUC on STARE is 0.9521 and 0.9682, respectively.

Table 2.5 summarizes each proposed unsupervised retinal vessel segmentation method on colour fundus images, in which those methods are indicated by the corresponding classification algorithm.

Table 2-5 Performance of unsupervised classification based retinal vessel segmentation approaches

Method	Algorithm	Year	Database	Sensitivity	Specificity	Accuracy	(AUC)
Salem et al.[112]	RACAL	2007	STARE	0.8215	0.975	-	-
Kande et al. [113]	FCM	2010	DRIVE	-	-	0.8911	0.9518
			STARE	-	-	0.8976	0.9602
Oliveira et al. [114]	FCM	2012	DRIVE	-	-	0.9580	-
			STARE	-	-	0.9582	-
Wang et al. [115]	Hierarchical Decomposition	2013	DRIVE	-	-	0.9441	0.9543
			STARE	-	-	0.9521	0.9682

2.3.4 Model based methods

Model based retinal vessel segmentation methods aim to detect the inherent vessel model to extract the vessels tree. Two representative categories of the model-based approach are the vessel profile model and the deformable model. The principle of the vessel profile model is that the intensity profile across a blood vessel can be described by a specific model such as Gaussian or derivative of Gaussian. The latter model describes where light is reflected within the vessel. In this case, the matched filter [85] which we described in section 2.3.1 also can be categorized as a model or template-based segmentation method. Conventionally, the computation of a deformable model can be described as a procedure that initialises a parametric curve or surface close to the objects of interest, and then deforms it iteratively towards to the objects' boundary until the process reaches convergence. According to different contour representations, deformable models can be divided into parametric and geometric models. A representative parametric model is an active contour model which is known as a 'snake' initially introduced by Kass et al. [116]. A snake is first initialled on the area close to the boundary of objects, and then the snake expands to fit the shape of the desired object according to an internal and external force. The internal force is used to constrain the snake's contour while the external force attracts the contour to objects according to desirable features. The geometric deformable model is based on the level set method [117], which is a numerical technique for tracking shapes. The moving contour is characterized as a zero level set of a higher dimensional level set function. The following model-based retinal vessel segmentation approaches on fundus images are reviewed by corresponding categories.

Wang et al. [118] proposed a retinal vessel segmentation algorithm based on a multi-resolution Hermite model. Blood vessel profiles are modelled as a 2-D Hermite function

intensity model in a quad-tree structure over a range of spatial resolutions. A Gaussian intensity model is employed to model local vessel features, of which the optimized parameters are further estimated by using an expectation-maximization (EM) scheme. The final global vessel tree is obtained by linking the local features using Bayesian stochastic inference. The developed model has robust performance to detect various types of vessels which includes handling those vessels that exhibit refraction artefacts. The algorithm is evaluated on both STARE and DRIVE databases. Sensitivity of 0.820, specificity of 0.933 for the STARE database and sensitivity of 0.841, specificity of 0.966 for the DRIVE database are reported.

Lam et al. [119] employed the concavity in the intensity profile to model vessel or non-vessel planes in order to segment vessels from background in fundus images. The proposed method is able to segment the vessel on both normal images and abnormal images (i.e. those containing exudates etc.). Different concavity measures are used to model hard exudate, haemorrhages, and vessels, respectively after applying a perceptive transform in a pre-processing stage. The steep intensity transition pattern that characterises hard exudates is used to distinguish them from other objects, whilst as the haemorrhages exhibit an irregular shape intensity structure and blood vessels have a line-shape intensity structure, a line-shape concavity detection algorithm is proposed to model the vessel and exclude haemorrhages. The global vessel tree that is detected relies on combining these concavity measures according to their statistical distributions. The measurement of performance (accuracy and AUC) for the DRIVE database is 0.9472 and 0.9614, respectively. For the STARE database, the accuracy is 0.9567 and AUC is 0.9739.

Espona et al. [120] proposed an active contour model (snake) based retinal vessel segmentation method. Initially, the vessel skeletons are extracted which can be used to initialize the snake and guide the contour evolution. The snake is initialized by intersecting the detected optical disc (OD) boundary and vessel skeletons. The external energy is modelled as an energy function which is composed of a set of energies and weighting factors. Instead of using a specific internal force, the vessel edge energy constrains the contour evolution when it expands along the vessel skeleton. The snake expands inside the vessel following an iterative algorithm to minimise these energy functions in order to obtain the vessel segmentation. The measurement of evaluation on the DRIVE database demonstrates that the accuracy, sensitivity and specificity are 0.9316, 0.6634 and 0.9682, respectively.

Al-Diri et al. [121] proposed a novel active contour model for retinal vessel segmentation and measurement. The proposed method integrates vessel segmentation and width measurement together, which comprises several stages. First, an initial set of potential vessel segment pixels is located by a tramline algorithm. Second, an active contour based model called 'Ribbon of Twins' (ROT) is applied to convert the tramline pixels into a set of segments. Each ROT contains four linked active contours, of which one pair of contours insides a vessel expand towards the internal edge, and the other pair of contours locate the outside edges and deform toward the internal contours. The contour energy function consists of internal, photometric and ROT energy parameters. The internal energy models the tension and rigidity of contours, the photometric energy is used to attract the contours towards edges, and the ROT model energy is used to capture the vessel's edges. Third, a junction resolution algorithm is developed to join up each vessel segment to produce the global vessel tree. The proposed method is evaluated on DRIVE and STARE databases and it achieves a sensitivity of 0.7282, specificity of 0.9551 on DRIVE and sensitivity of 0.7521 and specificity of 0.9681 on STARE.

Szpak and Tapamo [122] proposed a geometric deformable model based retinal vessel segmentation method which employs a fast level set method [124] without solving partial differential equations to extract the contour of the retinal vessels. The fast level set method [124] assumes that pixels in an image can be considered as the points on a grid. The neighbouring grid points inside the contour are represented as negative values and the points outside the contour are positive. A speed function of each pixel determined the evolution of the contour. In the proposed method [122], this function is formed by a binary pre-segmented vessel map which is obtained by applying a Laplacian of Gaussian on the pre-processed image to extract edges of vessels followed by thresholding. The vessel part of the binary vessel map constitutes a fixed positive speed, while the rest part of the map constitutes a fixed negative speed. This speed field guides the contour to gradually expand towards the vessel edges to obtain the final vessel tree segmentation. The proposed method achieves an average accuracy of 0.9299 on the DRIVE database.

In [123], the vessels properties are modelled by using a second derivative Gaussian filter. The response to the filter is further analysed to obtain the most probable parameters describing the vessel. The width, contrast and direction at each point on the blood vessel in the image are estimated. Homogeneous zero mean Gaussian noise with a statistical

autocorrelation function is chosen to produce a noise model in the background. The method is evaluated on the STARE database, and achieves 0.7000 sensitivity and 0.9530 specificity, respectively. Table 2.6 illustrates the measurements of performance using model-based retinal vessel segmentation methods.

Table 2-6 Performances of model based retinal vessel segmentation approaches

Method	Algorithm	Year	Database	Sensitivity	Specificity	Accuracy	AUC
Wang et al.[118]	Multi-resolution Hermite model	2007	DRIVE	0.841	0.966	-	-
			STATE	0.82	0.933	-	-
Espona et al. [120]	Snake	2007	DRIVE	0.6634	0.9682	0.9316	-
Szpak and Tapamo [122]	Geometric deformable model	2007	DRIVE	-	-	0.9299	-
Al-Diri et al. [121]	Ribbon of Twins	2009	DRIVE	0.7282	0.9551	-	-
			STATE	0.7521	0.9681	-	-
Ng et al.[123]	vessel profile model	2010	STARE	0.7000	0.9530	-	-
Lam[119]	Multi-concavity	2010	DRIVE	-	-	0.9472	0.9614
			STATE	-	-	0.9567	0.9739

Besides the four main categories of retinal vessel segmentation approaches reviewed above, a number of alternative methods have been proposed. Zana and Klein [125] employed an algorithm using mathematical morphology and cross-curvature evaluation to detect vascular patterns. The morphological properties of vessels are extracted by mathematical morphology, and then the cross-curvature evaluation is performed to eliminate similar patterns which are non-vessel related. Mendonca and Campiho [126] proposed a retinal vessel segmentation method combining centreline detection and morphological reconstruction. The vessel centrelines are extracted initially, and these guide the subsequent vessel filling phase. A complete segmentation of the retinal vessels is produced by a multi-scale approach followed by a simple region growing algorithm. In this stage a set of morphological operators is employed to generate several enhanced representations of vessels and then image masks containing binary reconstructions of the main vessel segments are derived from the enhanced representations by morphological reconstruction. The final segmentation is obtained by an iterative vessel filling procedure. Miri and Mahloojifar [127] employed a so called curvelet transform to enhance the vessel edges before a segmentation stage. The segmentation of the vessel tree is implemented by using morphology operators for reconstruction and length filtering. Graph techniques have also been employed for retinal segmentation in the literature [128]. To enhance the contrast between vessels and background,

Salazar-Gonzalez et al. [128] adopted adaptive histogram equalization. A binary morphological opening process was applied then the distance transform is used to generate a distance map which is used to construct a graph. Cai and Chung [129] used normalized cuts for retinal vessel segmentation. The algorithm employs a gradient matrix to locate a local candidate window which may contain vessels. Each candidate window is segmented using an intensity threshold which is calculated by minimizing the normalized cut criterion. Finally, a tracing strategy is utilized and segmentation results are optimized by avoiding noisy candidate windows. In the literature [130], an unsupervised retinal vessel segmentation based on a water flooding model is proposed. The method simulates the principle of water flooding also known as the watershed which exploits a digital elevation model.

We summarise evaluations of reviewed methods on DRIVE or STARE or both databases above in the table 2.7. Note: Cai and Chung is not included as no corresponding measurements are reported.

Table 2-7 Performances of other retinal vessel segmentation approaches

Method	Core Algorithm	Year	Database	Sensitivity	Specificity	Accuracy	AUC
Zana and Klein [125]	Mathematical morphology	2001	DRIVE	0.6696	0.9769	0.9377	-
Mendonca and Campiho [126]	Morphological econstruction	2006	DRIVE	0.7315	0.9781	0.9463	-
			STARE	0.7123	0.9458	0.9479	
Miri and Mahloojifar [127]	Morphological reconstruction	2011	DRIVE	0.7352	0.9795	0.9458	-
Salazar-Gonzalez [128]	Graph cut	2010	DRIVE	0.7197	0.9665	0.9479	-
			STATE	0.6782	0.9729	0.9478	-
Asad et al. [130]	Watershed	2013	DRIVE	0.6292	0.9821	0.9369	-

2.4 Chapter conclusion and discussion

Segmentation of retinal blood vessels in retinal fundus images is an essential stage in the retinal vessel analysis process. The morphological properties of retinal vessels provide important signs or evidence of several routine clinical diagnoses. This is particularly critical to diagnosis, screening, and treatment for various ophthalmologic diseases, such as Glaucoma, AMD, diabetic retinopathy (DR) and vascular disorders etc.. Automated assessment of vascular structures in the retinal fundus image is accepted in the clinical community as a critical stage in the development of a computer assisted diagnostic system for automated detection and grading various forms of retinopathy. In practice, the retinal vessel tree in the

retinal fundus image is primarily segmented manually by experts. However, the manual segmentation is quite time-consuming and the task demands considerable experience. As such, screening programs must consider the cost of workloads (training, labour force). This motivates studies of automatic segmentation of the blood vessel networks and a large number of approaches have been proposed. However, the challenges of developing accurate automatic retinal vessel segmentations are considerable and it remains a focus for ongoing research. Such challenges include the wide range of vascular width and tortuosity, presence of noise in each fundus image, the low and unstable local intensity contrast between vessels and background, presence of pathology elements, and presence of various optical artefacts such as reflection and refraction within vessels. In practice, the most difficult task of retinal vessel segmentation is to detect the tiny vessel (capillaries) from the background. There are no approaches which have been proposed that are able to segment all capillaries completely, to the best of our knowledge. Additionally, pathological changes presented in fundus images may be segmented as vessels. Reflection within vessels may be detected as non-vessel, as its colour intensity is quite different from the normal vessel. Under these circumstances, automatic retinal vessel segmentation remains a focus for improvements in performance due to the limitations of state-of-the-art methods. A large number of novel approaches have been proposed using various modern image processing and analysis techniques. These have been review in section 2.3. The methods are primarily divided into four categorizes;

(1) Matched filtering based segmentation,

(2) Vessel tracing/tracking based segmentation,

(3) Classifier based segmentation,

(4) Model-based segmentation.

Matched filtering is designed by considering known information that the vessel cross-sectional intensity profile can be approximated by a Gaussian shaped curve. As a specific linear detector, its simplicity attracts many research interests. However, the efficiency of algorithm may be affected by the size of designed filter kernel. Moreover, the designed kennel may not cover various widths of vessel, and has limitations for detecting those capillaries. One solution to enhance the filter kernel to detect vessels is that of optimizing the parameters of matcher filter via mathematical analysis and experiment simulation [86][87]. To overcome the limits of the matched filter, other imaging segmentation techniques are

combined with the matched filter. Such techniques are presented in reviewed methods [88][89][90]. A common solution to overcome the limit of capillary detection is increasing the number of kernels by using kernel at multi scales, where each scale is designed for specific vessel extraction purposes [92][93] or by introducing and working together with other categories of vessel enhancement filters [91]. The matched filter has specific ability to detect the linear structures in the image. Hence we believe it will remain a focus for ongoing research. For instance, it can be used as an assistant tool for vessel enhancement.

The tracing/tracking based retinal vessel segmentation method provides highly accurate measurement of vessel width and tortuosity. However, it has limitation for detecting some branches of vessels, such as arterioles and venules, as vessel crossing may influence the tracing procedure and the branch may be eliminated if the initializing points (seeds) are not placed on the branch. Meanwhile, the low contrast between capillaries and background may result in tracing failure. The tracing based method is very sensitive to the presence of noise. Good achievements of those methods also rely on two critical stages: the initializing and tracing stage, in which vessel centre lines or seeds need to be initialized using vessel enhancing filters, such as using matched filter [94][95], Gaussian derivative filters [97][100], and relying on seed selecting rules, for instance, selecting seeds from the optical disc[96][97], using a brightness selection rule [98] or guiding by vessel centreline [99]. In the tracing stage, the optimized path which matches a vessel profile model according to some local information is traced towards to the vessel spreading direction. The tracing process can be based on a speed function [94], can rely on the possibility of vessel pixel belonging to clustering group [96][98], and also can be a local vessel profile model [99][100][101].

The classifier based retinal vessel segmentation method is originated from the machine learning pattern recognition and classification research field. The achievement of classifier based methods relies on extracting characteristic features from vessel and non-vessel structures and training appropriate classifier based on such features. For classifier based segmentation methods, many feature extraction schemes have been proposed. For instance, extracting features based on several transforms (2-D Gabor wavelet, Hessian transform etc.) and local intensity [103][106][109][111][112]. Linear features are detected according to grey level [102][104], local vessel features are calculated by Local Binary Pattern (LBP)[105][106] and using combined filters to enhance the vessel and generate corresponding multi dimension feature vectors [107][108][113][114][115]. For supervised classifier based methods, in the

classification stage, different classifiers are employed, such as kNN[102], NN[108], GMM[103][106][110], SVM[104], ANFIS[105], AdaBoost[107] etc. For unsupervised classification methods, the extracted vessel related features may be clustered into a vessel group using a clustering algorithm such as RACAL [112] and fuzzy c-means (FCM)[113][114]. According to our investigation of classification methods, we find that most state-of-the-art supervised methods have better performances than unsupervised methods in healthy retinal fundus image, since the classifier is trained based on manually-labelled samples. However, the performance of supervised methods is very dependent on those pre-classified data, which may not be available in real applications. Moreover, as Hoover et al. [90] mentions, manual segmentation results may have significant differences varying from observer to observer, but the equality of ground truth may affect the trained classifier. This state is verified by our experiment which is presented in section 5.3. In practice, such issues have been an open problem which is challenging future work. Pursuing more accurate unsupervised methods which reduce dependences on the ground truth may handle such issues. Additionally, developing supervised methods which are capable of handling unhealthy fundus images may be the trend of future work.

Model based retinal vessel segmentation methods can be divided into vessel profile model and deformable model based approaches. Design of the vessel profile model is based on the intensity profile across a blood vessel being presented as a Gaussian or derivative Gaussian in the case of vessel reflection. In the literature [118][119][123], some specific vessel profile model are presented. According to different contour representations, the deformable models can be divided into parametric and geometric models. The good performance of the deformable model based approach depends on the designed internal and external energy function. The advantage of deformable model based segmentation is that it is capable of detecting tinny vessels if the evolution of contour is guided by an appropriate vessel centreline, whilst the detected diameter of the vessel is more close to the real width. The potential utilities of such method could be: detecting the vessels while measuring the vessel widths, so that vessel segmentation and measurement can be accomplished simultaneously. Al-Diri et al. [121] give a good example of such an application.

Besides four categories of retinal vessel segmentation, some alternative hybrid approaches are reviewed in this chapter. For instance, the morphological reconstruction technique is employed in approaches [125][126][127], The Graph cut technique is adopted in

[128]. A normalized cuts approach is used in [129], and a watershed method is implemented in [130].

Two commonly used evaluation methods are reviewed. The terms sensitivity and specificity are the factors which indicate success rate of classifying vessel and non-vessel pixels, respectively. The accuracy indicates an overall measurement that provides the ratio of total well classified pixels relative to ground truth. The receiver operating characteristic (ROC) curve is a general tool also used to measure the segmentation performance. An ROC curve plotted closer to the top left corner is indicative of better performance of the method. The area under the curve (AUC) can also be used as a performance index. Two publicly available databases DRIVE [132] and STARE [133] are introduced in section 2.2 as well.

We summarize the performance of reviewed approaches on the DRIVE database and the STARE database in table 2.8 and table 2.9 respectively. The methods are sorted by their published year, and corresponding measured terms are listed by each column.

The method proposed by Ricci & Perfetti [104] achieves the best accuracy and AUC on both databases. To provide a more intuitive view of those methods' performances in terms of sensitivity, specificity and accuracy, we plot the histogram for each method on both database in figure 2.2 and figure 2.3. Here the x-axis is the published year and y-axis represents accuracy, sensitivity and specificity on a scale with values ranging from 0.5 to1. The best sensitivity on DRIVE and STARE are 0.9094 and 0.8902, respectively, reported by Condurache & Mertins et al.[111].

Observing the tables and figures, we can see that average accuracies of 6 methods are over 0.95 on the DRIVE dataset, and average accuracies of 6 methods are over 0.95 on the STARE dataset as well. However, there are significant differences between sensitivity and specificity, indicated by the red and green pillars in both figures. We would like to emphasise that achieving better sensitivity without sacrificing specificity may be the focus of future research interest.

Table 2-8 Performance of previous retinal vessel segmentation methods on the DRIVE database

Method	Categories	Year	Database	Sensitivity	Specificity	Accuracy	(AUC)
chaudhure et al.[85]	MF	1989	DRIVE	-	-	0.8773	0.7878
Zana and Klein [125]	Mathematical morphology	2001	DRIVE	0.6696	0.9769	0.9377	-
Soares et al.[103]	supervised	2006	DRIVE	0.7283	0.9788	0.9466	0.9614
Mendonca and Campiho [126]	morphological reconstruction	2006	DRIVE	0.7315	0.9781	0.9463	-
Wu et al.[91]	MF	2007	DRIVE	0.84	0.81	-	-
Al-Rawi et al.[87]	MF	2007	DRIVE	-	-	0.9535	0.9435
Ricci & Perfetti [104]	supervised	2007	DRIVE	-	-	**0.9595**	**0.9633**
Wang et al.[118]	Hermite model	2007	DRIVE	0.841	0.966	-	-
Espona et al. [120]	Snake	2007	DRIVE	0.6634	0.9682	0.9316	-
Szpak and Tapamo [122]	Geometric deformable model	2007	DRIVE	-	-	0.9299	-
Rezatofighi et al.[105]	supervised	2008	DRIVE	0.7308	0.9723	0.941	-
Cinsdikici and Aydin[88]	MF	2009	DRIVE	-	-	0.9293	0.9407
Al-Diri et al. [121]	Snake	2009	DRIVE	0.7282	0.9551	-	-
Zhang et al.[89]	MF	2010	DRIVE	0.712	0.9724	0.9382	-
M. Vlachos and E. Dermatas[98]	Tracing	2010	DRIVE	0.747	0.955	0.929	-
Delibasis et al.[99]	Tracing	2010	DRIVE	0.7290	0.9510	0.9310	-
Moin et al. [106]	supervised	2010	DRIVE	-	-	0.9447	0.9515
Lupascu et al. [107]	supervised	2010	DRIVE	-	-	0.9561	0.9567
Kande et al. [113]	unsupervised	2010	DRIVE	-	-	0.8911	0.9518
Lam et al. [119]	Multi-concavity	2010	DRIVE	-	-	0.9472	0.9614
Salazar-Gonzalez[128]	Graph cut	2010	DRIVE	0.7197	0.9665	0.9479	-
You et al. [100]	Tracing	2011	DRIVE	0.8033	0.9594	0.9456	-
Marín et al. [108]	supervised	2011	DRIVE	0.7067	0.9801	0.9454	0.9588
Fraz et al. [110]	supervised	2011	DRIVE	0.7525	0.9722	0.9476	0.9616
Miri and Mahloojifar [127]	morphological reconstruction	2011	DRIVE	0.7352	0.9795	0.9458	-
Li et al.[92]	MF	2012	DRIVE	0.7154	0.9716	0.9343	-
Condurache & Mertins et al. [111]	supervised	2012	DRIVE	0.9094	0.9591	0.9516	0.9726
Oliveira et al. [114]	unsupervised	2012	DRIVE	-	-	0.958	-
Odstrcilik et al. [93]	MF	2013	DRIVE	0.706	0.9693	0.934	0.9519
Ocbagabir et al.[101]	Tracing	2013	DRIVE	0.7131	0.9824	0.9583	-
Wang et al. [115]	unsupervised	2013	DRIVE	-	-	0.9441	0.9543
Asad et al. [130]	Watershed	2013	DRIVE	0.6292	0.9821	0.9369	-

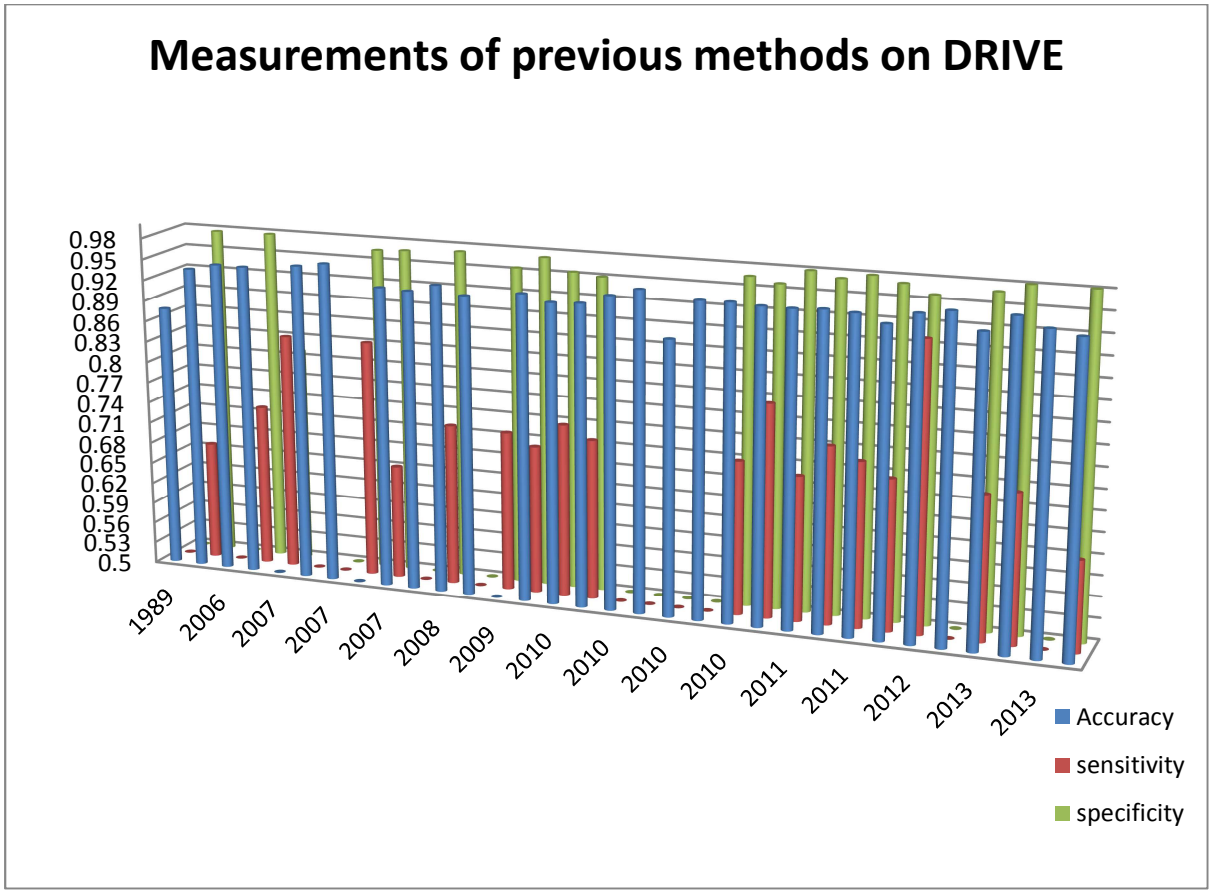

Figure 2.2 Histograms of terms: Accuracy (Blue), sensitivity (Red) and specificity (Green) on the DRIVE database

Table 2-9 Performance of previous retinal vessel segmentation methods on the STARE database

Method	Categories	Year	Database	Sensitivity	Specificity	Accuracy	(AUC)
Hoover et al.[90]	MF	2000	STARE	0.6751	0.9567	0.9275	-
Staal et al. [102]	supervised	2004	STARE	-	-	0.9516	0.9614
Wu et al.[95]	Tracing	2006	STARE	0.843	0.961	-	-
Soares et al.[103]	supervised	2006	STARE	-	-	0.948	0.9671
Ricci & Perfetti [104]	supervised	2007	STARE	-	-	0.9646	0.968
Salem et al.[112]	unsupervised	2007	STARE	0.8215	0.975	-	-
Zhang et al.[89]	MF	2010	STARE	0.7177	0.9753	0.9484	-
Kande et al. [113]	unsupervised	2010	STARE	-	-	0.8976	0.9602
Marín et al. [108]	supervised	2011	STARE	0.6944	0.9819	0.9526	0.9769
Selvathi et al. [109]	supervised	2011	STARE	0.6585	0.9666	0.9447	-
Fraz et al. [110]	supervised	2011	STARE	0.7604	0.9812	0.9597	0.9734
Li et al.[92]	MF	2012	STARE	0.8069	0.958	0.9461	-
Condurache & Mertins et al. [111]	supervised	2012	STARE	0.8902	0.9673	0.9595	0.9791
Oliveira et al. [114]	unsupervised	2012	STARE	-	-	0.9582	-
Odstrcilik et al. [93]	MF	2013	STARE	0.7847	0.9512	0.9341	0.9569

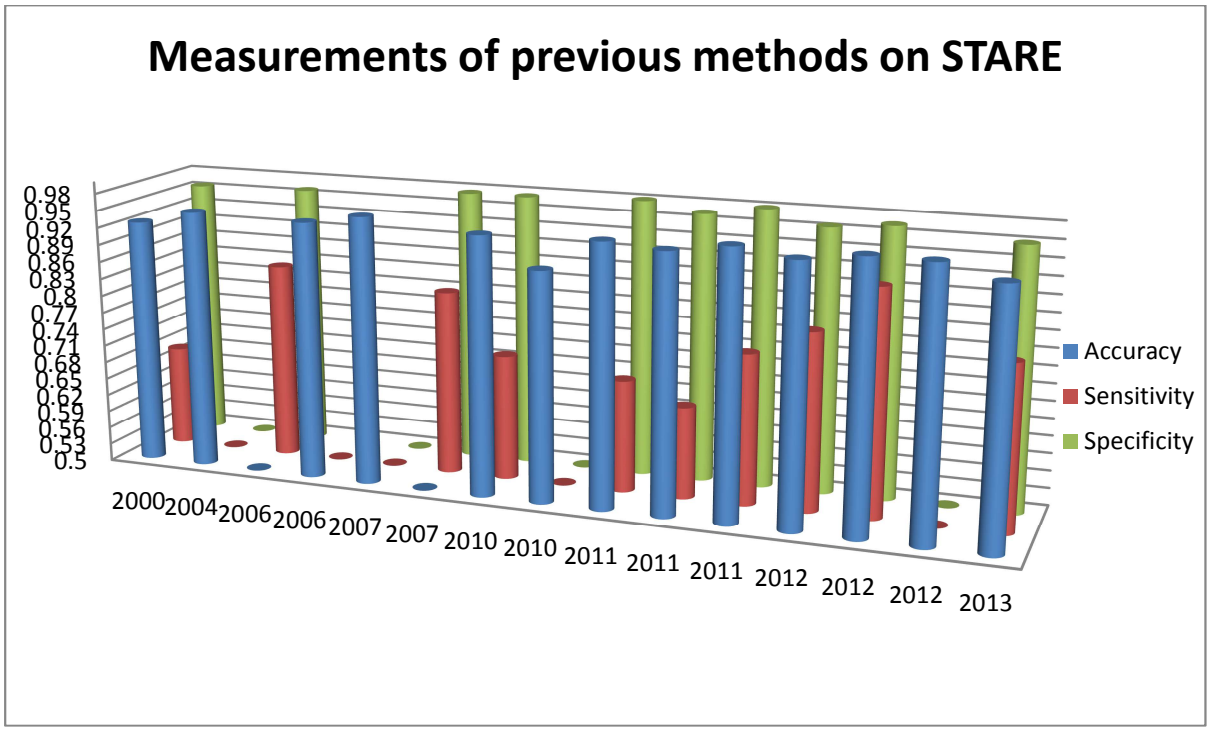

Figure 2.3 Histogram of terms: Accuracy (Blue), sensitivity (Red) and specificity (Green) on the STARE database

CHAPTER 3

3. Texture measure for segmentation

Putting aside the colour, grey level and regional intensity of an image, texture could be seen as another important element in distinguishing various patterns as it provides significant information regarding different visual features in images, i.e. those features that represent visually homogeneous patterns within the image. Smith gives a more specific description in [134], and defines texture as “homogeneous patterns or spatial arrangements of pixels that cannot be described sufficiently by regional intensity or colour alone” [134]. As such, texture has attracted extensive attention within the computer vision community and has been used to perform tasks such as object recognition, surface geometries analysis and image pattern classification etc. Image segmentation or shape detection is an important pre-processing stage in these tasks. Texture based image segmentation is a significant category of region based segmentation approaches. It has been adopted widely in applications of segmentation in images of natural scenes and has been particularly successful in content based image retrieval. Reed and Dubuf [141] present an exhaustive review of texture segmentation, in which they categorized the previous texture segmentation methods into feature based, model based and structural methods according to different feature extraction techniques they adopt. Numerous texture segmentation methods for natural images are proposed. For instance, Deng [135] presented a region growing method named as JSEG that takes colour-texture patterns into account. Blas et al. [136] proposed a fast integrated approach, in which the local colour and texture variations have been represented by a compact colour and texture descriptor. Fauzi and Lewis [137] extracted the features of image contents by a discrete wavelet frame and classified the image into different texture regions by combing the mean shift algorithm with fuzzy C-means clustering. Moreover, texture based segmentation approaches have been employed to address medical image segmentation tasks. He and Muhimmah et al. [138] presented a method which aims to segment mammographic images into mammographic building blocks (i.e. nodular, linear, homogeneous, and radiolucent structures). Our work is inspired by their achievements on mammographic x-ray images and also motivated by Varma and Zisserman’s work [139] which achieved success in classifying a range of natural texture

patterns. The framework provides an approach for learning texture features which is founded in human perception. However, only a few authors [140] have investigated structural texture based approaches for retinal vessel segmentation in fundus images. This motivates our focus on investigating texture discrimination techniques applied to retinal vessel segmentation in fundus images.

Texture analysis is a critical stage in image segmentation and texture classification, which is a procedure of characterizing the texture within images. In practice, the methodology and performance of the texture analysis component determines the quality of the image segmentation. To facilitate understanding of our work, in this chapter, we present an introduction to texture analysis methodologies which have been utilized in image segmentation. First, we introduce general categories of texture analysis methods in section 3.1, then corresponding structural and statistical feature characterizing methods are described in section 3.2. A brief summary of first- and second-order statistics and Markov random fields (MRF) is presented in subsections 3.2.1, 3.2.2 and 3.2.3, respectively. In subsections 3.2.4 and 3.2.5, the structural features characterizing maximal response and Gabor filters are introduced. In order to describe representative local texture features, local binary pattern (LBP) and scale invariant features are described in section 3.3. The chapter conclusion and discussion are presented in section 3.4.

3.1 Texture analysis methods

The primary aim of texture analysis in machine vision research is to detect, characterize, and process image texture. This is a mathematical procedure for measuring the spatial arrangement of grey values and modelling pixel inter-relationships within an image. Texture analysis is a critical stage in image processing, segmentation and texture classification, and it is critical to achieving good performance in many applications, such as object recognition, content based image retrieval etc.. Numerous methods have been proposed in the past few decades. Earlier attention in texture analysis is mainly focused on first- and second-order statistical analysis. Later on, model-based methods such as Gaussian Markov random fields were introduced and recently, the focus of research has turned to discovering local invariant texture features. Exhaustive reviews of existing texture analysis methods can be found in the literature [142][143] [150]. A review of texture measure and analysis approaches for texture segmentation is presented in [141]. Xie [144] presented a review of recent texture analysis

techniques for surface defect detection which has been viewed as a texture analysis problem. Several brief reviews of recent texture analysis techniques are presented in [145][146][147], where Zhang and Tan [147] focused on investigating invariant texture features analysis methods. Recently, texture has been seen as a powerful tool in image processing and texture analysis techniques have been extended to some medical image analysis applications. In the literature [148], texture analysis methods particularly focused on medical image applications are reviewed and Kassner and Thornhill [149] presented a review which considers applications involving neurologic MR images.

Descriptions that characterize texture by different mathematical procedures broadly fall into two categories: statistical methods and structural methods. By considering different forms of object representation (pixel, boundary or region), some authors [145][150] categorize the approaches into pixel based, local region based and region based methods. In the literature [143][142], some model based methods (such as autoregressive models, Markov random fields, Fractal models) are classified into a relatively independent category, and some convolution filtering based methods which derive from signal processing techniques are categorized into transform methods or filtering based methods. In this thesis, since combined spatial filter banks, Gabor filters and wavelet transforms are commonly used to describe structure primitives, we categorize filter based methods as structural methods. In our review, we adopt a similar approach to surveys of several texture analysis methods [142][143][144] [146][147][150], and categorise texture methods into: statistical methods, structural methods and model based methods.

3.1.1 Statistical methods

Commonly, statistical methods measure the spatial distribution of grey values and treat textures as statistical phenomena. The texture is represented as statistical distributions of the selected features which are computed at each pixel in the image. The early methods used for texture discrimination in the machine vision field are statistical methods. Many of these methods were proposed based on Julesz's pioneering work [151][152], in which he found that the human visual system uses statistical properties for texture discrimination. These include first and second order spatial statistics and higher order statistics. These properties manifest the distribution and interrelationship of grey values which have different effectiveness in discriminating texture within the human visual system. Julesz found that if second-order

spatial statistics of two textures are identical, these two textures are not discriminated spontaneously. The co-occurrence matrix is the best known second order statistical texture analysis technique. Its corresponding conception is introduced in subsection 3.2.2. The histogram statistics are normally used to detect first-order texture features; these are further described in subsection 3.2.1. Some other statistical methods such as autocorrelation and local binary patterns have also been applied in texture analysis.

3.1.2 Structural methods, Textons

Structural methods represent texture as consisting of many texture primitives and a corresponding spatial arrangement of these primitives. It's important to determine the form of the texture primitives. Commonly, these texture primitives can be individual pixels, average element intensity, or geometric segments etc. [144][147]. The primary goal of extracting primitives is to find fundamental micro-structures in images. Numerous structural texture analysis methods have been proposed. For instance, Chen et al. [156] proposed a grey-scale morphological granulometry algorithm for structural texture analysis. An iterative morphological decomposition algorithm was proposed by Wang et al. [157] to decompose an image into a set of morphological base functions. Their work was further extended by Lam and Li [158]. In [159], the structures are captured from natural images using a sparse coding concept, which simulates the coding strategy within the visual cortex of primates. The dominant representative research branch for extracting texture primitives from images is derived from texton theory. Julesz [3] introduced the term texton for the first time to explain the pre-attentive discrimination of texture pairs. He described textons as the line segments, elongated blobs, crosses and terminators which can be utilized in texture discrimination. Terminators include the corners and the endpoints of lines. He conjectured that pre-attentive discrimination of textures having identical second-order statistics but are made up by different textons can be perceived by the human visual system. For instance, Figure 3.1(a) and (b) illustrate two texture patterns which are made up by two pairs of basic units illustrated at the bottom in Figure 3.1 (a) and (b) respectively, where both textures have identical second-order statistics. In the left pattern (a), the numbers of terminators (say, endpoints of lines and line segments) of the two basic units are the same. Therefore this pair of units cannot be distinguished pre-attentively. In contrast, the second pair of units (b) can be discriminated pre-attentively, since although they have the same line segments (both are

three), the number of terminators are different. In this instance the triangle has three terminators, but the other one has four terminators.

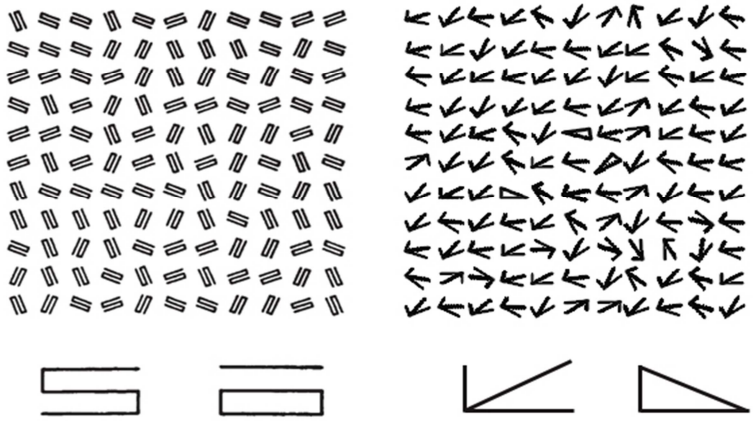

(a) (b)

Figure 3.1 Two texture patterns with identical second-order statistics. Left pattern (a) is composed of a pair of units which have the same textons (terminators) and right pattern (b) is composed of a pair of units which have different number of terminators.

Although Julesz proposed the theory of textons, the term “textons” remains a vague concept [153], as Julesz did not provide an operational definition or mathematical model. Malik and Leung et al. [154][155] extended the term texton and proposed an operational definition that a texture can be characterized by its responses to a filter bank (F_1,F_2,…,F_n).

$$\mathrm{R} = \{F_1 * I(\mathrm{x},\mathrm{y}), F_2 * I(\mathrm{x},\mathrm{y}), \ldots, F_n * I(\mathrm{x},\mathrm{y})\} \qquad (3.1)$$

If the filter bank is convolved with an input image I at each pixel (equation 3.1), it is reasonable to believe that some specific structures (e.g. lines, blobs) may produce positive responses (depending on the design of the filter bank). And if those structures appear repeatedly in the image, the feature vectors in the set R must be clustered into corresponding groups. Accordingly, filter responses that are clustered into a set of prototype response vectors are defined as textons by Malik and Leung et al. This novel definition enables textons to be generated automatically from an image.

Filter based feature extraction approaches are a direct way to extract features which can be used to generate textons. This approach is derived from signal processing techniques, in which pixel sequences in an image is processed as a specific signal sequence. A general framework of these methods is that a set of filters is applied on an image to generate filter

responses (equation 3.1) and certain features of those responses are then extracted for classification or segmentation purposes. The methods are divided into three subcategories: spatial domain, frequency domain and joint spatial/frequency domain. We describe the spatial domain filters first in subsection 3.2.4. Details of techniques relating to frequency and joint spatial/frequency domain filters are described in the subsection 3.2.5.

3.1.3 Model based methods

In model based texture analysis methods, a texture image is modelled as a parametric probability model or as a combination of a set of functions which represents known structural information and a random noise sequence. The textures can be characterized by the parameters of the model. Model based methods have been used for texture segmentation, classification and synthesis. Methods representative of the current state-of-the-art in the field of texture segmentation research include fractal models [163][164][165], autoregressive models [160][161][162], and Markov random fields [166][167][168][169]. Fractal geometry was firstly introduced by Mandelbrot [163] and the term fractals describe the geometric primitives which are self-similar and irregular. The fractal dimension is an important feature of fractals, as it provides a measure of the roughness of a surface. Pentland [164] has proved that there is a strong correlation between the fractal dimension and human perception of surface roughness. In practice, many efforts have been made to determine the fractal dimension to model the texture that can be used in various image processing applications [165]. In the autoregressive model, the texture is characterized by spatial interactions among image pixels, where pixel intensity is represented as a weighted sum of neighbouring pixels. The Markov random field (MRF) is a powerful stochastic tool to model the joint probability distribution of the image pixels in terms of local spatial interaction. It is a probabilistic process, in which it encodes spatial contextual constraints into the prior probability [167]. These models have been employed widely for image segmentation [166] [168] and texture classification [169]. Further fundamental concepts relating to MRFs are described in section 3.2.3.

3.2 Texture feature extraction and description

Feature extraction is the essential stage of texture based segmentation and classification. The primary goal of texture feature extraction is to express the differences in spatial structures by

differences in pixel intensities, so that homogeneous regions can be extracted based on such a feature space [141]. In a sense， the taxonomy of texture analysis methods relies on categorizing the feature extraction techniques. Due to the large number of activities that can be undertaken to extract useful textures, it is not practical to consider all proposed texture features. This section concentrates on those feature extraction techniques that have been widely used in image segmentation and have potential extension to be developed for medical image segmentations. The brief descriptions of those texture feature extraction techniques are provided in following subsections.

3.2.1 First order statistic based feature

First order statistics represent an early method and still an active one for texture feature extraction. They are low cost approaches that are invariant to rotation, as they are applied on sets of pixel values and are not involved in interrelationships among neighbouring pixels. Commonly, the texture features are characterized by first order histograms of intensity that provides a simple summary of statistical information of an image. Let a function *I(x,y)* of two space variables $x \in$ [1,2,…,N] and $y \in$ [1,2,…,M] represent an image, the *i* represents the grey levels. The first order histogram $H(i)$ is defined as:

$$H(i) = \frac{\sum_{x=1}^{N} \sum_{y=1}^{M} I_i(x,y)}{M \times N} \; i \epsilon (0, \dots, G-1) \qquad (3.2)$$

where G is the total number of grey levels in an image. The most commonly used central moments such as mean, variance, skewness and kurtosis which are derived from the histogram can be used to characterize the image features, as defined by Equations (3.3)-(3.6).

$$\text{Mean: } \mu = \sum_{i=0}^{G-1} iH(i) \qquad (3.3)$$

$$\text{Variance: } \sigma = \sqrt{\sum_{i=0}^{G-1} (i-\mu)^2 H(i)} \qquad (3.4)$$

$$\text{Skewness: } \mu_3 = \frac{\sum_{i=0}^{G-1} (i-\mu)^3 H(i)}{\sigma^3} \qquad (3.5)$$

$$\text{Kurtosis: } \mu_4 = \frac{\sum_{i=0}^{G-1} (i-\mu)^4 H(i)}{\sigma^4} - 3 \qquad (3.6)$$

The mean describes the average intensity of the texture whereas the variance measures the variation of grey level from the mean. The skewness represents the degree of asymmetry around the mean, and the kurtosis is a measure of histogram flatness. Features based on first order histogram statistics cannot provide any information about the spatial variation of the various grey levels within the image, but combined with some features based on second order statistics these measures can provide a useful tool for texture feature extraction. Recently, Aggarwal and Agrawal [170] used features based on first- and second-order statistics for classification of MRI brain images, and report results from comparative experiments that verify that the performance with such features outperforms existing methods based on wavelet transformation.

3.2.2 Co-occurrence matrix (GLCM)

The grey level co-occurrence matrix (GLCM) [171] is a well-known texture analysis method. The matrix is derived from an original image *I*, in which second order statistics are measured, stored and presented as a joint distribution of the grey levels of two pixels. The dependency of two pixels is described as a function of two parameters: distance of pixels *d*, and its relative orientation θ. Assuming an image is a function *I* with total number (G) of grey levels, the co-occurrence matrix is a G×G matrix, in which the entries are counts of the appearance of pixel pairs with grey level value *i* and *j* in a window separated by the distance *d* at orientation θ. The matrix can be expressed as $H_{(d,\theta)}(i,j)$. Figure 3.2 illustrates the GLCM calculation with distance *d*=1 and $\theta = \{0^o, 45^o, 90^o, 135^o\}$, where (a) is an 4×4 image example with grey levels {0,1,2,3}, (b) is the construction of GLCM, (c)(d)(e)(f) are the different forms of GLCM which are generated on four orientations. The texture features such as energy, contrast, homogeneity, correlation and entropy can then be extracted from these matrices [171]. The energy is also known as the angular second moment. It measures the smoothness of the texture surface hence larger values of energy indicate the region is smoother. The term energy is given by:

$$\text{Energy: } E(d,\theta) = \sum_{i=0}^{G-1}\sum_{j=0}^{G-1} H_{(d,\theta)}(i,j)^2 \qquad (3.7)$$

The contrast feature is expressed in equation 3.8, which is a measure of local variations present in an image.

$$\text{Contrast: } C(d,\theta) = \sum_{i=0}^{G-1}\sum_{j=0}^{G-1} |i-j|^2 H_{(d,\theta)}(i,j) \qquad (3.8)$$

Homogeneity is a measure of image local homogeneity, the contrast and homogeneity are inversely correlated. It is also called inverse difference and given by

$$\text{Homogeneity}=\sum_{i=0}^{G-1}\sum_{j=0}^{G-1}\frac{H_{(d,\theta)}(i,j)}{1+|i-j|^2} \quad (3.9)$$

Correlation is the measure of grey level linear correlation in two directions.

$$\text{Correlation}=\sum_{i=0}^{G-1}\sum_{j=0}^{G-1}\frac{(i-\mu_x)(j-\mu_y)H_{(d,\theta)}(i,j)}{\sigma_x\sigma_y} \quad (3.10)$$

Entropy is a measure of disorder of an image and is given by

$$\text{Entropy}=-\sum_{i=0}^{G-1}\sum_{j=0}^{G-1}H_{(d,\theta)}(i,j)\log_2 H_{(d,\theta)}(i,j) \quad (3.11)$$

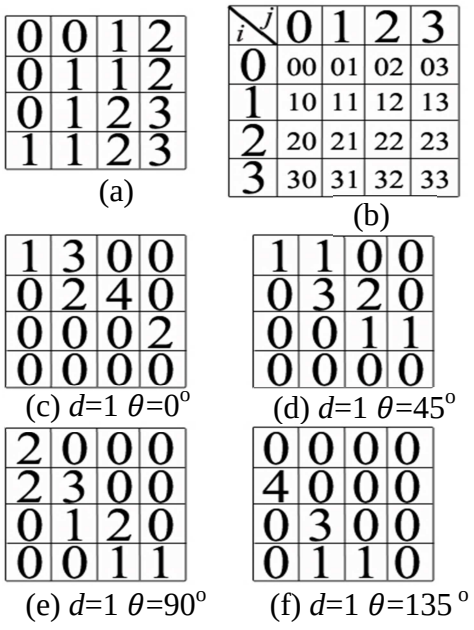

Figure 3.2 GLCM calculation with matrix function parameters d=1, $\boldsymbol{\theta}$ = {0°, 45°, 90°, 135°}. (a) is an 4x4 image example with grey levels {0,1,2,3}; (b) is the construction of GLCM; (c)(d)(e)(f) are the different forms of GLCM which are generated on four orientations.

Combinations of all the above features can be employed as a useful tool for texture discrimination and image segmentation. In [172], the GLCM is applied to estimate an appropriate level which may qualify the sub-regions of a natural image which will subsequently be further segmented. Marrón [173] presents a comparative study of two texture

operators (GLCM and fractal dimension) for image segmentation on various image forms. He noticed that the GLCM based features entropy can provide a better definition of edges and it outperforms many edge detectors. However, its computational cost is too expensive.

3.2.3 Markov random fields (MRF)

Markov random field (MRF) theory is a branch of probability theory, which can be used to capture contextual information in an image. In practice, such information (e.g. contextual constrains) are normally expressed as a joint probability based on local spatial interaction. The MRF models assume that the intensity of each pixel depend on the intensities of its neighbouring pixels. These local neighbourhood statistics are captured and represented by MRF models [167]. Assuming a 2D image with size $N \times N$ is a rectangular lattice, it can be denoted by

$$I = \{(x, y) | 1 \leq x, y \leq N\} \qquad (3.12)$$

For the lattice, pixel (x, y) can be simply re-indexed by a number i, where $i=(x-1)N+j$ and $i \leq N \times N$. Let F_i be a random variable which may represent the intensity at pixel (x, y). Accordingly, a set of all random variables defined on the set I can be denoted by

$$F = \{F_1, F_2, \ldots, F_{N \times N}\} \qquad (3.13)$$

where each F_i takes a value f_i in set L which is a set of labels. The label set L is specified as being continuous or discrete in different applications. A labelling of the sites in I can be defined by

$$f = \{f_1, f_2, \ldots, f_{N \times N}\} \qquad (3.14)$$

For example, as a discrete set, L may be represented by the set of quantized values of intensities, like {0, 1, 2…255}, for an image with 256 grey levels.

The interrelationships of sites in I can be defined by a neighbourhood system which is given by

$$N = \{N_i | \forall i \in I\} \qquad (3.15)$$

where N_i is the neighbour set of a site i. In the first order neighbourhood system, the site i has four connected neighbours. In the second order neighbourhood system, there are eight

neighbours surround site *i*. Within *N*, a series of subsets of sites called cliques in *I* are extracted. The form of cliques can be a single site, pair sites, triple sites and quadruple sites depending on the different neighbourhood systems utilised. The random field *F* can be defined as a MRF, if the probability mass function of *F* satisfies two conditions: one is that the function is positive and the other is that the function should satisfy Markovianity [167]. A MRF can be specified in two ways, either using conditional probabilities or joint probability. The theorem of MRF and Gibbs distribution equivalence [174] provides a means of specifying the joint probability of a MRF, so that not only the local information can be modelled in terms of conditional probabilities, but also the global texture can be measured by the joint probability.

A discrete Gibbs random field (GRF) which assigns a probability mass function over the entire lattice with respect to *N* is given by following form:

$$\mathrm{p}(F|f, f \in L) = Z^{-1}e^{-U(f)} \tag{3.16}$$

where

$$\mathrm{Z} = \sum_{f \epsilon L} e^{-U(f)} \tag{3.17}$$

The parameter Z is a normalizing constant called the partition function which is a sum over all possible labellings in L. The energy function $U(f)$is a sum of potential functions $V_c(f)$ over all possible cliques C.

$$\mathrm{U}(f) = \sum_{c \epsilon C} V_c(f) \tag{3.18}$$

MRF-based approaches have been successfully employed for many image processing applications which include image restoration and segmentation, edge detection, and texture analysis etc.. The MRF based image segmentation approach is based on a view of a random field segmentation result as a distribution of labels in the same lattice as the original image [166]. Kato and Pong [168] proposed a Markov random field (MRF) image segmentation model, which aims to combine colour and texture features. The remarkable contribution of their research is that it takes both colour and texture features into account in the segmentation of colour images. Deng and Clausi[166] proposed a simple Markov random field model with a new implementation scheme for unsupervised image segmentation based on image features. The proposed algorithm addresses the issue that traditional MRF segmentation models need

training data to estimate the model parameters. Varma and Zisserman developed a MRF classifier [169] for texture classification based on their previous method using filter bank in [204]. The MRF model is used to represent a probability density function (PDF) of the central pixels conditioned on their local neighbourhoods. At the filtering stage, instead of using filter responses at a pixel, the raw intensities of pixels in a neighbourhood square (of size $N \times N$) around that pixel are recorded to form a row vector with dimension N^2. They demonstrate that in feature extraction processes for certain tasks (e.g. classification), filter banks are not necessary but are sufficient [169]. Although the raw information (intensity values) from the texture pattern can be used to construct MRF models, the major disadvantage of using the MRF to represent a texture is the quadratic increase in the dimension of the feature space with the scale of the neighbourhood. The number of dimensions of the feature space is completely relied on the size (N) of the selected neighbourhood window. These high dimensional (N^2) features (vectors) may increase the computational cost when implementing the further computing processes (e.g. clustering, classification and synthesis etc.). Additionally, because of using raw intensities of pixels from source image, the MRF representation may be sensitive to the noise in the image.

3.2.4 Spatial domain filter bank (MR8, LM, Berkley)

Spatial domain filters are the straight forward way to characterize textures. One of the earlier attempts to discriminate between textures is by measuring the edge density using various edge detectors such as Sobel, Canny, Robert, Laplacian of Gaussian and Laws filters. Later on, multiple categories of filter kernels at different scales are combined into a filer bank which can be used to extract more sophisticated features for texture discrimination. In this case each filter kernel can be considered as a model of cells in the receptive fields of the visual cortex. This scheme was motivated by psychophysical research finding of models of processing in the early visual stages of primates [177][178]. Leung and Malik [154][155] proposed a filter bank called LM which is used to classify natural texture patterns taken from Columbia-Utrecht (CURet) texture database. This work was extended by Varma and Zisserman [139][169], who proposed the Maximum Response filter bank named MR8. Similar work by Martin et al. [175] introduced a small set of filters denoted as Berkeley Martin to detect boundaries in natural images.

- **LM filter bank**

In the LM filter bank, there are a total of 48 filters (Figure 3.3), comprising 18 even-symmetric filters (Figure 3.3-a), which are second derivative of Gaussian on 6 orientations at 3 scales and 18 odd-symmetric filters (Figure 3.3-b), which are derived from applying the Hilbert transform on those Gaussian derivatives. This makes total of 36 elongated filters. 8 filters (Figure 3.3-c) are centre-surround difference of Gaussian (DoG) and 4 filters (Figure 3.3-d) are Gaussian filters, these 12 filters are radially symmetric ones.

If an image is convolved with this filter bank, each pixel is transformed into a 48 dimensional vector, and it is reasonable to believe that most of the linear features can be extracted to characterize the texture, as elongated filters are typically bar or edge detectors.

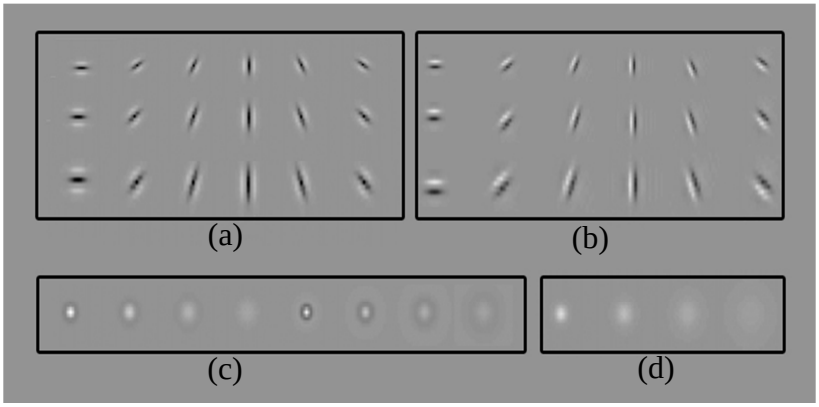

Figure 3.3 The LM filter bank with 48 filter kernels, which composes of (a) 18 even-symmetric filters, (b) 18 odd-symmetric filters, (c) 8 DoG filters and (d) 4 Gaussian filters

- **MR8 filter bank**

In the MR8 filter bank, a similar set of Gaussian derivatives are employed. It consists of 38 filters, instead of using the Hilbert transform of the second derivative Gaussian, they used the first derivative Gaussian giving an odd-symmetric filter (see Figure 3.4-a) for edge detection, whilst used the second derivative Gaussian as an even-symmetric filter (see Figure 3.4-b) for bar detection. As in the case of LM, both these filters are oriented, rotated on 6 orientations and employed at 3 scales. Additionally, two radially symmetric filters: Laplacian of Gaussian (LoG) and low-pass Gaussian are added to the set (see Figure 3.4-c). It should be noted that a difference of Gaussian (DoG) can be

approximated by a LoG. The filter responses of anisotropic first and second derivative Gaussian filters are generated by sampling the maximum filter responses in 6 orientations at each scale while the responses of isotropic filters (Gaussian and LoG) are used directly. This not only achieves rotation invariance, but also reduces the computational costs in the subsequent feature clustering stage, as it reduces the size of the dimensional space from 38 to 8 (6 maximum responses of elongated filters and 2 responses of radially symmetric filters).

A comparative study in [176] also demonstrates that MR8 provides better performance for texture feature extraction than the LM filter bank and the Schmid filter bank [182] which will be introduced in subsection 3.2.5.

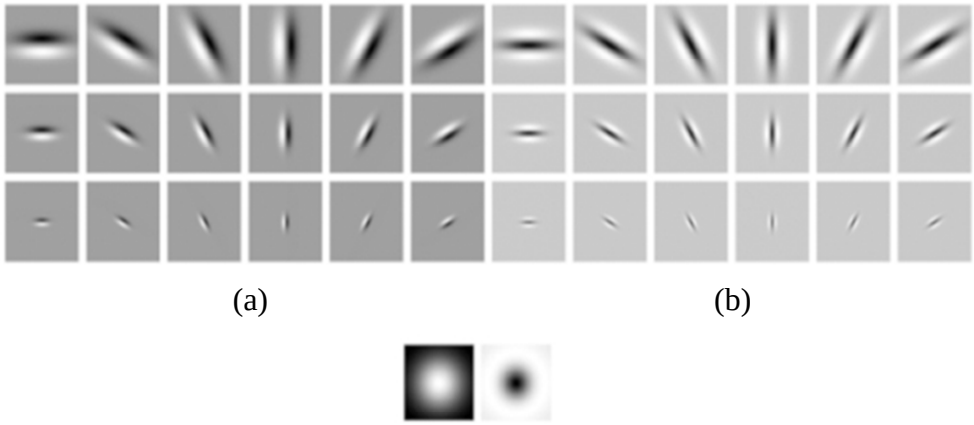

Figure 3.4 MR8 filter bank with 38 filter kernels, which composes of (a) 18 odd-symmetric filters, (b) 18 even-symmetric filters, (c) LoG filter and Gaussian filter

- **Berkley Martin**

A filter bank known as Berkley Martin [175] was designed and used to detect boundaries of different objects in natural images taken from the Berkeley segmentation dataset. Changes in brightness, colour and texture associated with natural boundaries were combined to characterize the objects' features. The filter bank consists of six pairs of elongated, oriented filters and an additional centre-surround filter. The elongated filters are divided into two classes: even-symmetric filters and the odd-symmetric filters, derived from a second derivative Gaussian and its Hilbert transform, respectively. These

filters are rotated on 6 orientations but at only one scale. Therefore if an image is convolved with the filter bank, each pixel is represented as a vector of 13 dimensional space.

Figure 3.5 Berkley Martin filter bank with 13 filter kernels

It is notable that the filter set only contains filters at a single scale. This may compromise the approach and result in an inability in detecting rich features from objects of interest. However, for the purpose detecting boundaries, one scale is supposed to be enough, especially given consideration of computational costs.

3.2.5 Joint spatial/frequency domain filters

Psychophysical studies have indicated that the human visual system processes images by analyzing their frequency and orientation components [179]. The Fourier transform is able to perform global frequency analysis of image textures. However, it lacks analysis in the spatial domain. Indeed, the spatial information is significant in many applications. The classical way to handle this is by introducing spatial dependency into Fourier analysis through the Windowed Fourier Transform (WFT) which can be defined as

$$\mathrm{F}_w(\omega, \varepsilon) = \int_{-\infty}^{\infty} f(x) W(x-\varepsilon)\, e^{-i\omega x}\, dx \qquad (3.19)$$

Here the function $f(x)$ is a one dimensional signal and $W(x)$ is the so called window function which allows us to see how the spectrum changes in the spatial domain. If the window function is Gaussian, the WFT becomes a Gabor transform.

Dennis Gabor [180] introduced the Gabor filter for the first time and for a one dimensional function it is defined as:

$$\mathrm{G}(x) = \mathrm{G}_{re}(x) + i\mathrm{G}_{im}(x) = \frac{1}{\sqrt{2\pi}\sigma} e^{-\frac{x^2}{2\sigma^2}} e^{i2\pi fx} \qquad (3.20)$$

Where $\frac{1}{\sqrt{2\pi}\sigma} e^{-\frac{x^2}{2\sigma^2}}$ represents a Gaussian envelope, f is the centre frequency and $e^{i2\pi fx}$ is a complex sinusoid which consists of real component $G_{re}(x)$ and imaginary component $\mathrm{G}_{im}(x)$. The real part also can be denoted as:

$$\mathrm{G}_{re}(x) = \frac{1}{\sqrt{2\pi}\sigma} e^{-\frac{x^2}{2\sigma^2}} \cos(2\pi fx) \qquad (3.21)$$

the imaginary part is defined as

$$\mathrm{G}_{im}(x) = \frac{1}{\sqrt{2\pi}\sigma} e^{-\frac{x^2}{2\sigma^2}} \sin(2\pi fx) \qquad (3.22)$$

Daugaman [181] extended the concept to two dimensions and adopted it for modeling of the receptive field of simple cells in the visual cortex of some mammals. The two dimensional Gabor function can be defined as

$$\mathrm{G}(x, y) = e^{-\frac{1}{2}(\frac{x^2}{\sigma_x} + \frac{y^2}{\sigma_y})} \cos(2\pi fx + \varphi) \qquad (3.23)$$

where σ_x and σ_y determine the spread of the Gaussian envelop and φ is the phase of the sinusoidal wave. When φ equals $\frac{\pi}{2}$ or -$\frac{\pi}{2}$, the equation turns into an odd-symmetric function. In practice, only the real part of the Gabor filter is convolved with the image region that coincides with the Gaussian envelope. Since the Gabor filter analyses the image in both spatial and frequency domains, different texture features can be extracted depending on the values of various parameters. The approach has been widely used in many applications of image processing, such as object recognition, texture segmentation and classification.

The wavelet transform has similar properties to the Gabor transform, which has also been widely used for texture feature extraction and classification. The usage of wavelet transform within texture analysis was introduced by Mallat in [205], where the textural features are extracted by using three wavelets at dyadic scales. Unlike the Gabor transform, the spatial resolution of wavelet transform is adopted to its frequency content [144]. Wavelet transform can thus be regarded as image decomposition in a set of spatially oriented frequency channels [142]. Recently, the wavelet transform has been attracted much interest in many applications of texture analysis [206] [207] [208] [209] [210].

Schmid [182] proposed a filter bank for feature extraction, which consists of 13 isotropic "Gabor-like" filters. The filters combine the frequency and spatial scales by introducing two variables (τ and σ) in a function, which is defined as

$$F(x, y, \tau, \sigma) = F_0(\tau, \sigma) + \cos\left(\frac{\sqrt{x^2+y^2}\pi\tau}{\sigma}\right) e^{-\frac{x^2+y^2}{2\sigma^2}} \quad (3.24)$$

where $F_0(\tau, \sigma)$ is added to obtain a zero DC component. In their experiments, rotationally invariant filters are used with only 5 scales (σ=2, 4, 6, 8, 10) and 4 frequencies (τ=1, 2, 3, 4), in which for a small scale only small τ are used to avoid generating a high dimensional vector. Figure 3.6 illustrated 13 rotationally invariant filter kernels which are grouped by corresponding rows (τ) and column (σ).

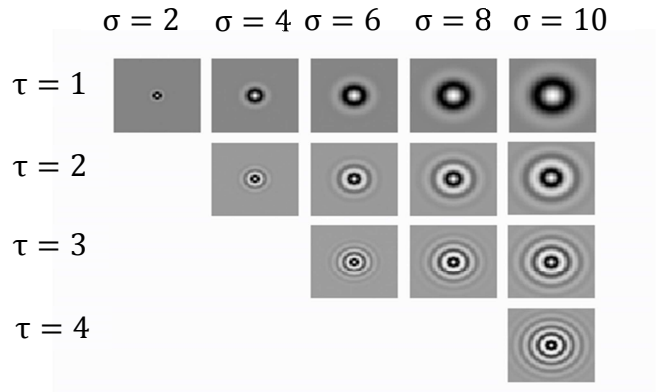

Figure 3.6 Schmid filter bank with 13 filter kernels

3.3 Local invariant texture feature descriptor

In practice, texture features can be extracted at various scales where for each scale, some particular local features can be detected which are quite important for texture segmentation (object recognition). For instance, a tree consists of leaves, branches, and a trunk. If features are required to be extracted at the leaf level, only this corresponding scale need to be selected and applied. As we zoom out, if the required features are at whole tree level, the scale has to change. Structural texture analysis methods determine those scales by the sizes of the filter kernel in the filter bank and these, in turn are chosen to respond to the different sizes of structures. Moreover, many texture features are derived from the original grey levels in an image. However, those algorithms may be sensitive to any changes of grey level among different image modalities. In this case, grey-level invariant features are significant in

handling those problems. We introduce two techniques called the Local Binary Pattern (LBP) and the Scale Invariant Feature Transform (SIFT) in the following subsections.

3.3.1 Local Binary Pattern (LBP)

Local Binary Pattern (LBP) texture analysis is a method that uses grey-scale invariant texture statistics, derived from detecting grey level intensity differences in a local neighbourhood. The LBP operator was first introduced as a complementary measure for local image contrast by Ojala [183], and although a number of extensions [184] [185] [187] for LBP have been developed, the basis of LBP is similar. A binary number at each pixel is calculated by thresholding between the centre pixel and its neighbouring pixels. The classic version of the LBP considers only eight neighbour pixels of the centre pixel, and then all circular neighbourhoods are considered. A procedure for LBP computation is illustrated in Figure 3.7, using a simple image of 3×3 size. The corresponding grey level values of each pixel are presented in Figure 3.7 (a). The grey level differences between the centre pixel and neighbouring pixels are illustrated in Figure 3.7 (b). If the difference is larger or equal to 0, the neighbouring pixel is signed as value 1, otherwise, the value is 0. This gives 8 binary numbers surrounding the centre pixel, as shown in Figure 3.7 (c). The LBP code then can be calculated through multiplying those binary numbers (0 or 1) by powers of two and summing them. So, for the Figure 3.7 example, the LBP code is $0 \times 2^0 + 0 \times 2^1 + 0 \times 2^2 + 1 \times 2^3 + 1 \times 2^4 + 1 \times 2^5 + 1 \times 2^6 + 0 \times 2^7$ =120.

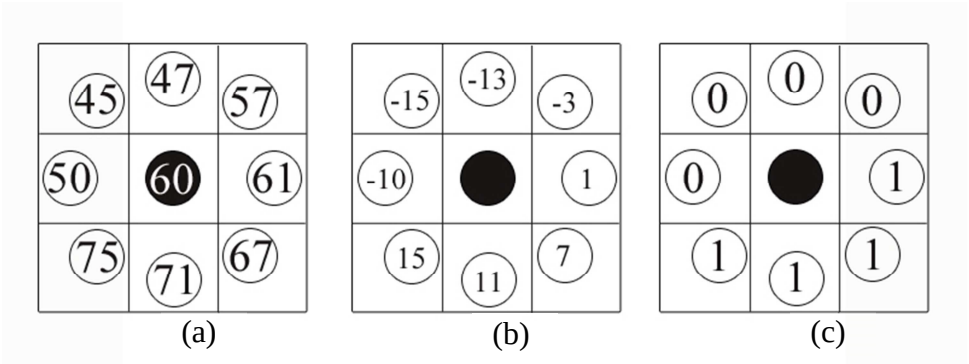

Figure 3.7 An example of LBP computation, (a) a simple image of 3×3 size with corresponding grey level values of each pixel, (b) illustrates the grey level differences between the centre pixel and neighbouring pixels, (c) illustrates 8 binary numbers surrounding the centre pixel

The LBP operator has been extended to use neighbourhoods with different sizes [184]. In this derivation of LBP, the LBP code is calculated for each pixel in any cropped portion of the image that allows any radius (denoted as R) and number of pixels (denoted as P) in the neighbourhood. The values of neighbours which do not locate exactly on pixels are estimated by bilinear interpolation. The LBP code then can be calculated by

$$LBP_{P,R}(x_c, y_c) = \sum_{p=0}^{P-1} s(g_p - g_c)2^p \qquad (3.24)$$

where $g_p - g_c$ is the difference of gray level values between the centre pixel and one of neighbouring pixels. Function *s(x)* is defined by

$$\mathrm{s(x)} = \begin{cases} 1 \; x \geq 0 \\ 0 \; x < 0 \end{cases} \qquad (3.25)$$

Finally, a feature vector can be represented by the distribution of these codes.

Another extension of the original LBP [185] generates rotation invariant LBPs called uniform patterns that make LBP codes invariant with respect to rotation of the image domain, and also reduce the dimensionality of the feature vector.

The LBP method can be regarded as a general tool for structural and statistical texture analysis, since the LBP code that labels each pixel can be interpreted as a micro-structure (include spots, flat areas, edges, curves, etc.), and the distribution of micro-structure can be seen as a statistical placement. Because of this advantage, the LBP has been applied and extended in texture classification, texture based segmentation, and texture synthesis. For instance, Connah and Finlayson [186] investigated the application of the LBP texture operator in the retrieval of coloured object under changes in illumination colour and object pose. In [187], Liao and Chung extended the LBP by introducing the concept of Advanced Local Binary Patterns (ALBP), and demonstrate that these are capable of representing most of the essential local structure characteristics of texture images obtained from CURenT database. He et al. [188] proposed a Bayesian LBP operator which is formulated using a novel Filtering, Labelling and Statistical (FLS) framework.

3.3.2 Scale invariant feature transform (SIFT)

The Scale Invariant Feature Transform (SIFT) was proposed by Lowe [202] to extract distinctive local image features that can be used in a various image processing applications, such as image matching, object recognition, object tracking etc. There are four stages to extracting SIFT features: The first stage calculates potential points that may be invariant to scale and orientation by detecting local minima and maxima based on responses of a set of difference of Gaussian (DoG) filters. The determination of so-called keypoint candidates (minima and maxima) is based on a scheme that compares each point with its 26 neighbouring pixels at the same and adjacent scales. Then the location and scale of each potential keypoint are determined in the second stage, in which all points with low contrast are discarded. The third stage assigns one or more orientations to each keypoint. The orientations are calculated based on local image gradients around keypoints. Figure 3.8 (a) illustrates the image gradient magnitudes and orientations in the region around the keypoints at the selected scale, where the circles indicate the Gaussian window covering the region. All gradients are generated from a 16x16 sample region, which are then accumulated into a descriptor. Finally, a keypoint descriptor is generated at each keypoint. It is formed as a vector which contains values of all the orientations and corresponding lengths, as shown in Figure 3.8 (b). The descriptor is represented as a 4×4 grid which summarizes those orientation histograms over 4×4 sub-regions, and each orientation histogram contains 8 direction bins. The sum of the gradient magnitudes near that direction is indicated by length of each arrow. It results in a feature vector containing 4x4x8=128 elements.

Features extracted from the image using SIFT are invariant to scale and orientation, and are highly distinctive of the image. SIFT has been used in some natural image processing applications. For instance, Suga and Fukuda et al. [189] proposed an object recognition and segmentation method on natural images using SIFT combined with graph cuts. SIFT is used to detect the potential candidate seeds for the graph cut algorithm. Sobek and Cetnarowicz et al.[190] applied the SIFT algorithm in fingerprint recognition. Two fingerprint images are matched by matching their descriptors. Kamencay and Breznan et al. extended the SIFT by proposing a SIFT-PCA algorithm for face recognition, in which the principle component analysis (PCA) is employed to analyse face data. The modified algorithm uses PCA instead of histograms to normalize gradient patches and this significantly reduces the vector dimensionality.

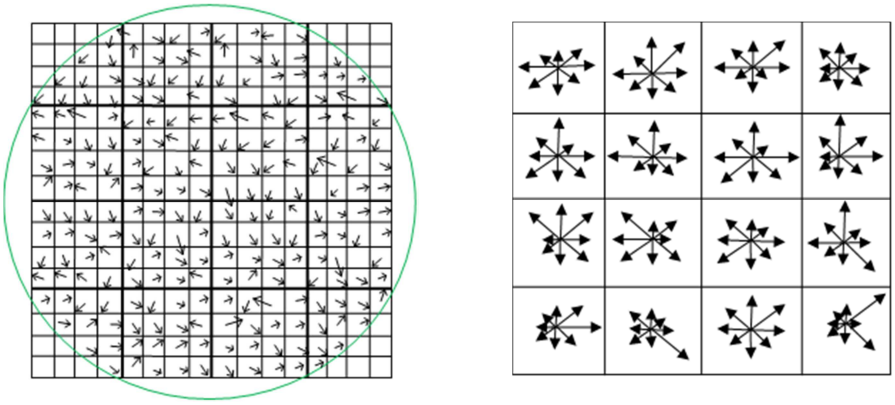

(a) (b)

Figure 3.8 SIFT descriptor computation, (a) illustrates the image gradient magnitudes and orientations in the region around the key point at the selected scale, the descriptor (b) is formed as a vector which contains values of the orientations and corresponding lengths.

3.4 Chapter conclusion and discussion

Image texture is one of the most important characteristics to distinguish various patterns which have different visual features in images. It has received extensive attention and has been used to perform image segmentation and shape detection. Texture based image segmentation has been adopted widely on problems involving natural image segmentation, where texture analysis is a critical stage. Texture analysis is a procedure for characterizing textures within the image that can achieve very successful image segmentation results. To facilitate an understanding of our work and set it in context, this chapter introduced various texture analysis methodologies which have been utilized in image segmentation. The methods are categorized into: statistical methods, structural methods and model based methods. Statistical methods represent textures as a statistical distribution of selected features which are computed at each pixel in images. In contrast, structural method, represented texture as consisting of many texture primitives grouped within a corresponding spatial arrangement. In model based texture analysis, a texture image is modelled as a parametric probability model or as a combination of a set of functions which represents the known structural information and random noise. Early attention in texture analysis has mainly focused on statistical methods such as the first- and second-order statistical analysis; later model-based methods such as Gaussian Markov random fields are introduced and more recently, local invariant features representing texture has become a focus of research.

In a sense，the taxonomy of texture analysis methods relies on a categorization of feature extraction techniques. We described those feature extraction techniques with respect to corresponding categories of texture analysis methods, particularly concentrating on those techniques that have potential extensions for medical image segmentations. The first order histogram is a low level feature for texture discrimination. Although it cannot reflect interrelationships among neighbouring pixels it can be used for image pre-processing within the segmentation pipeline (e.g. normalization, noise reduction etc.) and is especially attractive considering its low computational costs,. Feature extraction methods based on second order statistics such as GLCM use a joint distribution of the grey levels of two pixels. Model based methods such as MRF and LBP provide more sophisticated features which reflect interrelationships among neighbouring pixels. Different texture primitives which are able to characterize texture can be detected using MRF or LBP. It is reasonable to believe that MRF and LBP have more potential to achieve better image segmentation performance compared with GLCM. In practice, minimising the high computational cost caused by high dimensional feature vectors generated when using MRF or LBP may remain a research focus. In structural methods, filter based feature extraction approaches offer a direct way to extract features which can be used to generate textons. The structure can be decomposed into micro-structures (line, spot) using a filter bank which contains a set of filters. A comparative study in [176] demonstrates that the MR8 filter bank has better performance for extraction of texture features than either the LM filter bank or the Schmid filter bank [182].

Psychophysical studies have indicated that the human visual system process images by analyzing their frequency and orientation components [179]. This research finding motivates applications and developments of Gabor filters which analyse texture features in both the spatial and frequency domain. The primary limitation of filter based methods is that the extracted features are sensitive to choices of scale which determine the size of filter kernel. Detected feature structures are also determined by the chosen filter kernel shapes. Therefore, the selected filters have to be optimized in kernel size, shape and rotation according to consideration of specific properties of structures in images. It is not possible to design a unified filter bank to extract various types of features from images in different applications. This problem can be addressed using scale and orientation invariant feature extraction techniques such as SIFT that can be employed to extract specific invariant features.

Considering the lack of existing methods for retinal vessel segmentation using texton, we

would like to fill this gap and pursue more accurate segmentation by investigating filter based texture feature extraction techniques and textons. The following chapters describe how to design the filter bank for retinal vessel segmentation in fundus images, and show that better segmentation performance can be achieved using textons. We also examine the feasibility of using a general texton to implement retinal vessel segmentation on different datasets, the utilities of Gabor filters to reduce the dimensionality of feature vectors and the potential application of SIFT to improve texton generation.

CHAPTER 4

4. Retinal vessel segmentation on pathological fundus image

The importance of retinal vessel segmentation for diagnosis, screening and treatment of various ocular diseases has been emphasised in chapter 1 and 2. We also demonstrated the significance of automated retinal vessel segmentation methods for a computer assisted diagnostic system which is capable of automated detection and grading various forms of retinopathy. Many methods have been reviewed in chapter 2. Among them a representative category is the matched filter based segmentation method, in which the retinal vessel's features are extracted by convolving a retinal fundus image with multiple specific filter kernels. Conventionally, the matched filtering based method is combined with thresholding-based segmentation methods to obtain a final binary segmentation result. Many retinal vessel segmentation methods have been proposed based on classic matched filters (CMF) [85]. Most of them improved CMF by modifying or optimizing the filter kernel, while some methods combined CMF with other techniques to generate more accurate results. However, in many of these methods, the algorithms frequently fail in cases which contain some pathological changes. Those anomalies are particularly characterized by various forms of exudates (soft and hard drusens, cotton-wool spots, etc.) and manifest themselves as local small brightness blobs in a fundus image. These anomalies, especially when located around vessels, have the most important influences for segmentation. Besides, images are often contaminated by noise and suffer low contrast between the vessels and surrounding background that also challenges the vessel segmentation. Cases which suffer from existing damage due to disease can be particularly problematic and thus remain an open problem. Our initial work is focused in this area.

In this chapter, we describe an improved retinal vessel segmentation scheme that is capable of excluding influences caused by anomalies in fundus images. The chapter demonstrates how to use local texture energies to detect those anomalies like drusen and how to eliminate their influences for retinal vessel segmentation. Initially, such influences are

detailed in section 4.1 and a method we adopted for drusen detection is described in section 4.2. In section 4.3, the matched filter which is used to extract the vessel features and segmentation is detailed. Section 4.4 presents the experimental results and evaluation.

4.1 The influence of abnormalities on vessel segmentation

As we described in chapter 1, commonly, the hard or soft drusen can be found in retinal images of patients who suffer from AMD. The hard drusen manifests itself as a set of small yellowish-white blobs with a clear boundary, and the soft drusen has a similar appearance but with a fuzzy boundary. For those patients with early stage DR, the fat and protein that leaks from weak vessels may form yellow white blobs on the retina. These are known as so-called retinal exudates, appearing as brighter blobs than the background in retinal fundus images. For those patients who suffer from later stage DR, their retinal fundus images normally contain cotton-wool spots which appear as white patches that exhibit fluffy density and a fuzzy boundary.

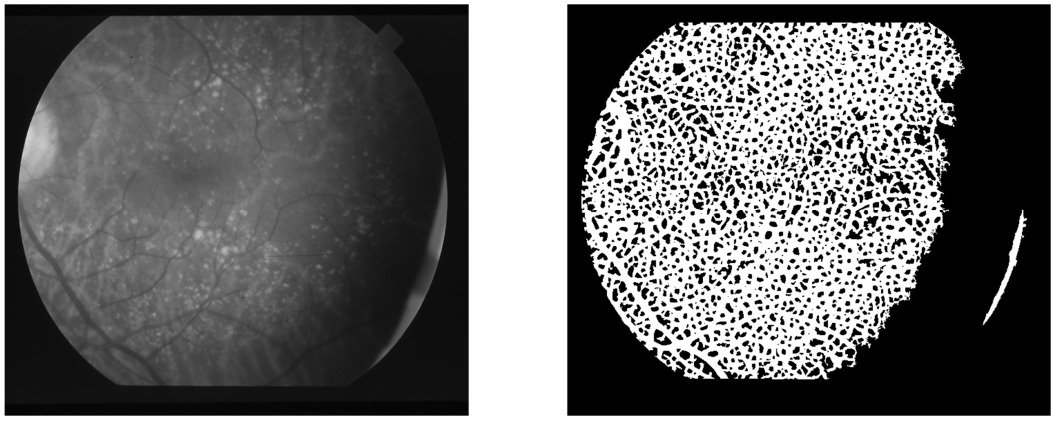

(a) (b)

Figure 4.1 The segmentation problem for fundus image contains pathological changes. (a) a grey level fundus image contains numerous drusens; (b) illustrates retinal vessel segmentation result using the matched filter based method proposed by Chanwimaluang [192]

The common characteristic of these anomalies presented in fundus images is that normally they are brighter than the background. These characteristics may result in the failure of vessel segmentation due to the dramatic gradient changes around the boundaries. This is especially problematic in cases where the anomalies are located around the vessels as the anomalies significantly influence the segmentation. Figure 4.1 illustrates an example where

the segmentation has been compromised by anomalies. Figure 4.1 (a) demonstrates a grey level fundus image which contains numerous drusens around vessels, and Figure 4.1 (b) illustrates the retinal vessel segmentation result using the matched filter based method proposed in [192]. We address this problem by removing the brightness blobs (that appear like drusen) before undertaking segmentation in order to reduce their effect on the vessel segmentation. The framework of our method is primarily composed of four stages: First, pre-processing to reduce noise and enhance the contrast; second, detecting and removing drusen; third, extracting vessel features using a matched filter to generate maximal filter responses; and fourth, converting the responses to binary by using a local entropy thresholding algorithm followed by using length filtering to remove the isolated objects.

4.2 Drusen detection using local energy

In our experiment, an original image is converted into a grey level image by isolating the green channel before we apply a texture-based drusen detection scheme on the image. We use the green channel since other authors (e.g. Wu et al. [91]) have noted that contrast between vessels and background is enhanced in this channel. The image is then smoothed by a two dimensional Gaussian filter. After the image pre-processing stage, we adopted a texture-based drusen detection method [193], in which the texture of the drusen is characterized in term of local energy. The local energy has been defined in [194] as the sum of squared responses of orthogonal pairs of Gabor or Log-Gabor filters. The Log-Gabor filter was proposed by Field [195], which is a logarithmic transformation of the Gabor function. A Gabor filter is a powerful tool to analyse texture in both the spatial and frequency domain. It has commonly adapted to calculate the local energy based on the multi-scales and multi-orientation features. Unlike the Gabor filter, the Log-Gabor filter has Gaussian transfer function when viewed on the logarithmic frequency scale, which allows the filters to be used in large bandwidths, from 1 to 3 octaves. This characteristic make the Log-Gabor filter to be a particularly useful tool for drusen detection or segmentation [193]. Due to the singularity in the Log-Gabor function at the origin, an analytical expression for the filter in spatial domain is absented. In the linear frequency domain, the Log-Gabor function is formed by

$$\mathrm{G}(f_0, \theta_0) = \mathrm{e}^{\left\{\frac{-[\log(f/f_0)]^2}{2[\log(\sigma_f/f_0)]^2}\right\}} \times e^{\left\{\frac{-[\theta-\theta_0]^2}{2\sigma_\theta{}^2}\right\}} \qquad (4.1)$$

where the former part of the formula is a radial component and the latter part is an angular component. Parameters (f, θ) represent a set of polar coordinates, f_0 indicates the central radial frequency and the θ_0 is the filter direction. σ_f and σ_θ define the radial bandwidth and angular bandwidths, respectively. The term σ_f / f_0 in equation 4.1 has to be held constant for varying $f_0$to obtain constant shape ratio filters. In order to design the filter to have bandwidth of 2 octaves, the term σ_f / f_0 is empirically chosen as 0.65. The Log-Gabor filter was applied at 2 scales (f_0=1/3 and f_0=1/6). Because the exudate contained in a retinal image may presented as an arbitrary blob (e.g. a spot, an elongated ellipse etc.), filters are applied at different orientations. In our experiment, the values of orientation parameter θ_0: 0^o, 30^o, 60^o, 90^o, 150^o were chosen as same as in [193]. The local energy at each pixel is calculated by summing squares of even and odd symmetric Log-Gabor filter responses at every pixel. It is obtained as

$$E_{\theta_0}^{f_0}(x, y) = (R_{\theta_0}^{f_0, even}(x, y))^2 + (R_{\theta_0}^{f_0, odd}(x, y))^2 \qquad (4.2)$$

where $(R_{\theta_0}^{f_0, even}(x, y))$ and $(R_{\theta_0}^{f_0, odd}(x, y))$ present the responses of even and odd symmetric Log-Gabor filters, respectively. Figure 4.2 illustrates an example of exudate detections using local energy, in which (a) is the pre-processed grey level image, and (b) demonstrates exudates contained in (a).

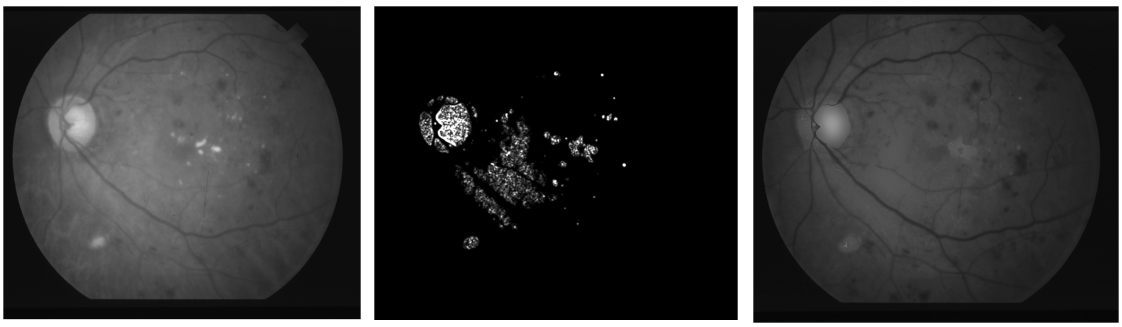

(a) (b) (c)

Figure 4.2 Local energy example of detecting exudate. (a) is the pre-processed grey level image, and (b) demonstrates exudates contained in (a); (c) is the result image where the exudates are removed.

Once drusen are detected they are removed by an averaging filter applied to the areas identified by the local energy map. Each pixel value in the areas of detected exudates is replaced by the average value of its neighbourhood. In practice, the averaging filter also is

based on a kernel, and can be seen as a convolution filter. The kernel determines the size of the neighbourhood. In our experiment, considering the large size of a fundus image (e.g. size of 565×584 pixels in the DRIVE dataset and 700×605 pixels in the STARE dataset), we choose a filter size of 40×40. And before apply the filter on the objective areas of image (the drusen areas), we transform the local energy map to a binary image which is used to determine the range of averaging area. In our experiment, these areas, actually, are drusen. The threshold is simply chosen by calculating the average value of the energy map. An example of final result image is demonstrated in Figure 4.2 (c).

4.3 Retinal vessel segmentation using Matched filter

4.3.1 Matched filter

The design of the matched filter is based upon a spatial profile of a vessel that exhibits a cross-sectional intensity profile that can be approximated by a Gaussian shaped curve (Figure 4.3-b illustrates this property; Figure 4.3-a is a patch of original fundus image). The basis of using matched filter is constructing a Gaussian-shaped model which can be used to match the vessels for detection [85]. Therefore, the matched filter kernel can be expressed by

$$k(x,y) = -\mathrm{e}^{\left(\frac{-x^2}{2\sigma^2}\right)} \; \forall \; |y| \leq \frac{L}{2} \tag{4.3}$$

where L is the length of the vessel segment that has a fixed orientation. σ is the spread of the intensity profile. Because the vessels may rotate in any orientation, the kernel $k(x,y)$ has to be rotated as well. The kernel then can be transformed as

$$P_i = [u\ v] = k(x,y) \times \begin{bmatrix} \cos\theta_i & -\sin\theta_i \\ \sin\theta_i & \cos\theta_i \end{bmatrix} \tag{4.4}$$

$$K_i(x,y) = -\mathrm{e}^{\left(\frac{-u^2}{2\sigma^2}\right)} \; \forall P_i \in N \tag{4.5}$$

In which, the P_i denotes the points in a neighbourhood N defined in the area of $[u\ v]$. The i (i =1, 2, 3 … 12) indicates the index of kernel which has a predefined angle. To eliminate the long double sided tails of a Gaussian curve in N (in equation 4.5), the tails are truncated at $+3\sigma$ and -3σ, thus $|u| \leq 3\sigma$[85]. Meanwhile, $|v| \leq L/2$ is defined, in which L is used as

the neighbourhood length of the kernel. The matched filter is then normalized to have zero mean as follows:

$$K'_i(x,y) = K_i(x,y) - \frac{1}{n}\sum_{P_i \in N} K_i(x,y) \qquad (4.6)$$

In which the number of points in *N* is denoted as n.

In our experiment, we applied a set of 12 orientations (0°, 15°, 30°, 45°, 60°, 75°, 90°, 105°, 120°, 135°, 150°, 165°) of filter kernel at one scale (σ =1.75). The choice of the12 orientations is according to the statement in [87], where they introduced that a filter kernel rotating by an amount of 15^o is adequate to detect vessels with an acceptable amount of accuracy. The value of sigma was chosen empirically, since an empirical evaluation on training images showed that on average, the sigma=1.75 gave the visually maximum responses. The cross-sectional intensity profile of the kernel with orientations = 0° is illustrated in Figure 4.3 -c.

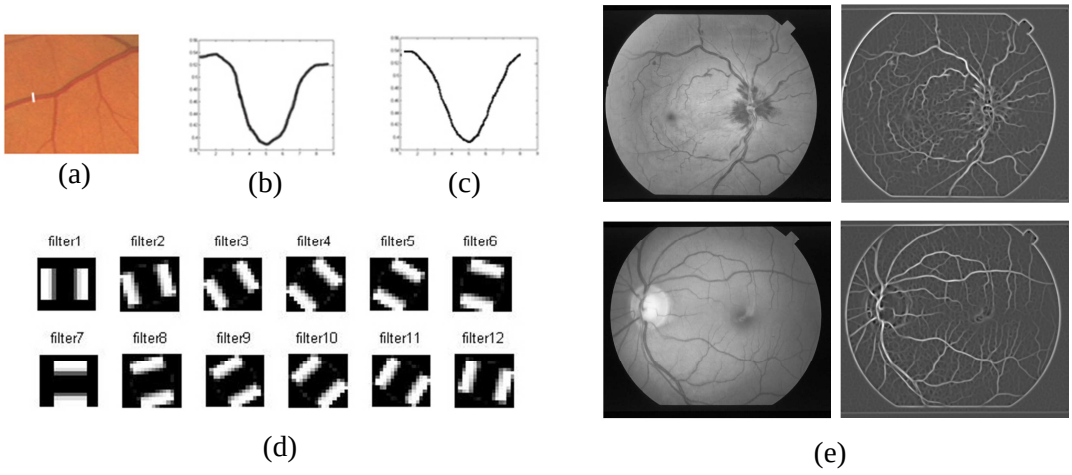

Figure 4.3 Vessel's cross-sectional intensity profile and matched filter kernels (d) and examples of filtering results. (a) is a patch of original fundus image; (b) is a cross-sectional intensity profile of a vessel; (c) is the cross-sectional intensity profile of the matched filter kernel with orientations = 0°; (e) show examples that result from the filtering using Match Filter, where the gray scale images are illustrated in left column of (e) and the right column illustrates the corresponding filter responses.

Given the vessel networks have a wide range of vessel widths (2-15 pixels), the size of each Gaussian kernel is chosen to be 16×15 pixels. Figure 4.3-d illustrated the filter kernel

with 12 different orientations. The vessel features then are extracted by taking the maximum filter responses at each pixel.

4.3.2 Segmentation method

The segmentation method is implemented based on matched filter responses using a thresholding scheme to find an optimal threshold value which can be used to distinguish between vessels and the background. The thresholding algorithm adopts local entropy based on the grey level co-occurrence matrix, in which distribution of the grey levels of two pixels are taken into account. This local entropy based thresholding technique was proposed by Pal and Pal [196] and has been employed by Chanwimaluang and Fan [192] for retinal vessel segmentation. Considering dependences of intensities between each image pixel and its effectiveness, we follow the same approach. The co-occurrence matrix was made by considering horizontal right and vertical lower transitions [196]. Namely the distance d of matrix $H_{(d,\theta)}(i,j)$ equals 1 and θ are 0^o and 270^o (see section 3.2.2 for details). Therefore, the probability of co-occurrence $p_{(i,j)}$ of grey levels i and j can be expressed as

$$p_{(i,j)} = \frac{H_{(1,0)}(i,j)+H_{(1,270)}(i,j)}{\sum_i \sum_j H_{(1,0)}(i,j)+\sum_i \sum_j H_{(1,270)}(i,j)} \qquad (4.7)$$

Let s be a threshold which is $0 \leq s \leq G-1$, in which the G is the total number of grey levels contained in an image. Therefore the image can be split into two parts, the object donated by A and the background donated by B. We get the following cell probabilities:

$$P_{ij}^A = \frac{p_{(i,j)}}{\sum_{i=0}^{s} \sum_{i=0}^{s} p_{(i,j)}} \quad 0 \leq i,j \leq s \qquad (4.8)$$

$$P_{ij}^B = \frac{p_{(i,j)}}{\sum_{i=s+1}^{G-1} \sum_{i=s+1}^{G-1} p_{(i,j)}} \quad s+1 \leq i,j \leq G-1 \qquad (4.9)$$

Then the second order entropies of the object and background can be defined as

$$E_A^{(2)}(s) = -\frac{1}{2} \sum_{i=0}^{s} \sum_{j=0}^{s} P_{ij}^A \log_2 P_{ij}^A \qquad (4.10)$$

$$E_B^{(2)}(s) = -\frac{1}{2} \sum_{i=s+1}^{G-1} \sum_{j=s+1}^{G-1} P_{ij}^B \log_2 P_{ij}^B \qquad (4.11)$$

The total second-order local entropy of the object and the background can be written as

$$E_T^{(2)}(s) = E_A^{(2)}(s) + E_B^{(2)}(s) \qquad (4.12)$$

The optimal threshold for object and background classification then can be obtained by finding the grey level corresponding to the maximum of $E_T^{(2)}(s)$ [196].

After implementing the thresholding algorithm, some pixels may be misclassified and may be presented as small isolated objects in the image. Therefore, length filtering which uses the concept of connected pixels labelling is adopted to remove those isolated objects.

4.4 Experimental results and evaluation

In our experiment, the parameters of the Log-Gabor filter for drusen detection described in subsection 4.2 and the parameters of the Matched Filter described in subsection 4.3.1 were obtained empirically based on the 20 images of training set in STARE. The test and evaluation procedure are applied to 20 STARE testing images using both the original method proposed by Chanwimaluang [192] and our improved method (that includes a pre-processing step to remove exudates). Figure 4.4 illustrates a comparison of segmentation performance, in which (a) is a pre-processed image named 'im044' in the STARE database, (b) is its ground truth, (c) is the segmentation result using Chanwimaluang method, and (d) is the segmentation result using our method. Visually, (a) contains exudates which influences the segmentation illustrated in (c). This abnormality has less influence (d) when applied to our method on an image that contains pathological changes. In order to evaluate the segmentation performance of our method, we use the standard measures sensitivity, specificity and accuracy (see section 2.1). The comparative results of sensitivity, specificity and accuracy are illustrated in table 4.1, of which the last row shows the average values of those terms. The column "1" denotes the results using our method and the "2" the results of Chanwimaluang's method. Paired t-tests on the specificity values for individual images of the STARE database show that our method (1) performs significantly better than the Chanwimanluang's method (2), with p-values= 1.1×10^{-2}, meanwhile, as expected, the test results also demonstrate that there is no significant difference on the sensitivity between our method and chanwimanluang's method. This, in turn, results in the better accuracy of our method. These results also reflect that our improved method is capable of excluding the drusen influences while maintains the good sensitivity of vessel segmentation. Additionally, the standard deviations of all measurements derived from our method are lower than the ones of

Chanwimanluang's method (see the bottom row of table 4.1 (.)), this also reflects the stability of our method.

Table 4-1 Comparative results on STARE data using our method and the method in [192].

Image	Sensitivity		Specificity		Accuracy		Az	
	1	2	**1**	2	**1**	2	**1**	2
Im0001	0.7009	0.6686	0.9509	0.9279	0.9310	0.9072	0.9081	0.8926
Im0002	0.7386	0.7258	0.9200	0.9001	0.9080	0.8885	0.9152	0.9065
Im0003	0.7692	0.7634	0.9016	0.8957	0.8937	0.8878	0.9136	0.9112
Im0004	0.5344	0.5747	0.9840	0.9809	0.9507	0.9508	0.9273	0.9181
Im0005	0.5825	0.6146	0.9729	0.9672	0.9377	0.9354	0.9323	0.9347
Im0044	0.6907	0.8614	0.9736	0.9112	0.9539	0.8204	0.9166	0.9406
Im0077	0.7669	0.8041	0.9637	0.9526	0.9479	0.9407	0.9314	0.9261
Im0081	0.8242	0.8646	0.9517	0.9382	0.9422	0.9327	0.9410	0.9346
Im0082	0.7267	0.7922	0.9766	0.9634	0.9569	0.9500	0.9331	0.9330
Im0139	0.7083	0.7654	0.9744	0.9465	0.9530	0.9320	0.9267	0.9275
Im0162	0.7171	0.7534	0.9721	0.9600	0.9539	0.9453	0.9492	0.9488
Im0163	0.7450	0.8128	0.9819	0.9669	0.9636	0.9549	0.9544	0.9519
Im0235	0.7959	0.8140	0.9495	0.9440	0.9358	0.9325	0.9239	0.9235
Im0236	0.6972	0.8392	0.9736	0.9310	0.9485	0.9227	0.9370	0.9366
Im0239	0.7374	0.6348	0.9703	0.9775	0.9502	0.9479	0.9245	0.9185
Im0240	0.6632	0.7391	0.9679	0.9577	0.9367	0.9354	0.9264	0.9187
Im0255	0.7207	0.8079	0.9743	0.9584	0.9516	0.9449	0.9478	0.9474
Im0291	0.7423	0.7726	0.9817	0.9769	0.9696	0.9666	0.9576	0.9518
Im0319	0.7478	0.5645	0.9644	0.9851	0.9550	0.9670	0.9160	0.9107
Im0324	0.8235	0.6318	0.9519	0.9756	0.9434	0.9527	0.9519	0.9363
Average	**0.7216**	**0.7402**	**0.9628**	**0.9508**	**0.9442**	**0.9308**	**0.9317**	**0.9285**
Std.	**(0.0699)**	**(0.0901)**	**(0.0209)**	**(0.0264)**	**(0.0177)**	**(0.0338)**	**(0.0147)**	**(0.0161)**

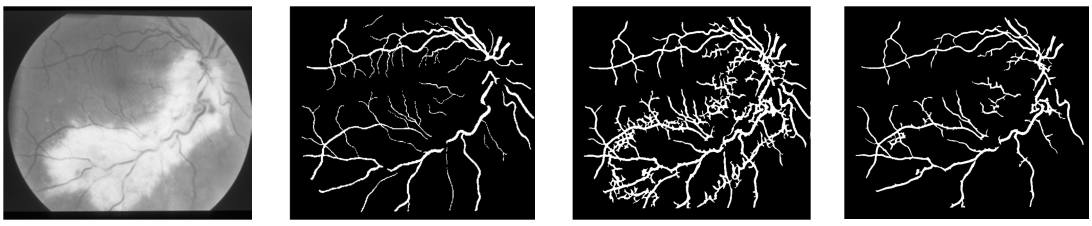

(a) (b) (c) (d)

Figure 4.4 The comparison of vessel segmentation results using our and Chanwimaluang method. (a) is pre-processed image; (b) is its ground truth; (c) is the segmentation result using Chanwimaluang method; and (d) is the segmentation result using our method.

In addition, the algorithm's performance was also measured with receiver operating characteristic (ROC) curves (see section 2.21.2 for details). The ROC curves for each image

are obtained by manually thresholding the image with the threshold values starting from 0 to 1 in a step of 0.01 (e.g. Figure 4.5). The areas under the ROC curves for both the original method and our method are listed in Table 4.1. Az indicates the area under the ROC curves, also known as AUC.

Considering the sensitivity, specificity, accuracy and the ROC curve, we can say that the modified method improves the segmentation performance compared to original method, particularly reduces the miss-segmentation rate (FPF) which is the rate at which tissue not belonging to vessel are miss-segmented as vessels. Observing from Figure 4.5, in contrast to the original method's plus (+symbols) points line, we can find that the red point curve plotted closer to the top left corner. This also confirms our method achieves some success in reducing the effects caused by drusen which present as light spots in the image and produce false positives.

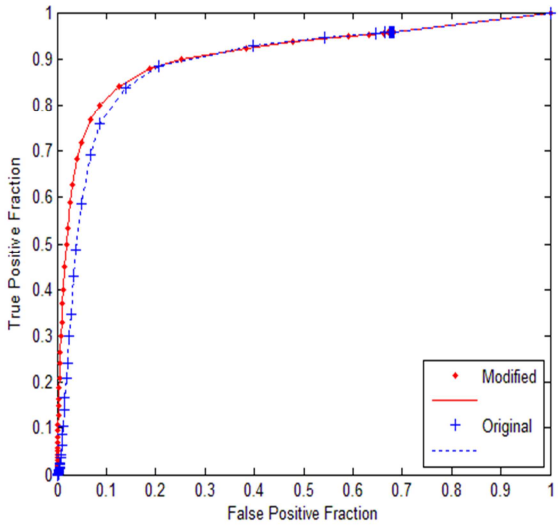

Figure 4.5 ROC curves for the first image of STARE

4.5 Chapter conclusion and discussion

In this chapter, we demonstrated the effect of brighter anomalies on vessel segmentation in retinal fundus images. We propose a retinal vessel segmentation scheme using a Log-Gabor filter and a matched filter. A Log-Gabor filter is employed to detect drusens which manifest as bright areas in the image. Drusens can cause errors in the vessel segmentation. Considering our experimental results (the sensitivity 0.7216, specificity 0.9628 and accuracy 0.9442 with AUC area under the ROC curve 0.9317) compare with original method (sensitivity 0.7402,

specificity 0.9508 and accuracy 0.9308 with AUC area under the ROC curve 0.9285) we can conclude that our method improves the segmentation performance compared to the original method, particularly reduce the miss-segmentation rate (FPF) which is the rate at which the tissue not belonging to vessels are miss-segmented as vessels.

Nevertheless, recalling our scheme, the segmentation algorithm is primarily based on the local entropy of the grey level co-occurrence matrix, in which the joint distribution of the grey levels of two neighbouring pixels is considered as a texture feature for classification. However, it is not strong enough to discriminate vessel related textures, since a fundus image contains other components (OD, exudates, and macula), and even the vessel tree has various texture characteristics (different width, tortuosity, reflection, artificiality). Moreover, the retinal fundus image has low and inconsistent contrast between the vessels and background, especially for those capillaries in the images which have very similar appearances compared to the background. This phenomenon may result in the misclassification of those capillaries. In this case, we would like to say that the retinal vessel segmentation using only one global threshold based on low level feature extraction and discrimination techniques will encounter a bottleneck to accurately distinguish vessel and non-vessel objects. In the next chapters, we will introduce more sophisticated schemes for vessel and non-vessel feature extraction and classification by using the texton concept based on understanding limitations of techniques adopted in this chapter.

Chapter 5

5. Texton based retinal vessel segmentation experiments

Although numerous automatic retinal vessel segmentation methods on fundus images have been proposed in the past (referring to the comprehensive review of those methods presented in chapter 2), it is still a big challenge; and retinal vessel segmentation remains a focus for ongoing research. In this chapter we focus on structural texture-based segmentation techniques known as textons (see chapter 3 for details), as only a few authors [197] have investigated this approach for retinal vessel segmentation and it provides a framework for learning texture features which is founded in human perception. This chapter describes three sets of experiments about our texton-based retinal vessel segmentation schemes. In the first experiment, a supervised texton-based retinal vessel segmentation method is introduced, in which the textons are trained on vessel and background samples separately. The second experiment improves the scheme by introducing a machine learning stage to distinguish corresponding vessel textons from background textons. Moreover, to pursue an automatic vessel segmentation method that does not require excessive retraining and is robust to noise and variation in image capture, we performed the third set of experiments on retinal images captured in three different datasets, generating textons from one set and testing on the other two data sets. The third experiment reveals that it is possible to train a set of general texons based on our proposed scheme, which can be used as a general tool for retinal vessel segmentation for other image databases. The three experiments are detailed in section 5.1, 5.2 and 5.3, each of which presents its corresponding experimental results and evaluations.

5.1 Supervised texton based retinal vessel segmentation

In this experiment, segmentation is performed using an approach that classifies each pixel in a fundus image as vessel or non-vessel. The classifier is designed using a supervised learning scheme, in which vessel relative textons are trained on vessel related responses and non-vessel textons are trained from responses to non-vessel structure. The training samples are obtained using ground truth to label vessel and non-vessel objects in response to a fundus

image. Textons are learnt from the responses of a filter bank which is applied to each image in the training set. For example, suppose there are *n* filters, then the response of filter F_i is given by

$$R_i(x, y) = F_i * I_{(x,y)} \qquad (5.1)$$

where $*$ denotes the convolution operation. The filter responses form an *n*-dimensional vector $\mathrm{R} = [R_1, R_2, \ldots R_n]^T$ at each pixel position in the image. Filter responses from pixels in *m* training images are clustered using the *k*-means algorithm into *k* groups. These *k* clustering centres form a set of prototype response vectors known as textons.

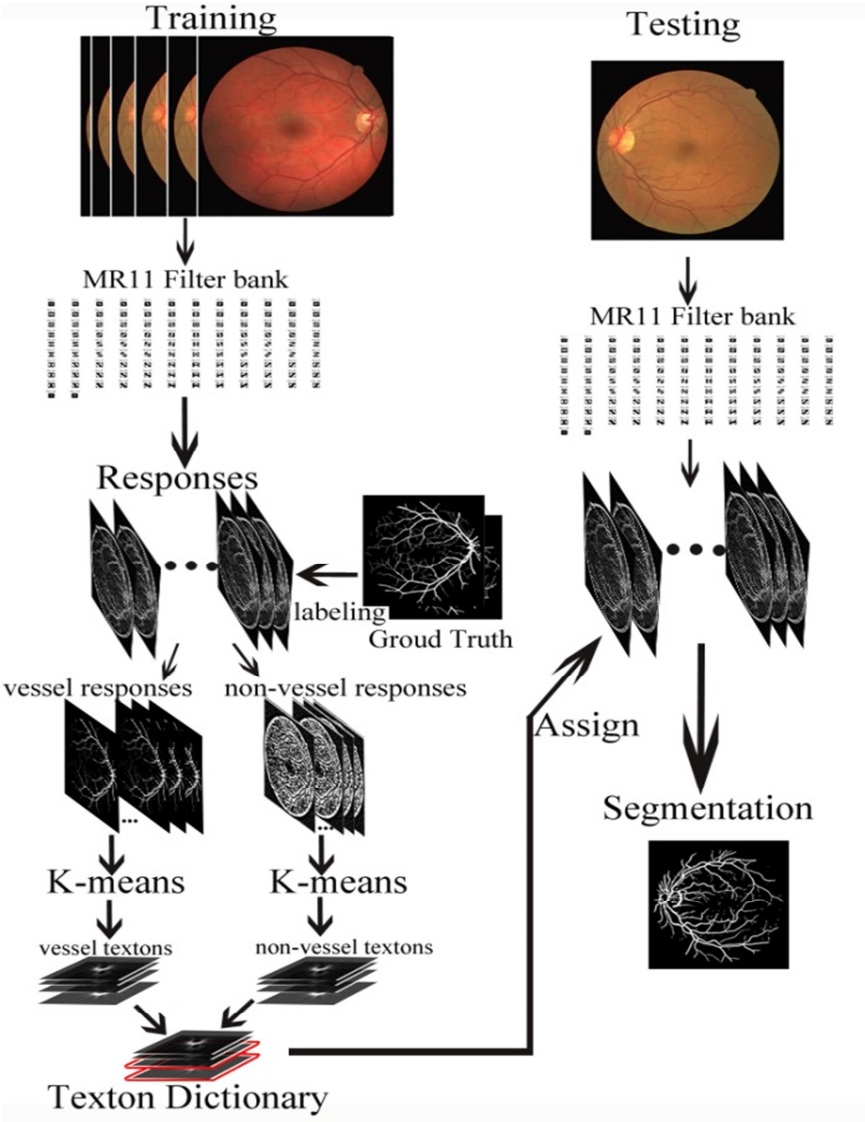

Figure 5.1 The framework of a supervised texton based retinal vessel segmentation method.

Note that in our first experiment, the vessel related textons and non-vessel textons are trained separately and stored into a textons dictionary which can be used in the testing stage. In the testing stage, the same filter bank is applied to each novel image and pixels are classified as vessel or non-vessel by mapping the responses onto cluster centroids representing each class in the multidimensional feature space. Figure 5.1 illustrates this procedure.

5.1.1 Feature extraction using the MR11 Filter bank

Design of a filter bank is an important part of any system using textons and different sets of filters have been identified in previously published work. Varma and Zisserman [139][176] examined the significance of a so-called maximal response 8 (MR8) filter bank in their proposed framework which is used to classify natural texture patterns (see section 3.2.4 for more details). Adjeroh et al. [197] considered the problem of designing a filter bank for retinal images and proposed a correlation-based refinement of filters in previous retinal segmentation studies. For our retinal vessel application we designed a new filter bank to extract features from vessels by considering their photometric and structural properties. The most significant properties for vessel extraction are vessel width and angles. As we described in previous chapters, the vessel networks have wide range of vessel widths (from 2-15pixels), and they may be at any orientation in fundus images. In addition, a fundus image contains other anatomic components (such as OD and macular) and some pathological changes; various artefacts such as vessel light reflection may also appear on the vessel surface. In practice, vessel networks (arteries, veins and capillaries) are typically bar structures and the vessel cross-sectional intensity profile can be approximated by a Gaussian shaped curve. With this in mind, we employed the second-order derivative Gaussian filter that forms part of the MR8 filter bank. Let's define the one dimension (1D) Gaussian function as follows:

$$G(x) = \frac{1}{\sqrt{2\pi}\sigma} e^{-\frac{x^2}{2\sigma^2}} \tag{5.2}$$

The two dimension Gaussian function is given by:

$$G(x,y) = \frac{1}{\sqrt{2\pi}\sigma_x} e^{-\frac{x^2}{2\sigma_x^2}} \times \frac{1}{\sqrt{2\pi}\sigma_y} e^{-\frac{y^2}{2\sigma_y^2}} \tag{5.3}$$

First and second order derivative 1D Gaussian functions are given by

$$G'(x) = \frac{x}{\sqrt{2\pi}\sigma^3} e^{-\frac{x^2}{2\sigma^2}} \quad (5.4)$$

$$G''(x) = \frac{1}{\sqrt{2\pi}\sigma^5}(x^2 - \sigma^2) e^{-\frac{x^2}{2\sigma^2}} \quad (5.5)$$

Therefore according to equation 5.3 and 5.5, the second order partial derivative of $G(x, y)$ with respect to the y-axis direction can be given by

$$\frac{\partial''_{G(x,y)}}{\partial_y} = \frac{1}{\sqrt{2\pi}\sigma_x} e^{-\frac{x^2}{2\sigma_x^2}} \times \frac{1}{\sqrt{2\pi}\sigma_y^5}(y^2 - \sigma_y^2) e^{-\frac{y^2}{2\sigma_y^2}} \quad (5.6)$$

In order to allow the filter kernel to be rotated to any orientation, an orthonormal rotation matrix $\begin{bmatrix} \cos\theta & -\sin\theta \\ \sin\theta & \cos\theta \end{bmatrix}$ is multiplied by matrix $\begin{bmatrix} x \\ y \end{bmatrix}$, hence the equation 5.6 can be converted to

$$\frac{\partial''_{G(x',y')}}{\partial_y} = \frac{1}{\sqrt{2\pi}\sigma_x} e^{-\frac{x'^2}{2\sigma_x^2}} \times \frac{1}{\sqrt{2\pi}\sigma_y^5}(y'^2 - \sigma_y^2) e^{-\frac{y'^2}{2\sigma_y^2}} \quad (5.7)$$

where

$$x' = x\cos\theta - y\sin\theta$$

$$y' = x\sin\theta + y\cos\theta$$

In our experiment, the second order derivative Gaussian filter is applied at 3 scales (σ_x,σ_y) ={(1,3), (1.5,4.5), (2,6)}, and the anisotropic filter kernel at each scale is rotated in 12 orientations (0, 15^o, 30^o, 45^o, 60^o, 75^o, 90^o, 105^o, 120^o, 135^o, 150^o, 165^o). These filter kernels are illustrated in the rows1-3 of Figure 5.2.

Under a specific illumination condition, a retinal image may contain some photometric anomalies. These may include effects such as the vessel reflection problem. In [118], Wang et al. proposed a model based method to address this problem. The vessel profile which contains specular reflection is modelled by a Hermite Gaussian model. In our work, to address this we employ a Difference of Gaussians (DoG) filter proposed by Gao et al. [198]. In equation 5.3, assume the σ_y equals $3\sigma_x$ to make the filter to be an anisotropic kernel, in which σ_x or σ_y is the standard deviation which defines the spread of the intensity profile. The 2D Gaussian function can be converted to

$$G_{\sigma_x}(x,y) = \frac{1}{6\pi\sigma_x^2} e^{-\frac{1}{2}(\frac{x^2}{\sigma_x^2}+\frac{y^2}{3\sigma_x^2})} \quad (5.8)$$

Then the DoG is expressed as

$$DoG_{\sigma_{x1},\sigma_{x2}}(x,y) = G_{\sigma_{x1}}(x,y) - AG_{\sigma_{x2}}(x+\delta,y) \quad (5.9)$$

where the offset parameter δ in equation 5.9 represents the centre position of the vessel over a cross section. In reality, the vessel reflection may not just appear exactly on the centre line. Under this circumstance, the offset parameter can be adjusted based on the location of the light reflection. The parameter *A* is used to regulate the amplitude of the Gaussian function. It combines with the multiplier $(1/6\pi\sigma_x^2)$ of the Gaussain function that controls the intensity of curves. The amplitude parameter *A* is chosen as $1/\pi$ in order to avoid an overlarge amplitude of the Gaussian curves, as in reality, although the vessel light reflections are brighter than vessels, their illumination conditions are still within a certain range, for instance, they are not brighter than some exudates or the OD. Parameters σ_{x1} and σ_{x2} represent the spread of the Gaussian curve chosen to fit different vessel diameters. In our experiments we found that δ = 0.5, 0.75, 1.0 are appropriate values for $(\sigma_{x1}, \sigma_{x2})$= {(1.5, 0.5), (1.5, 0.8), (2, 1.4)}, respectively. Rows 4-6 of figure 5.2 illustrate the DoG filter. Our filter bank also includes a matched filter modelled as the general Gaussian function described in section 4.3.1. For the parameter σ we choose σ = 1, 1.5, 2 pixels, respectively. The length of the vessel segment *L* was set to 9. These values match structural properties in our dataset and others have used similar values [85]. The matched filters (at 3-scales) are shown in Figure 5.2, rows 7-9.

Since the Difference of Gaussian (DoG) and Matched filters (MF) like the second-order derivative Gaussian (2DG) are anisotropic filters (shown in Figure 5.2, rows 1-9), to detect the vessels at different orientations, the filter kernel has to be rotated. In our study, anisotropic filter kernels are presented in 12 orientations (columns 1-12). All anisotropic filters are applied at 3 scales using a filter kernel size of 16×15 pixels to estimate different widths of vessels. For the anisotropic filters the maximal response, across all orientations, represents its output. We also employ two isotropic Gaussian and LoG filters to extract general image features from the background and vessel boundaries (Figure 5.2, row 10, col's 1-2). Consequently, the proposed filter bank comprises of 110 filters but only 11 filter responses are obtained, hence we named it MR11.

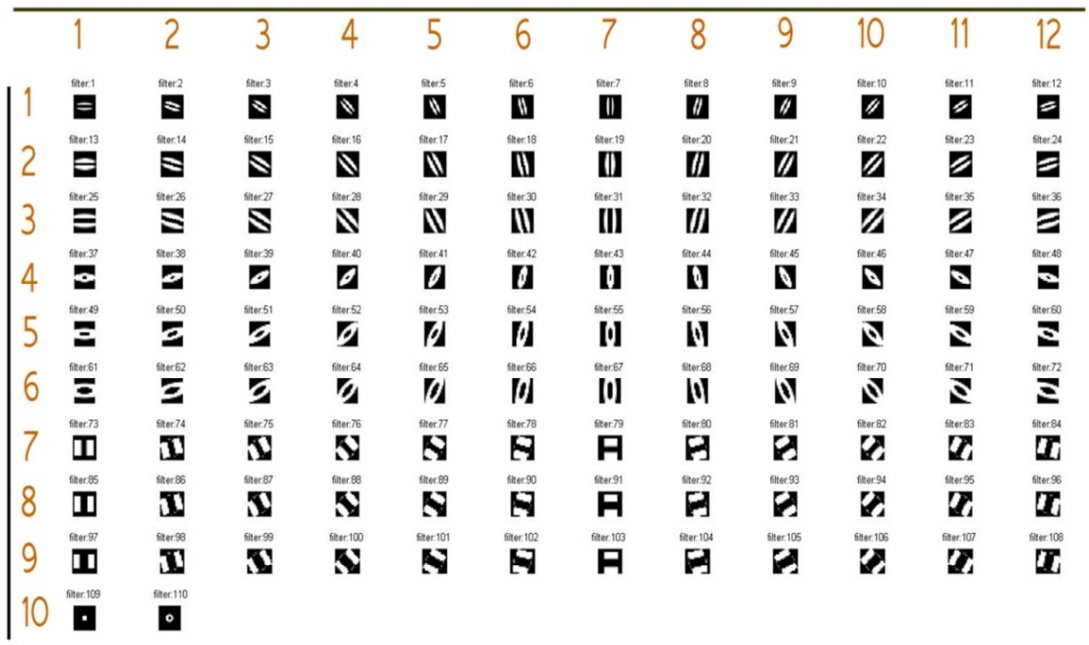

Figure 5.2 Filter bank MR11 for vascular feature extraction

We should point out that in some cases the second order derivative of Gaussian has better performance than the Matched Filter. Figure 5.3 (a1) and (a2) illustrate the second order derivative of Gaussian response and Matched Filter response, respectively, which are derived from an example image (a). A comparison of these filter responses is analysed by using ROC curve. As we can see in Figure 5.3 (b), the solid curve of second order derivative of Gaussian plotted closer to the top left corner compared to the dot line curve of the Match Filter. The corresponding AUCs of second order derivative of Gaussian and Matched filter are 0.9380 and 0.9341, respectively. However, this does not mean that the second order derivative of Gaussian always outperforms the Matched filter. In contrast, for the fundus image contains large width vessels, the Matched filter has better performance. A vessel reflection phenomenon presented in a square area of Figure 5.3 (a) is amplified and illustrated in Figure 5.3(c). Figure 5.3 (c1) and (c2) are the filter responses to the second order derivative of Gaussian and the difference of Gaussian, respectively. Comparing (c1) to (c2), we can observe that the shadow in (c1) caused by vessel reflection is removed in (c2). Considering respective advantages and disadvantages of different filter categories, we combine these filter categories into the MR11 filter bank to extract more sophisticated vessels features from fundus images. After applying the filter bank on an image, each pixel is converted into 11-D feature vector, which can be further used in a subsequent stage to generate textons.

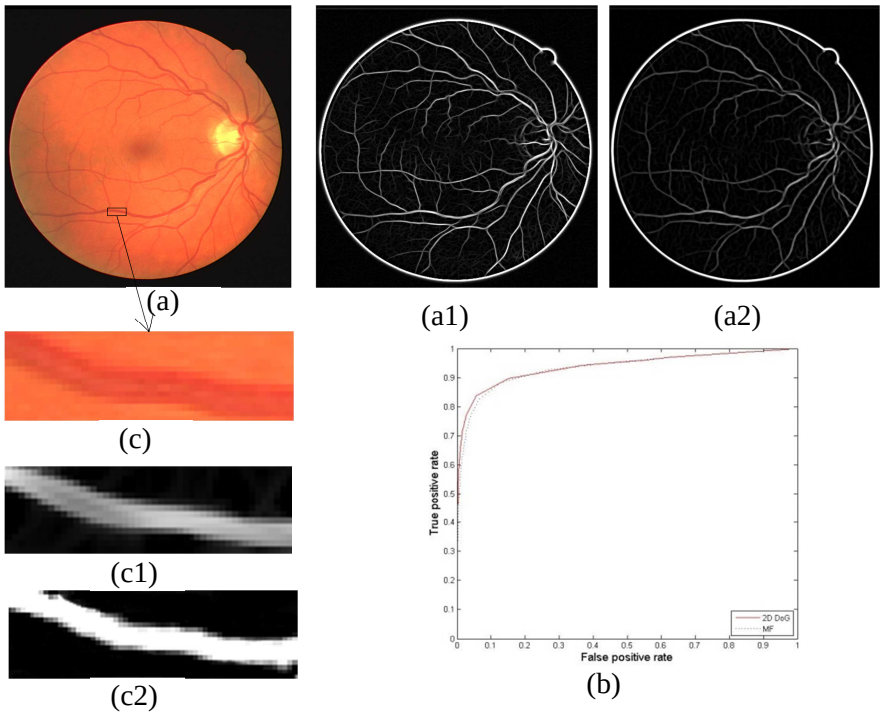

Figure 5.3 Comparisons of responses to filters in MR11 filter banks. (a) is an example image; (a1) is the (a) filter response to second order derivative of Gaussian at scale ($\boldsymbol{\sigma_x}$,$\boldsymbol{\sigma_y}$)=(1.5, 4.5); (a2) is the matched filter response at scale $\boldsymbol{\sigma}$=1.5; (b) illustrates ROC plots for both second order derivative of Gaussian an Matched filter. (c) is an amplified vessel reflection presented in (a); (c1) is the filtering result using the second order derivative of Gaussian; and (c2) is the filtering result using difference of Gaussian.

5.1.2 Textons generation and segmentation

In our experiment, textons were trained from the MR11 filter bank responses generated from training samples, from which we extracted local features of retinal vessels. The training procedure includes two stages. In the vessel texton training stage, the texton computing procedure was implemented on filter responses in which the non-vessel related responses were identified using ground truth and removed. To train non-vessel texons, the vessel related areas in responses were removed in order to obtain non-vessel background responses. The textons were generated by employing a *k*-means clustering algorithm on the filter responses. As representations of texture, the textons were aggregated based on the properties of distances calculated from memberships to clustering centres. The clustering procedure is an iterative process. Initially, *k* random points were selected as default means (centroids) of *k* clusters. Corresponding memberships were selected based on differences of Euclidean distance between means and centre bins. New means of those memberships were calculated again and were defined as new clustering centres. The process runs iteratively until it

converges. The flowchart of this algorithm is illustrated in Figure 5.4. Both vessel textons and background textons were stored in a texton dictionary and subsequently used in the test stage. At the test stage, the trained textons were assigned depending on responses of the filter bank and then the corresponding texton memberships are calculated by assigning each pixel to the nearest cluster centre (texton) based on the Euclidean distance. The vessel texton related memberships generate texton maps and the segmentation results are obtained by combining vessel texton related maps. At the vessel texton training stage, we applied two schemes for selecting the value of *k*. Initially, as a direct way that we chose *k*=2, i.e. one class for vessel texton and the other representing background texton. Then considering the natural condition of fundus images comprising those vessels that also contain light reflection and backgrounds which contain pathological anomalies (exudates, drusen, etc.), we chose *k*=4; two vessel related textons and two non-vessel related textons. The iteration parameter of the *k*-means algorithm determines the efficiency of performance. The iteration parameter=30 is chosen empirically in our experiment, taking into consideration both complexity and performance of the algorithm. This value is selected based upon an experimental evidence that iteration=30 and iteration=50 have the similar performance for clustering in training images.

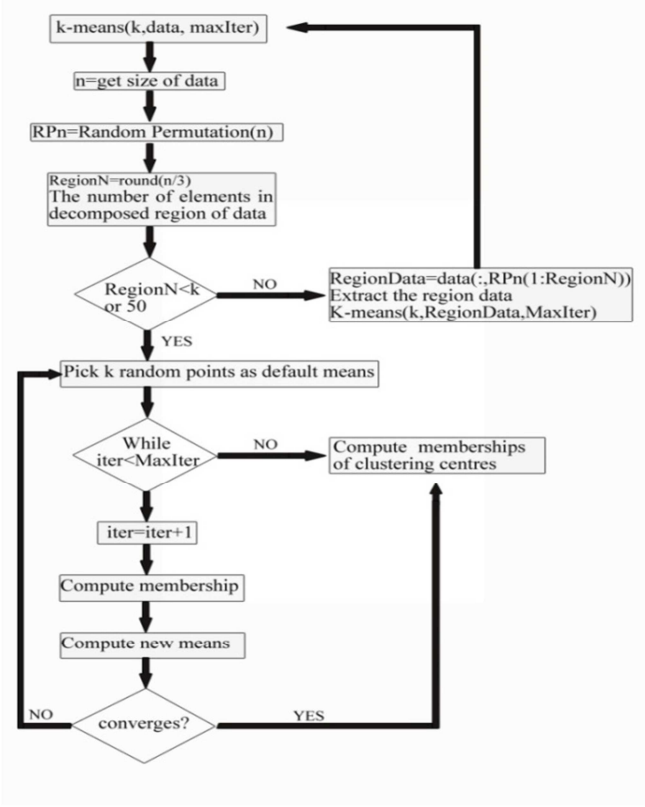

Figure 5.4 Flowchart of texton generation algorithm

5.1.3 Experimental results and evaluation

The proposed method was tested and evaluated on the DRIVE data set which has been introduced in subsection 2.2.1 of chapter 2. In order to quantify the performance of the proposed approach, segmentation results are compared to corresponding ground truths. The ground truth is defined by a binary vessel mask in which all vessel pixels are set to one and all non-vessel pixels are set to zero. The DRIVE database is divided into training and test sets where each set consists of 20 images.

For the test set, two sets of manual segmentations are provided by two observers. The first observer's manual segmentations are used as ground truth in our experiment. Figure 5.5 illustrates two examples of segmentation results, in which the first row (a) and (b) are original fundus images, the second row (a1) and (b1) are corresponding ground truths. The third row (a2) (b2) are segmentation results using the 2 textons set, and the last row illustrates segmentation results using 4 textons set. Visually, the segmentation results of using 4 texons are more detailed than using 2 textons segmentations, especially for the arterioles, venules and capillaries, but with more isolated objects which may be fragmentary vessel segments or noise. This phenomenon is also confirmed by our evaluation of segmentation shown in the table 5.1.

Our algorithm was evaluated in terms of sensitivity, specificity and accuracy (see subsection 2.2.1 for details). Table 5.1 illustrates the evaluation results for each test image in test set using k=2 and k=4 in our algorithm. For k=2, the average specificity reaches 0.9806 with 0.7325 sensitivity, the average accuracy is 0.9587. The values of specificity, sensitivity and accuracy for the k=4 are 0.9524, 0.8323, 0.9422, respectively. We can see that there is an increasing sensitivity of using 4 textons compared to sensitivity of using 2 textons whilst the specificity of 4 textons is lower than the specificity of 2 texton. This is because segmentation using 4 textons set contains more misclassified non-vessel elements than 2 textons set (see Figure 5.5).

The primary limitation of this scheme is the high computational cost, as the training procedure has to implement the clustering computation twice, one for vessel related textons generation and the other for non-vessel textons generation. With this in mind, we improved our initial method by proposing a new texton generation scheme which is described in the next section.

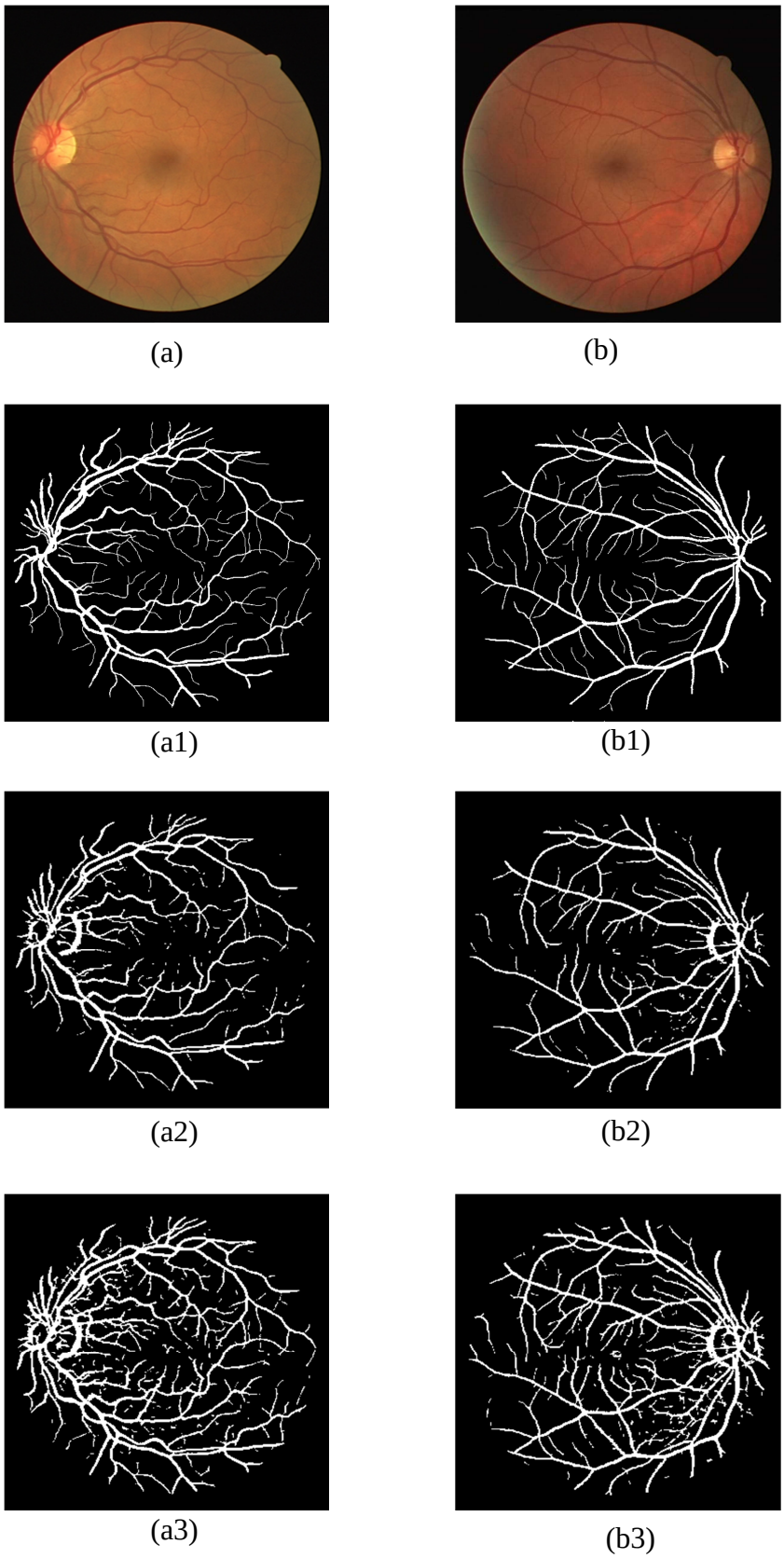

Figure 5.5 Examples of segmentation results using two textons (the third row a2, b2) and four textons (the fourth row a3, b3); (a)(b) are original images and (a1)(b1) are their corresponding ground truths.

Table 5-1 Performance results on DRIVE database using 2 texons and 4 textons

Image	Sensitivity		Specificity		Accuracy	
	K=2	K=4	**K=2**	K=4	**K=2**	K=4
01test	0.8190	0.8990	0.9758	0.9471	0.9618	0.9428
02test	0.7545	0.8419	0.9844	0.9603	0.9609	0.9482
03test	0.6612	0.7831	0.9847	0.9562	0.9524	0.9390
04test	0.7397	0.8203	0.9807	0.9526	0.9586	0.9404
05test	0.6677	0.7763	0.9905	0.9729	0.9603	0.9544
06test	0.6526	0.7650	0.9880	0.9700	0.9554	0.9500
07test	0.7112	0.8141	0.9769	0.9403	0.9527	0.9403
08test	0.6476	0.7769	0.9773	0.9496	0.9490	0.9347
09test	0.6612	0.7855	0.9882	0.9704	0.9617	0.9554
10test	0.7040	0.8087	0.9834	0.9633	0.9604	0.9506
11test	0.7245	0.8186	0.9775	0.9418	0.9549	0.9307
12test	0.7429	0.8410	0.9797	0.9482	0.9593	0.9390
13test	0.7110	0.8116	0.9796	0.9510	0.9533	0.9374
14test	0.7786	0.8670	0.9724	0.9345	0.9568	0.9290
15test	0.7968	0.8767	0.9663	0.9215	0.9541	0.9183
16test	0.7603	0.8641	0.9826	0.9565	0.9625	0.9481
17test	0.7252	0.8358	0.9788	0.9446	0.9574	0.9354
18test	0.7828	0.8800	0.9782	0.9482	0.9627	0.9428
19test	0.8440	0.9086	0.9837	0.9580	0.9722	0.9539
20test	0.7658	0.8718	0.9825	0.9604	0.9666	0.9539
Average	**0.7325**	**0.8323**	**0.9806**	**0.9524**	**0.9587**	**0.9422**

5.2 An improved supervised texton based retinal vessel segmentation

In this experiment, the segmentation method is improved by modifying the texton training stage. In this framework, the classifier is designed using a supervised learning algorithm to generate textons based on our previous experiment. This learning algorithm aims to reduce the computational cost of the vessel segmentation algorithm so that its efficiency can be

improved. Our aim is to change the framework shown in Figure 5.1 and to use only one *k*-means clustering procedure to generate all the texton maps.

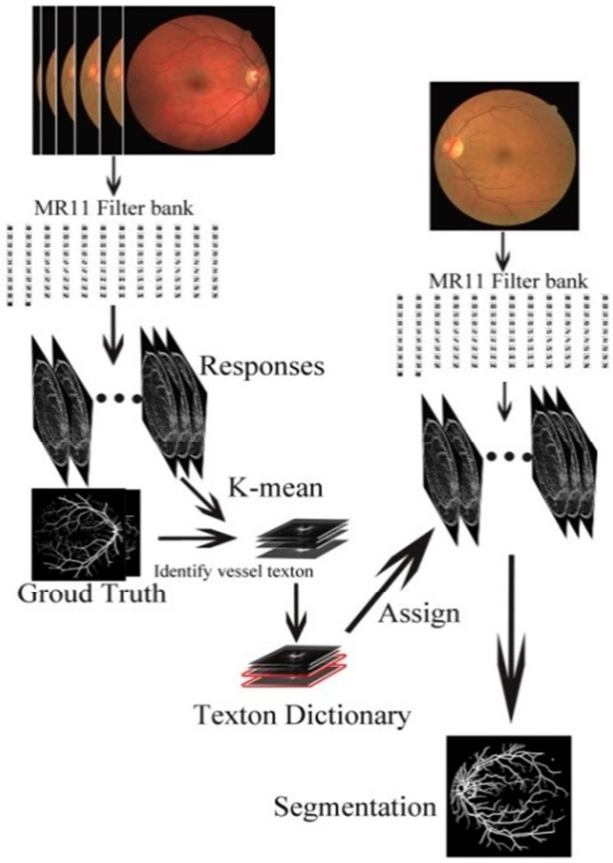

Figure 5.6 The framework of improved supervised texton based retinal vessel segmentation method.

5.2.1 The improved scheme of texton generation

Given the structures within retinal images, normally each scan consists of five classes of objects; background, vessel tree network (possibly exhibiting light reflection anomalies), OD, and other pathological changes (particularly found in images of patients). In this scheme, we chose 5 textons to reflect significant classes of those objects that are visible in the images. The textons are computed by applying the same MR11 filter bank to each image in the training sample to get 11 classes of filter responses. We use the *k*-means algorithm once to cluster the filter responses into k=5 groups identified by their cluster ID (k=1…5). We run the *k*-means algorithm until either it converges or the number iterations reaches a limit (30). To determine the vessel texton class membership from the ground-truth, we first rank the clusters based on their size. The largest cluster in the list maps onto the background pixels. The

remaining clusters are considered as textons. These are subjected to further analysis to identify optimized combinations. For instance, we got four texton ID which are 1, 2, 3, 4, respectively. There are 11 combinations of these four textons related memberships (map), namely, (1, 2), (1, 3), (1, 4), (2, 3), (2, 4), (3, 4), (1, 2, 3), (1, 2, 4), (1, 3, 4), (2, 3, 4) and (1, 2, 3, 4). Each combination is evaluated with regard to accuracy by back-projecting the clustered pixels and recovering their ground truth labels. We store the combination with the highest accuracy and its corresponding texons ID represent the vessel related textons. Figure 5.7 illustrated the trained textons dictionaries from the STARE and DRIVE databases, in which each dictionary contains 5 textons. Each texton is a 11 dimensional vector and assigned by an integer ID [1,K]. Figure 5.7 (a) is the dictionary from STARE, showing IDs (1, 2, 5) are indicated as vessel related textons and IDs (3, 4) are non-vessel textons. Figure 5.7 (b) is the textons dictionary from the DRIVE dataset, where IDs (2, 3, 4) are vessel textons and the IDs (1, 5) are non-vessel textons. These identifications of textons are trained based on the training scheme described above. These dictionaries of stored textons will be used to evaluate the vessel segmentation in a subsequent testing stage.

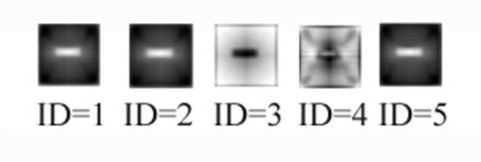

(a) STARE textons dictionary

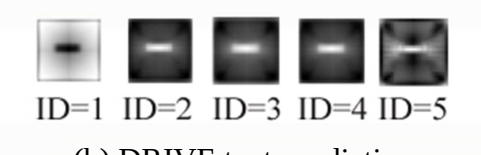

(b) DRIVE textons dictionary

Figure 5.7 Textons dictionaries of STARE and DRIVE database. (a) is the STARE textons dictionary, IDs (1, 2, 5) are indicated as vessel related textons and IDs (3, 4) are non-vessel textons; (b) is the DRIVE textons dictionary, IDs (2, 3, 4) are vessel textons and IDs (1, 5) are non-vessel textons.

5.2.2 Experimental results and evaluation

In this experiment, the improved method was tested and evaluated on both STARE and DRIVE datasets (described in section 2.3). The DRIVE database includes training and testing

sets. The STARE database is not pre-split into training and testing sets, but it provides 40 images with two sets of associated ground truth, hand labelled by two experts. In our evaluation, 20 images which have been tested by many other authors are grouped into the test dataset; the 20 remaining images in the database are assigned to the training dataset. For both databases, the textons are trained on the training samples, and are tested on the 20 remaining images.

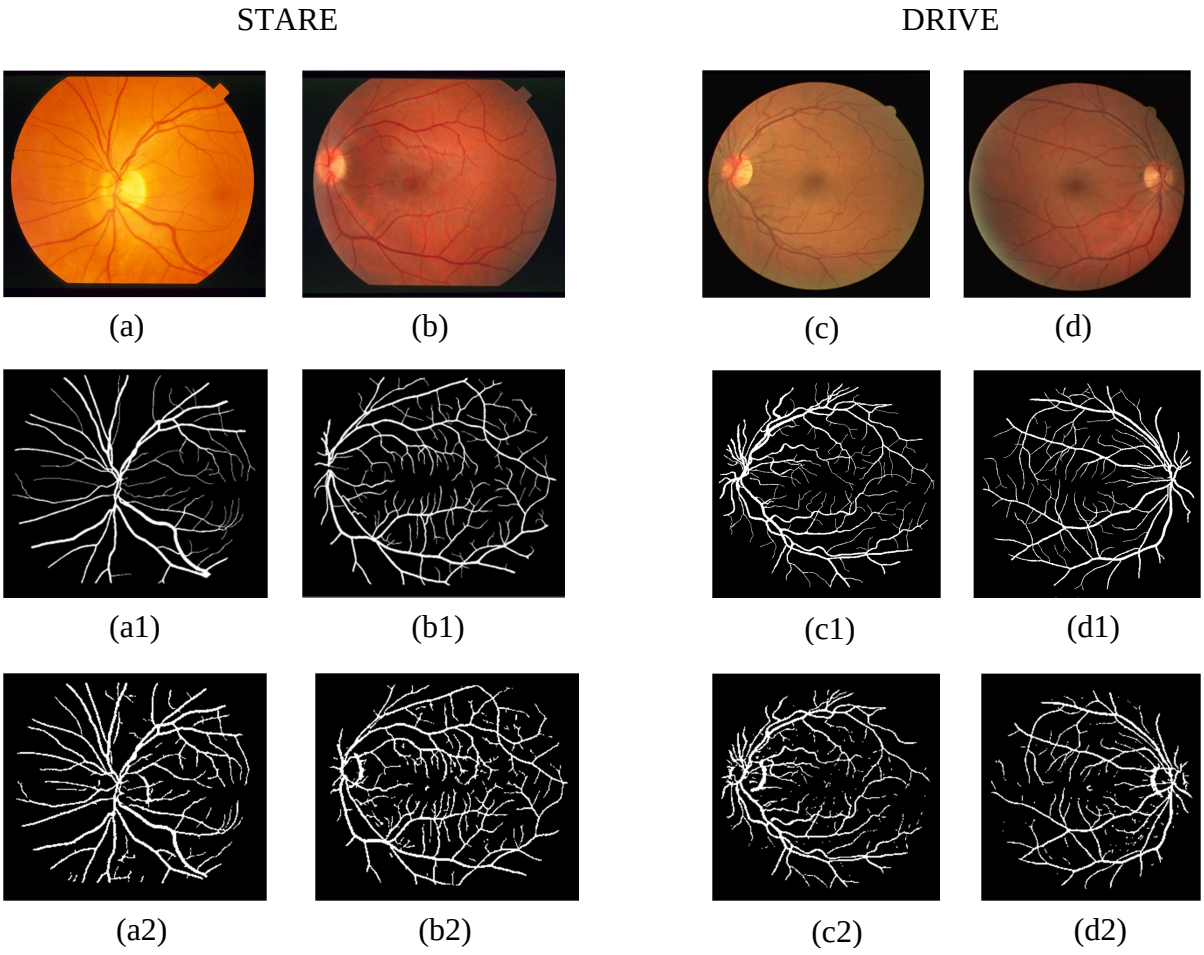

Figure 5.8 Examples of segmentation results using improved supervised texton based method. The first row (a) (b) (c) (d) shows original colour fundus images; The second row (a1) (b1) (c1) (d1) illustrates corresponding ground truths; the bottom row (a2) (b2) (c2) (d2) are vessel segmentation using our improved scheme.

Examples of our retinal vessel segmentation results on both STARE and DRIVE database are shown in the Figure 5.8, of which the left two columns relate to the STARE database and the right two columns illustrate the original images and segmentation results with respect to the DRIVE database. The first row (a) (b) (c) (d) in Figure 5.8 shows original colour fundus

images. The second row (a1) (b1) (c1) (d1) illustrates corresponding ground truths. The segmentation results using the improved scheme are illustrated on the bottom row.

The algorithm was also evaluated by standard measurements of sensitivity, specificity and accuracy. On the STARE database, average specificity reaches 0.9643 with 0.7517 sensitivity, the average accuracy is 0.9506. The values of specificity, sensitivity and accuracy for the DRIVE dataset are 0.9831, 0.7167 and 0.9591, respectively.

Table 5-2 Performance results on STARE and DRIVE databases using improved supervised retinal vessel segmentation on fundus images

Image STARE	Sensitivity	Specificity	Accuracy	Image DRIVE	Sensitivity	Specificity	Accuracy
Im0001	0.7029	0.9366	0.9180	**01test**	0.8036	0.9784	0.9628
Im0002	0.6460	0.9459	0.9259	**02test**	0.7377	0.9864	0.9609
Im0003	0.6547	0.9558	0.9750	**03test**	0.6439	0.9865	0.9524
Im0004	**0.4588**	**0.9938**	**0.9541**	**04test**	0.7246	0.9835	0.9597
Im0005	0.6507	0.9741	0.9449	**05test**	0.6510	0.9918	0.9599
Im0044	0.7647	0.9706	0.9562	**06test**	0.6370	0.9894	0.9551
Im0077	0.8869	0.9413	0.9369	**07test**	0.6913	0.9807	0.9543
Im0081	0.8867	0.9539	0.9489	**08test**	**0.6287**	0.9806	0.9503
Im0082	0.8595	0.9577	0.9500	**09test**	0.6432	0.9898	0.9617
Im0139	0.8350	0.9362	0.9280	**10test**	0.6891	0.9851	0.9608
Im0162	0.8898	0.9586	0.9537	**11test**	0.7114	0.9805	0.9564
Im0163	**0.9120**	**0.9634**	**0.9595**	**12test**	0.7263	0.9822	0.9601
Im0235	0.8347	0.9586	0.9476	**13test**	0.6946	0.9820	0.9539
Im0239	0.7845	0.9632	0.9477	**14test**	0.7637	0.9760	0.9588
Im0236	0.8411	0.9591	0.9484	**15test**	0.7818	0.9706	0.9571
Im0240	0.6562	0.9831	0.9497	**16test**	0.7452	0.9847	0.9630
Im0255	0.8548	0.9686	0.9584	**17test**	0.7090	0.9818	0.9587
Im0291	0.6944	0.9894	0.9745	**18test**	0.7702	0.9809	0.9642
Im0319	0.6053	0.9897	0.9731	**19test**	**0.8336**	**0.9863**	**0.9736**
Im0324	0.6109	0.9867	0.9616	**20test**	0.7481	0.9846	0.9672
Average	**0.7515**	**0.9643**	**0.9506**	**Average**	**0.7167**	**0.9831**	**0.9591**

Table 5.2 illustrates measurements of 20 test images for both STARE and DRIVE database, respectively. Each database has 20 testing samples which are numbered using their image file names. In practice, the sensitivity is much more important than the specificity, since the number of background pixels is larger than the number of vessel related pixels in a fundus image. As we can see from the table 5.2, the maximum and minimum sensitivity are 0.9120 and 0.4588 for STARE images. For the DRIVE images, the maximum sensitivity is 0.8336 and minimum sensitivity is 0.6370.

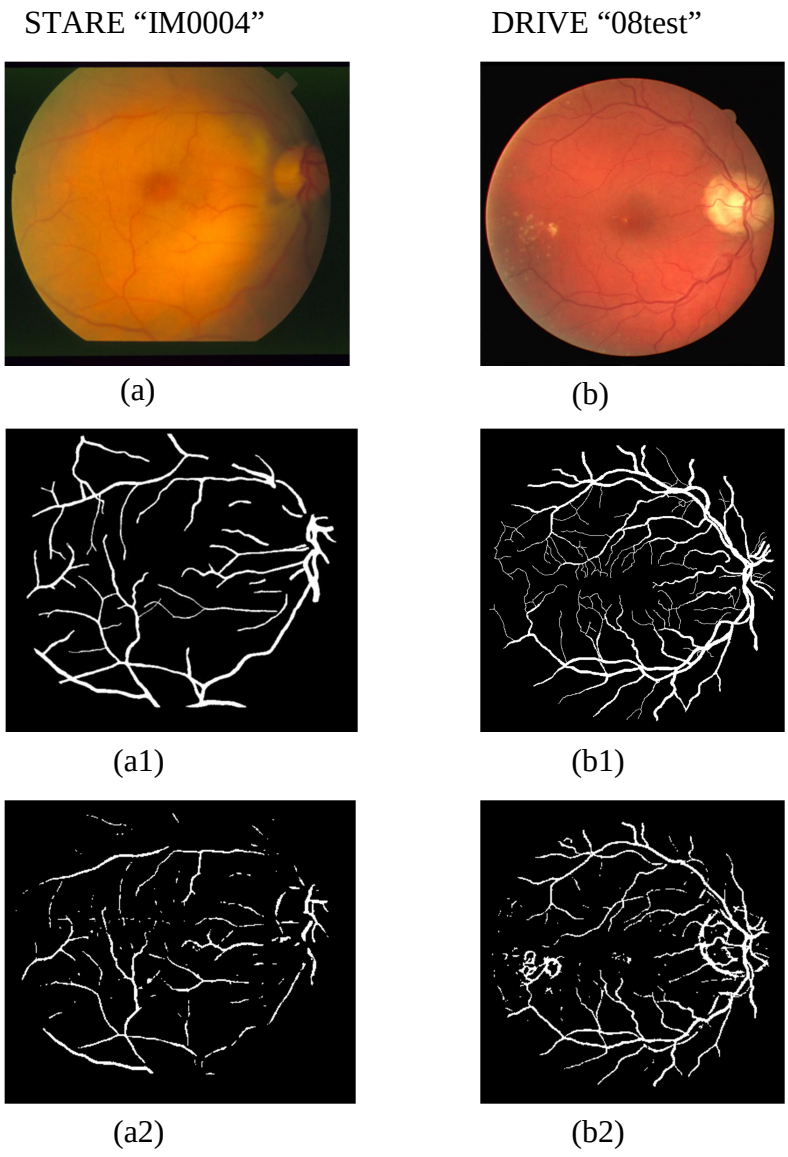

Figure 5.9 The segmentation results with the least sensitivity for both STARE and DRIVE databases. (a) (b) are test images of STARE and DRIVE databases; (a1) and (b2) are the ground truths and (a2), (b2) are the segmentation results

Figure 5.9 illustrates the cases with the worst sensitivity in the STARE and DRIVE database, in which (a) 'IM0004' is a test image of STARE and (b) is an image of DRIVE. Visually, the local contrast between vessels and background is extremely low in both (a) and (b). In figure 5.9 (b), most of vessels surrounding the macula cannot even be distinguished pre-attentively from the background by the human vision system.

Comparing the segmentation results (a2, b2) to the ground truths (a1) and (b2), respectively, we can see some vessel trees are miss-segmented. This low contrast condition is the critical factor that leads to the poor segmentation using the proposed method. Extremely low contrast between vessels and background is a common issue for retinal vessel segmentation, however there are no solutions that can handle it completely in the research community, to the best of our knowledge. We also compare our approach to other retinal vessel segmentation algorithms to set the performance of our method in context. Table 5.3 shows these comparative results of performance. Experimental results show that our proposed method outperforms some state-of-the-art methods, while the performance compares well with the best published results on both datasets.

Table 5-3 Comparison between our method with five other methods on STARE and DRIVE databases

Method	**Performance Results**			
	database	***Sensitivity***	***Specificity***	***Accuracy***
2nd human observer	STARE	0.8949	0.9390	0.9354
Our method	STARE	**0.7515**	**0.9643**	**0.9506**
Hoover[90]	STARE	0.6751	0.9567	0.9275
Soares [103]	STARE	0.7165	0.9748	0.9480
Marín [108]	STARE	0.6944	0.9819	0.9526
Staal [102]	STARE	0.6970	0.9810	0.9516
Zhang [89]	STARE	0.7177	0.9753	0.9484
2nd human observer	DRIVE	0.7761	0.9725	0.9473
Our method	DRIVE	**0.7167**	**0.9831**	**0.9591**
Mendonca [126]	DRIVE	0.7344	0.9764	0.9425
Soares [103]	DRIVE	0.7283	0.9788	0.9466
Zana [125]	DRIVE	0.6696	0.9769	0.9377
Staal [102]	DRIVE	0.7194	0.9773	0.9441
Zhang[89]	DRIVE	0.7120	0.9724	0.9382

5.3 Retinal vessel segmentation using general textons

Normally, similar objects in the natural world have similar properties, such as shape, colour, texture etc., and it is reasonable to believe that the similar objects should have similar structural primitives (textons). Consequently we can assume that the vessel or non-vessel elements in fundus images which are obtained from different databases should have similar textons that can be used as a general tool for retinal vessel segmentation. Under ideal circumstances it should even be possible to construct a unified vessel textons library, which can be employed for vessel segmentation on fundus images in any datasets. In order to verify this assumption, we set up an experiment on retinal images captured from three different datasets, in which texons trained on one data set were reused on other data sets. This experiment may not be sufficient to verify the assumption under the ideal circumstance, but it provides evidence of the feasibility and motivation for pursing an automatic vessel segmentation method that does not require excessive retraining and is robust to noise and variation in image capture methods. This experiment evaluates the performance of our proposed method and provides evidence to extend applications of our textons based methods.

5.3.1 Experimental setup

To verify the feasibility of using a unified texton as a general tool for retinal vessel segmentation in fundus images, we first adopt a statistical analysis method (paired t-test) to analyse the difference between two segmentation results which were obtained by using two sets of textons. The paired t-test has been widely used to prove whether differences between two methods are significant. A novel method can be qualified based on the performance of the other method. For the first experiment, our hypothesis is that if the textons trained from one dataset produce segmentation results on another dataset with similar or better performance compared to the manual segmentation or other proposed methods then this provides some evidence that unified textons may be an acceptable tool for retinal vessel segmentation.

Towards this direction, in our first experiments, test images from the DRIVE database were segmented by employing the textons trained from the STARE database. The first observer's manual segmentation of test images in the DRIVE database is defined as ground truth. The measures of the second observer's segmentation can be used to compare with the

measures of automatic machine segmentation using the STARE textons. Moreover, we also compared our results to the results published by Marín et al. [108], as they reported detailed measurements for each test image in the DRIVE database.

In the second experiment, we investigated the inter observer variability between two methods which use two sets of textons (one texton set is trained from the database itself and the other is trained from another independent database). We would like to compare this inter-observer variability with the inter observer variability of two expert segmentations of the same datasets. In the second experiment, we built a new independent data set which comprised 114 images collected from Manchester Royal Eye Hospital (MREH). Each image was digitized with a size 756×656 pixel and was stored as png format. 20 images were randomly selected as test samples, 20 of remaining images were used as training samples. We asked three ophthalmologists to manually segment retinal vessels from the background on 20 test images, in which one of the ophthalmologists provides ground truth on 20 training images and the manual segmentation of the senior expert is chosen as ground truth.

5.3.2 Comparative study of retinal vessel segmentation using general textons

In the first experiment, the textons from the STARE database were applied on the DRIVE test images to obtain the vessel segmentations (denoted as *our**). Then the result of each image was evaluated by standard measurements. The measured results of 20 DRIVE test images are illustrated in table 5.4, in which the average sensitivity, specificity and accuracy are 0.7795, 0.9706 and 0.9537, respectively. In order to provide the comparable measurements, the second observer's segmentations of the DRIVE database (denoted as *human*) were measured with average sensitivity, specificity and accuracy as 0.7761, 0.9725 and 0.9473 respectively. There are two sets of ground truth provided by two experts independently in the DRIVE database (refer to the section 2.2.1). Therefore, for manual segmentation measurement, by convention, if the manual segmentations provided by the first expert are defined as gourd truths, a set of measurements (sensitivity, specificity and accuracy) for each individual image in test dataset can be calculated by comparing the second expert manual segmentation to the ground truth (first expert segmentation). As a result, there are in total 20 sets of these measurements for 20 test images. The measurements of segmentation results (denoted as *Marín*) which were produced by *Marín* et al. are collected from their published paper in [108], where all their 20 sets of evaluation measurements are

reported. We analysed the differences among our method (*our**), human segmentation (*human*) and *Marín* method using the paired t-test based on respective 20 sets of evaluation measurements. Paired t-tests on the accuracy values for individual images of DRIVE database show that *our** performs significantly better than the *Marín* et al. with p-values= 6.58×10^{-8}, meanwhile the test results also demonstrate that *our** outperforms the *human* with p-values=4.75×10^{-4}. The corresponding results are illustrated by box-and-whisker plots in Figure 5.10. However, we can observe from the Figure 5.10 that the range of boxes related to the human segmentations is less than our method (*our**) for all three measures. This reflects that human segmentation has a more stable performance compared to automatic segmentation methods. The manual segmentation still needs to be approved in terms of robustness and reproducibility for vessel segmentation in the retinal images which are commonly inconsistent in image condition (illumination, contrast et al.) and quality.

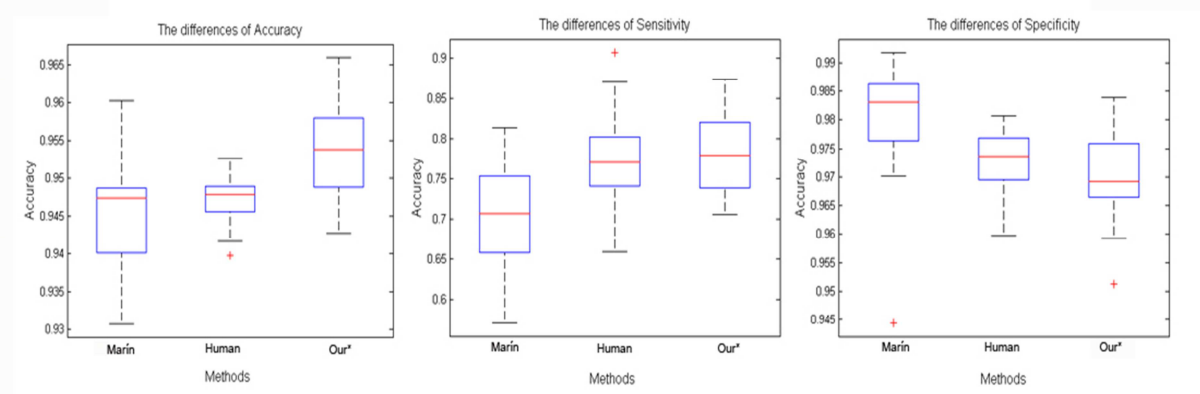

Figure 5.10 The box plots of accuracy, sensitivity and specificity for *Marín*, human and our* methods

In the second experiment, we further evaluated our approach by segmenting 20 images from the MREH data set. To investigate different training regimes we built two classifiers. The first was trained on the STARE images and the second was trained on a training subset of MREH images. Examples of segmentations are illustrated in Figure 5.11, in which the (a) is an original test image, (b) demonstrates the ground truth, (c) is the segmentation result using STARE textons and (d) is the segmentation result using textons trained from subset of MREH database. In each case the test set of MREH was evaluated in terms of sensitivity, specificity and accuracy, corresponding measurements are shown in table 5.5, of which the left part lists measurements of each case using MREH textons (denoted as MREH) and the

right part includes measurements of each case using STARE textons (denoted as MREH*). The average measurements of MREH are 0.7678, 0.9636 and 0.9447, the average measurements of MREH* are 0.7901, 0.9556 and 0.9397; sensitivity, specificity & accuracy respectively. The comparative results of these two classifiers are presented in Figure 5.12 (a).

Table 5-4 Measurement results on DRIVE database using STARE textons

Image DRIVE	Sensitivity	Specificity	Accuracy
01test	0.8539	0.9660	0.9560
02test	0.7938	0.9758	0.9571
03test	0.7212	0.9760	0.9506
04test	0.7806	0.9683	0.9510
05test	0.7223	0.9839	0.9594
06test	0.7055	0.9814	0.9545
07test	0.7578	0.9645	0.9456
08test	0.7082	0.9676	0.9453
09test	0.7232	0.9811	0.9602
10test	0.7529	0.9763	0.9579
11test	0.7631	0.9668	0.9486
12test	0.7896	0.9687	0.9532
13test	0.7594	0.9696	0.9490
14test	0.8230	0.9593	0.9483
15test	0.8323	0.9513	0.9428
16test	0.8063	0.9730	0.9580
17test	0.7786	0.9662	0.9504
18test	0.8273	0.9682	0.9570
19test	0.8742	0.9742	0.9659
20test	0.8176	0.9743	0.9628
Average	**0.7795**	**0.9706**	**0.9537**

To get the comparable measurements, we evaluated the inter observer variability between two expert segmentations of the same datasets (MREH) and present the results in Figure 5.12(b). A paired t-test result shows that accuracy and sensitivity of two expert segmentations are statistically significantly different with p-values=$4.7\text{x}10^{-4}$, $1.1\text{x}10^{-5}$, respectively. The mean of difference on accuracy and sensitivity are 0.0052 and 0.0535, respectively. Although a paired t-test on the accuracy, sensitivity of two segmentations (MREH, MREH*) shows that the inter observer variability between two methods is also different with p-values=$2.6\text{x}10^{-9}$,

$7.9x10^{-9}$, the mean of difference on the accuracy and sensitivity are 0.0050 and 0.0223 which are less than the differences of two ophthalmologists.

Both the first experiment and the subsequent experimental results provide evidence which demonstrates the robustness of our texton based retinal vessel segmentation method. The comparative study results reveal that textons derived from one database are sufficiently general to be operationally useful on other databases. This suggests that it may be feasible to generate a consistently updated unified texton dictionary which can then be used in several databases.

Table 5-5 Performance results on MREH database using two training regimes

MREH	Sensitivity	Specificity	Accuracy	MREH*	Sensitivity	Specificity	Accuracy
01test	0.7896	0.9441	0.9253	**01test**	0.8037	0.9327	0.9169
03test	0.7278	0.9849	0.9664	**03test**	0.7618	0.9815	0.9657
06test	0.7557	0.9662	0.9445	**06test**	0.7767	0.9569	0.9383
07test	0.7916	0.9587	0.9439	**07test**	0.8098	0.9488	0.9364
08test	0.7715	0.9628	0.9396	**08test**	0.7902	0.9556	0.9355
22test	0.8014	0.9556	0.9419	**22test**	0.8169	0.9473	0.9357
23test	0.7759	0.9552	0.9403	**23test**	0.7935	0.9463	0.9337
25test	0.8491	0.9698	0.9599	**25test**	0.8670	0.9647	0.9567
26test	0.8363	0.9602	0.9479	**26test**	0.8496	0.9527	0.9424
30test	0.7212	0.9595	0.9356	**30test**	0.7460	0.9509	0.9303
34test	0.8158	0.9652	0.9516	**34test**	0.8326	0.9580	0.9466
35test	0.8202	0.9599	0.9484	**35test**	0.8387	0.9505	0.9413
39test	0.6674	0.9640	0.9312	**39test**	0.6961	0.9572	0.9284
41test	0.7918	0.9623	0.9460	**41test**	0.8094	0.9542	0.9403
49test	0.7628	0.9698	0.9531	**49test**	0.7852	0.9638	0.9494
92test	0.8187	0.9512	0.9399	**92test**	0.8297	0.9423	0.9327
95test	0.7249	0.9604	0.9357	**95test**	0.7828	0.9433	0.9293
99test	0.7150	0.9736	0.9480	**99test**	0.7378	0.9671	0.9443
102test	0.6973	0.9838	0.9558	**102test**	0.7283	0.9794	0.9549
109test	0.7212	0.9647	0.9388	**109test**	0.7461	0.9581	0.9356
Average	0.7678	0.9636	0.9447	**Average**	0.7901	0.9556	0.9397

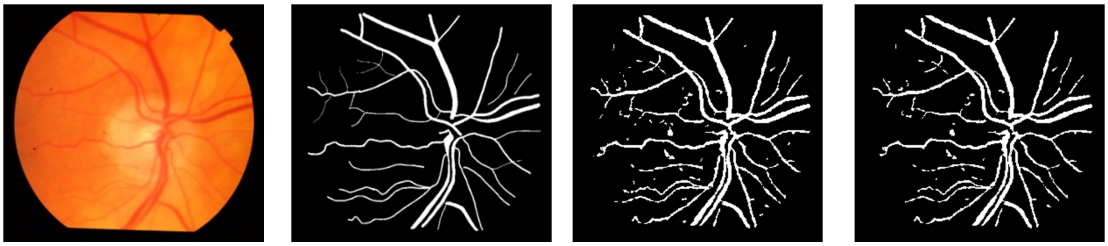

(a) (b) (c) (d)

Figure 5.11 The examples of segmentation on a MREH image using different training regimes. (a) is an original test image; (b) demonstrates the ground truth; (c) is the segmentation result using STARE textons and (d) is the segmentation result using textons trained from subset of MREH database.

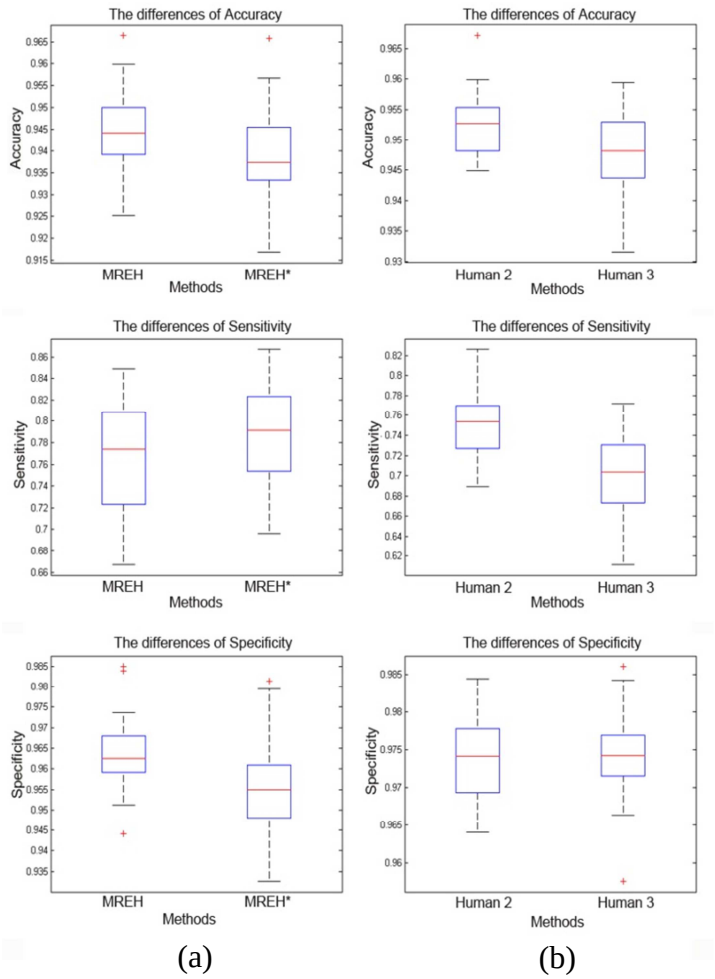

(a) (b)

Figure 5.12 (a) The box plots of measurements of two classifiers trained on MREH (MREH) and STARE (MREH*); (b) Comparative performance of two experts.

5.4 Chapter conclusion and discussion

Three sets of experiments have been described in this chapter. The first set of experiments demonstrated a supervised retinal vessel segmentation method using a novel MR11 filter bank and textons. The performance measurements on the DRIVE database shows that for k=2, the average specificity reaches 0.9806 with 0.7325 sensitivity, the average accuracy is 0.9587. The values of specificity, sensitivity and accuracy for the k=4 are 0.9524, 0.8323, 0.9422, respectively. The second set of experiments described an improved texton generation scheme based on the previous experiments, which improves the efficiency and is more automated than our previous method. The evaluation results suggest that our proposed method outperforms many published works and the performance compares well with the best published results on STARE and DRIVE datasets. For our segmentations of the STARE dataset, the average specificity = 0.9643, sensitivity = 0.7515 and accuracy = 0.9506. Specificity, sensitivity and accuracy for the DRIVE dataset are 0.9831, 0.7167, and 0.9591 respectively. The third set of experiments provided sufficient evidence which verifies that textons trained on one dataset can be reused on other datasets, while our analysis also revealed the consistent performance of our proposed method when applying it on an independent set of optical fundus images. Besides using publicly available STARE and DRIVE database, a new independent dataset named MREH was employed to test our technique. As expected, we found that textons trained on images drawn from the same dataset as the test sample perform better. However, the performance we measured when training images were drawn from a different dataset was only marginally poorer and comparable to that found between human experts, faced with the same task.

In practice, although the experimental results suggest that the textons are successfully capturing vessel texture and the framework for learning and selecting textons is robust, the high (11) dimensional feature vector causes high computational cost which still remains a problem in practical application. Moreover, some blood arterioles, venules and capillaries are miss-detected because of limited scales of spatial domain filters. A straight forward way to handle this issue is increasing the number of scales that may cover more vessel diameters. However it will again increase the computational cost. Therefore we believe that this contradiction cannot be resolved using this proposal. An alternative solution is introducing the Gabor filter to analyse the image in both the spatial and frequency domain. Our subsequent studies using the Gabor filter for retinal vessel feature extraction and

segmentation are presented in the next chapter. In addition, the statistical analysis results in our experiment shows that the performance of two expert's segmentations have statistically significant difference, which is some cause for concern and suggests that our approach may benefit from techniques for identifying ground truth that compensate for this inter observer variability [199]. We believe there is scope for further work focused on producing reliable ground truth from multiple experts, and we hope the comparative study undertaken with human experts will inform future clinical investment in this area.

Chapter 6

6. Texton based retinal vessel segmentation using Gabor filters and derivative of SIFT

Retinal vessel segmentation is an important preliminary stage in automatic assessment of retinopathy as it enables the vascular tree to be constructed. Numerous automatic retinal vessel segmentation approaches on fundus image have been proposed. A Comprehensive survey of these methods was presented in chapter 2. A significant number of filter-based methods are proposed to extract vessel and non-vessel features. The achievement of filter-based methods depends on the design of the filter bank used to extract vessel features. However these approaches that rely on special filters suffer due to the large range of various vessel widths that occur in fundus images and a common problem is that some tiny vessels are miss-segmented. Although our proposed MR11 filter bank can address some of these limitations (see section 5.1.1 for details), the technique is computationally expensive since many filter kernels need to be convolved with the image and the features that are formed are high dimensional vectors and this, in turn increases the computational cost of subsequent clustering or classifying algorithms.

The first experiment presented in this chapter investigates if we can balance this situation by decreasing the number of filters while maintaining or improving the segmentation performance. Our technique uses the Gabor filter to extract vessel relative features.

In practice, although supervised segmentation methods exhibit more competitive performance than unsupervised methods (refer to table 2.8, 2.9), pursuing more automatic (unsupervised) retinal vessel segmentation method has still been a focus of research in the area, especially, for those classifier-based segmentation methods. Unsupervised training schemes commonly do not rely on the ground truth and this is an attractive feature as in reality it may not be reliably provided. Building on texton theory and given that the vessel structure can be decomposed into many vessel segments rotated in any specific angle, we develop a derivative of the scale invariant feature transform (SIFT) [202] based on Gabor filters to extract specific vessel relative features.

In the second experiment, we propose an unsupervised retinal vessel segmentation method, in which, a derivative of the scale invariant feature transform (DSIFT) algorithm extracts vessel features that are used to determine appropriate scale parameters and potential interesting key-points which are further employed to inform the initialization of a *k*-means algorithm in the texton generation stage. The use of stable vessel key points derived from DSIFT improves the stability of the clustering algorithm and this enables textons to be selected automatically without manual intervention.

These two sets of experiments are described in section 6.1 and 6.2 respectively. The segmentation results for each experiment were measured, and corresponding evaluation results are presented in subsection 6.1.3 and 6.2.3. Section 6.3 presents the chapter conclusion and discussion.

6.1 Retinal vessel segmentation using Gabor filter and Textons

The Gabor filter was originally proposed by Dennis Gabor [180] and subsequently used by Daugman [181] to model specific frequencies and orientations of certain cells in the visual cortex of some mammals. Because of its characteristics, the Gabor filters have been widely used in many applications of image processing, such as object recognition, edge detection, and texture classification. Since the Gabor filter is localised, spatially different image textures can be extracted depending on values of the filter parameters. In this experiment, we choose the Gabor filter kernel considering the vessels' morphological characteristics, of which the most important vascular properties are vessel width and their corresponding rotated angle. We present a procedure for parameter selection based on the retinal vessel features, and use a further parameter λ to control the function's performance. Machine learning is used to optimize the filter parameters for retinal vessel extraction. The filter responses are represented as textons and this allows the corresponding membership functions to be used as the framework for learning vessel and non-vessel classes. Then, vessel texton memberships are used to generate segmentation results.

6.1.1 Optimization of Gabor filter parameters

We choose a Gabor filter kernel to extract features of retinal vessels as the function encodes information about specific frequencies and orientations. The mathematical expressions of the 1-D function and 2-D function have been presented in section 3.2.5. In order to allow the

filter kernel to be rotated in any orientation, the equation 3.23 is converted to following equation:

$$G_\theta(x,y) = e^{-\frac{1}{2}(\frac{x'^2}{\sigma_x}+\frac{y'^2}{\sigma_y})}\cos(2\pi f x' + \varphi) \qquad (6.1)$$

where $x' = x\cos\theta + y\sin\theta$, $y' = -x\sin\theta + y\cos\theta$. σ_x and σ_y determine the spread of the Gaussian envelope in x and y axis directions, respectively. We set the term σ_x equals to σ_y in our experiment. The term f denotes the spatial frequency of the Gabor filter kernel. We introduce the parameter λ which presents the wavelength of the cosine factor ($\cos(2\pi\frac{x'}{\lambda}+\varphi)$, see equation 6.2) of the Gabor filter kernel and the 1/ λ denotes the special frequency of the cosine factor (see f in equation 6.1). Because the linear structure (vessel segment) has an approximate rectangular shape, the kernel should be anisotropic. In order to construct an anisotropic kernel we insert the spatial aspect ratio parameter γ into the equation 6.1, which determines the ellipticity of Gabor Kernel. Consequently, equation 6.1 can be converted into the following form:

$$G_{\lambda,\theta,\varphi,\sigma,\gamma}(x,y) = e^{(-\frac{x'^2+\gamma^2y'^2}{2\sigma^2})}\cos(2\pi\frac{x'}{\lambda}+\varphi) \qquad (6.2)$$

$$x' = x\cos\theta + y\sin\theta$$

$$y' = -x\sin\theta + y\cos\theta$$

If γ=1, the kernel is circular and σ is the standard deviation of the Gaussian envelope.

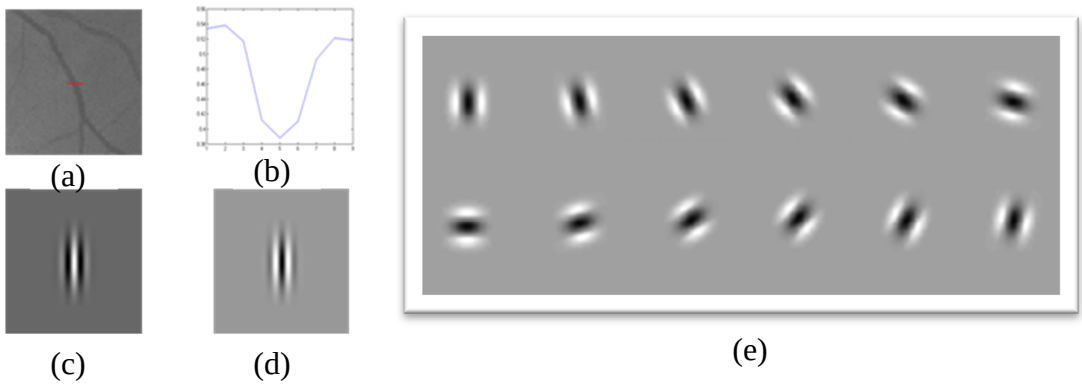

Figure 6.1 Showing the characteristics of vessel boundaries, the symmetric Gabor kernel and the optimal Gabor filter bank; (a) is a panel cropped from a grey-level retinal image; (b) a grey level profile from the red line crossing the vessel in (a); (c) Gabor kernel with parameter φ=0; (d) Gabor kernel with parameter φ= π; (e) is optimized Gabor filter bank for retinal vessel feature extraction.

Because the vessel boundaries in fundus images are presented in a plane approximately normal to the sensor plane their edges are assumed to be parallel. So we model the vessel as an even symmetric function with corresponding *centre-on* and *centre-off* responses given by $\varphi = 0$ and $\varphi = \pi$. When φ equals $\frac{\pi}{2}$ or $-\frac{\pi}{2}$, the equation becomes an odd-symmetric function. Figure 6.1-c and 6.1-d illustrate Gabor kernels with parameter $\varphi = 0$ and $\varphi = \pi$, respectively. Since retinal vessels appear darker compared with their background (e.g. Figure 6.1-a is a panel cropped from a grey-level retinal image and 6.1-b is a grey level profile from the red line crossing the vessel in 6.1-a), we choose $\varphi = \pi$ for our kernel model.

Neurophysiological research shows that the parameter λ and σ are not independent [200], Petkov and Kruizinga [201] reported that the ratio σ/λ is related to the half-response spatial frequency bandwidth *b* and can be set as follows.

$$\frac{\sigma}{\lambda} = \frac{1}{\pi}\sqrt{\frac{\ln 2}{2}}.\frac{2^b+1}{2^b-1} \qquad (6.3)$$

In practice, the bandwidth *b* controls the number of visible parallel excitatory and inhibitory stripe zones. Three zones, one inhibitory and two excitatory are visible in the retinal vessel structure (Figure 6.1-a) so we determined *b*=3 in our experiment. We set the spatial aspect ratio γ as 0.85 as our previous work suggests this ratio to be optimal. Since σ and λ are correlated, only one of them (λ) is considered a free parameter. Hence, we rewrite equation 6.2 as

$$G_{\lambda,\theta}(x,y) = e^{\left(-\frac{x'^2+0.72y'^2}{0.12\cdot\lambda^2}\right)}\cos\left(2\pi\frac{x'}{\lambda}+\pi\right) \qquad (6.4)$$

The orientation of the retinal vessel is another significant structural characteristic since vessels are neither vertical nor horizontal precisely. Consequently, the Gabor filter kernels are designed to cover 12 different orientations in 15^o increments. Hence, our filter bank comprises a set of Gabor kernels parameterised by λ which can control the function's performance with respect to the enhancement of vessels. The choice of λ, and hence using the relationship in equation 6.3, the kernel size σ is of primary importance with regard to the performance of the Gabor filter and its ability to extract vessels. We choose λ by plotting a family of ROC curves for a range of filter responses obtained from a training set of images.

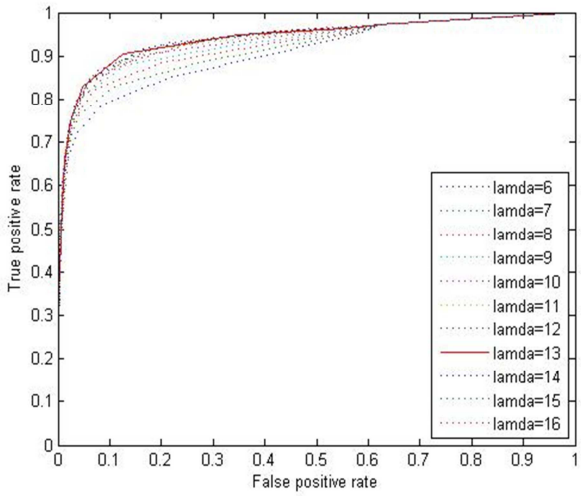

Figure 6.2 The ROC curves obtained by different lambda values.

Typical results are plotted in Figure 6.2. Corresponding qualitative measurements AUCs (area under the curves) were obtained based on the selection of λ values (6-16).

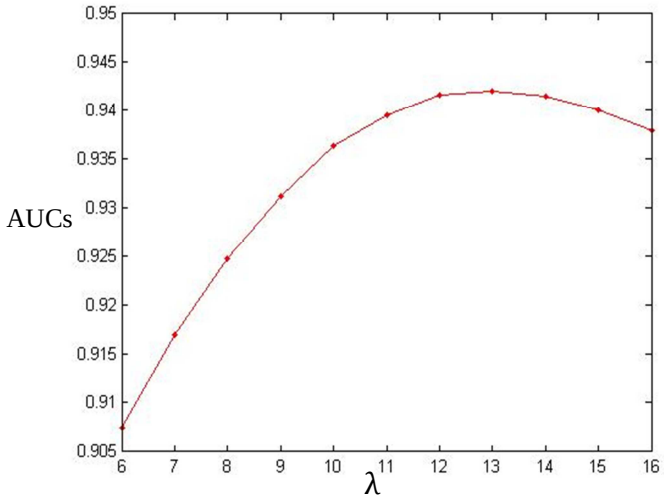

Figure 6.3 The AUCs of ROCs with different lambdas

As we can see from the Figure 6.3, when λ is 13, the value of AUC reaches maxima (0.9421), the remaining values of AUCs are 0.9074, 0.9170, 0.9248, 0.9312, 0.9364, 0.9395, 0.9417, 0.9415, 0.9401 and 0.9379, respectively. From this analysis we chose λ=13. Using equation 6.3, we find σ is 3.12 and hence a suitable kernel size is 9×9. Figure 6.1-e illustrates optimized Gabor filter bank for retinal vessel feature extraction.

To assess the performance of the Gabor filter bank we designed, we compare Gabor filter with matched filter using ROC curves. Figure 6.4 illustrates both curves, in which the curve shown with the solid line represents the performance of our Gabor filter and the curve shown with a dotted line represents the matched filter. The results indicate that the Gabor filter outperforms the matched filter, since the Gabor filter curve is closer to the top left corner.

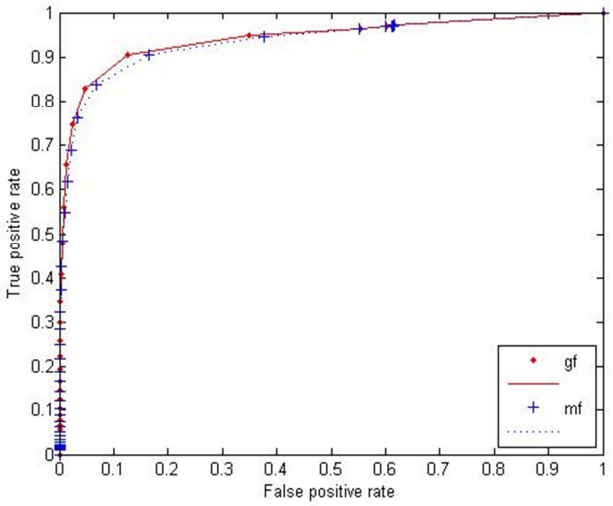

Figure 6.4 Comparative ROCs between Gabor filter and Matched filter

A typical example image response to Gabor filer bank with optimized parameter is illustrated in figure 6.5, in which 6.5(a) is an original fundus image and the 6.5(b) is the filter response.

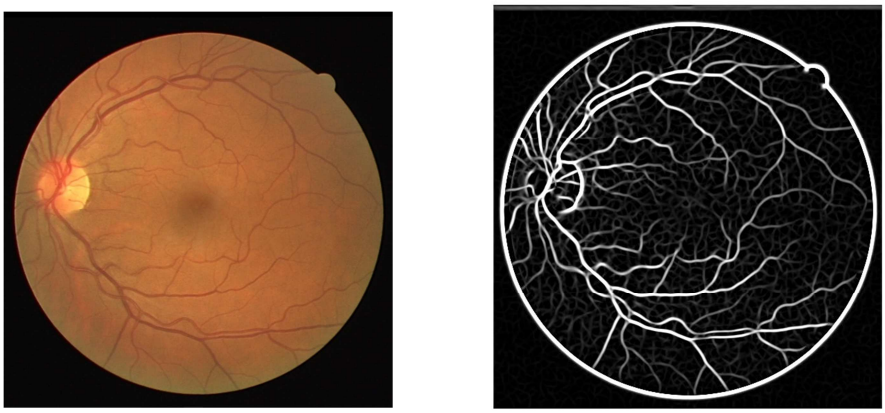

(a) (b)

Figure 6.5 An example of optimal Gabor filter response, (a) is an original fundus image and (b) is the filter response to optimized Gabor filter.

6.1.2 Generating the textons

The procedure for generating textons is similar to the scheme described in section 5.1.2. In this experiment, we search for an optimal value for parameter k of the k-means clustering procedure. When training vessel textons , various values of k (number of cluster centres) were chosen (k = 1…5) and when training non-vessel textons k= (1…10) were chosen. The corresponding accuracies were calculated by evaluating with respect to ground truth. Consequently, a total of 12 textons were generated and stored in the texton dictionary, in which 3 textons are related to vessel elements and 9 textons are related to non-vessel elements.

6.1.3 Experimental results and evaluation

In this experiment, the proposed method was tested and evaluated on the DRIVE data sets. Our algorithm was evaluated using standard measurements, in terms of sensitivity, specificity and accuracy for each sample of test images. Table 6.1 illustrates these measurements for each case in the test set of the DRIVE database, in which the average specificity reaches 0.9602 with 0.7673 sensitivity and the average accuracy is 0.9430. An example of a segmentation for an image in the test set of the DRIVE database is illustrated in Figure 6.6, in which the 6.6 (a) is an original image, the 6.6 (b) is its ground truth and 6.6(c) is the vessel segmentation. Visually, most of tiny vessel braches (capillaries) are detected. However some false positive pixels are evident in the area at the right bottom corner and around the optic disc (OD).

To verify the performance of our method, we compare results with other state-of-the-art approaches for retinal vessel segmentation in fundus images. Table 6.2 presents corresponding results. The relative terms of measurement are average obtained from all of the test images.

The experimental results show that our proposed method produced a much better figure for sensitivity, whilst maintaining almost the same overall accuracy, compared with the best other methods. Note: Comparative results include work by Soares [103] and Fraz [110] who also use Gabor filters.

Table 6-1 Performance results on the DRIVE database using the optimized Gabor filter

Image DRIVE	Sensitivity	Specificity	Accuracy
01test	0.8499	0.9564	0.9469
02test	0.7351	0.9739	0.9495
03test	0.6680	0.9714	0.9411
04test	0.7618	0.9562	0.9383
05test	0.6631	0.9864	0.9561
06test	0.7060	0.9743	0.9481
07test	0.7524	0.9459	0.9282
08test	0.7101	0.9551	0.9340
09test	0.7216	0.9744	0.9539
10test	0.7493	0.9694	0.9513
11test	0.7561	0.9494	0.9321
12test	0.7827	0.9560	0.9410
13test	0.7542	0.9572	0.9373
14test	0.8073	0.9427	0.9317
15test	0.8250	0.9322	0.9245
16test	0.8092	0.9626	0.9488
17test	0.7808	0.9511	0.9367
18test	0.8340	0.9559	0.9462
19test	0.8636	0.9649	0.9565
20test	0.8159	0.9679	0.9568
Average	0.7673	0.9602	0.9430

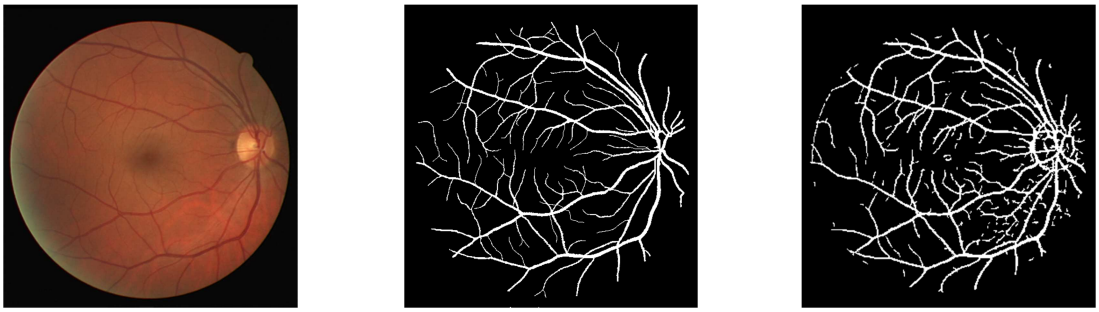

(a) (b) (c)

Figure 6.6 Examples of segmentation on a DRIVE image using optimized Gabor filter. (a) is an original image, (b) is its ground truth and (c) is the vessel segmentation

In practice, it's difficult to balance the sensitivity and specificity. Normally, with increasing sensitivity, the value of specificity might reduce and this, in turn changes the overall accuracy. In our experiment, we found that sensitivity increased more than 5% however the specificity just reduced 1%. This performance confirms the robustness of our method in detecting retinal vessels.

Table 6-2 Comparative results on the DRIVE database

Method	**Performance Results**			
	database	***Sensitivity***	***Specificity***	***Accuracy***
2nd observer	DRIVE	0.7761	0.9725	0.9473
Our method(Gabor)	**DRIVE**	**0.7673**	**0.9602**	**0.9430**
Our method(MR11)	DRIVE	0.7167	0.9831	0.9591
Mendonca [126]	DRIVE	0.7344	0.9764	0.9452
Zana[125]	DRIVE	0.6696	0.9769	0.9377
Staal [102]	DRIVE	0.7194	0.9773	0.9441
Zhang [89]	DRIVE	0.7120	0.9724	0.9382
Soares [103]	DRIVE	0.7283	0.9788	0.9466
Fraz [110]	DRIVE	0.7525	0.9722	0.9476

Table 6.2 also includes the measurements of method using MR11 (expressed as our method (MR11)) which has been described in chapter 5. Comparing with the experimental results of chapter 5, the performance of our method using Gabor in terms of accuracy is poorer than the performance of the method using MR11, however the former is much more effective, as the dimensions of feature vectors are reduced and the computational cost is lower. In the next experiment, we will investigate how to improve its performance by adopting multi-scale Gabor filters and propose an unsupervised texton based segmentation method using a derivative of SIFT.

6.2 Unsupervised texton based retinal vessel segmentation using DSIFT and the multi-scale Gabor filter

Although supervised segmentation methods are more competitive in terms of performance than unsupervised approaches, their dependence on ground-truth requires a training stage and the problem of intra- and inter-observer variability amongst experts needs to be considered as in practice this limits the robustness of the application [199]. In this and many other research fields, the availability of ground truth may be sparse or very expensive to acquire due to the laborious nature of the task. Even when a suitable image database with corresponding ground truth is available, inaccuracies in the segmentation will lead to poor performance compared to ground truth. Moreover, because a significant number of supervised vessel segmentation methods use filter banks to extract vessel and non-vessel features, the performance depends on the design of the filter bank. However they are computationally expensive since many filter kernels need to be convolved with the image and the features that are formed are high

dimensional vectors and this, in turn increases the computational cost of subsequent clustering or classifying algorithms. In this case, it's very significant to develop an unsupervised method using a limited number of filters to handle this issue, especially in the retinal vessel segmentation research field.

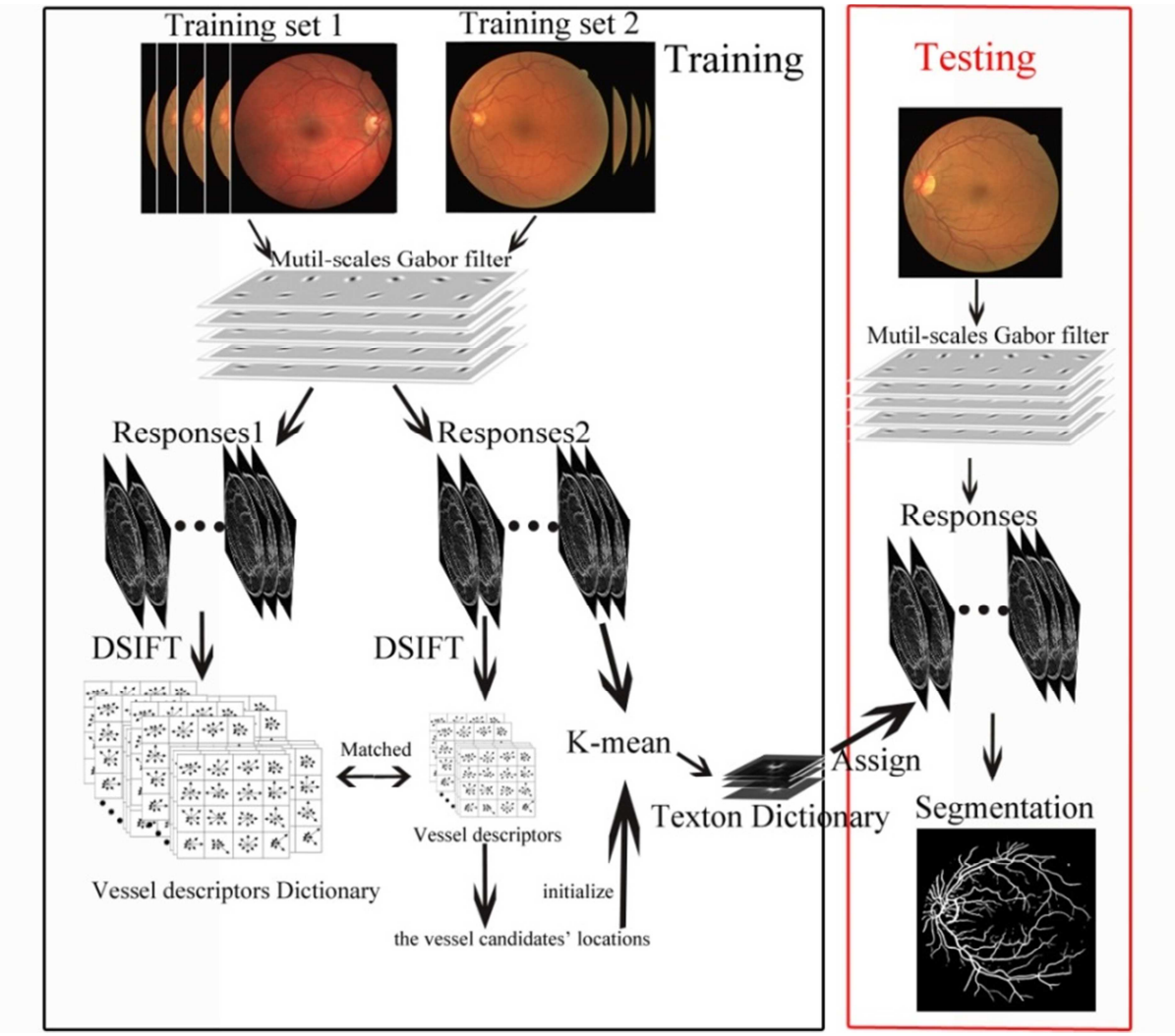

Figure 6.7 The framework of an unsupervised retinal vessel segmentation on fundus image using multi-scale Gabor filters and DSIFT

Recalling the schemes of previous methods presented in section 6.1 and chapter 5, ground truth is used to determine the vessel or non-vessel related textons when training appropriate classifiers for vessel segmentation. In this experiment, we wish to develop a new algorithm to identify the vessel textons directly instead of using ground truth. We adopted the Gabor filters presented in the previous section to detect potentially interesting pixels that will be

used to extract the specific vessel feature around those individual candidates based on an algorithm derived from SIFT. We call this algorithm the derivative of SIFT (DSIFT) algorithm. The feature descriptors derived from extracted features then can be used as indicators to identify the vessel relative elements on the fundus image. Consequently, the clustering computation procedure is seeded from those identified vessel elements to generate vessel textons that are subsequently used for segmentation in the testing stage.

The framework of this procedure is illustrated in Figure 6.7. It is split into two primary stages: training and testing. The training set is drawn from the DRIVE database and includes 20 images. We further split these images into two subsets, of which one was used for training a dictionary of vessel relative descriptors by employing DSIFT (section 6.2.1) and the other was used to train a dictionary of vessel textons as described in section 6.2.2.

At the textons training stage, the selection of appropriate Gabor filter scales is determined by scales of key points. This in turn allows textons to be formed at specific scales. We call these meta-textons (see section 6.2.2). The vessel feature descriptors were computed on each pixel of potential interest (key points), and then these generated descriptors are matched to those pre-trained vessel feature descriptors. Seeds for initializing the k-means algorithm were selected from the matched vessel key points. This determines the trained textons relating to vessel. At the test stage, meta-textons are assigned depending on responses of multi-scale Gabor filters. The selection of filter scales is informed automatically by scale information in meta-textons. The vessel texton related memberships generate texton maps and the segmentation results are obtained by combining vessel texton related maps.

6.2.1 Derivative of SIFT

The scale invariant feature transform (SIFT) was originally proposed by Lowe [202], a brief review of SIFT has been presented in section 3.3.2. SIFT is used to extract distinctive local image features that has been employed as a powerful tool for various image processing applications. Computing the SIFT involves four stages, see section 3.3.2 for details. In our experiment, inspired by Lowe's work, we developed an approach called derivative of SIFT (DIFT). Our approach uses Gabor filter to model the distinctive vessel features. The detail of the Gabor filter characterised by a free parameter λ is presented in section 6.1.1.

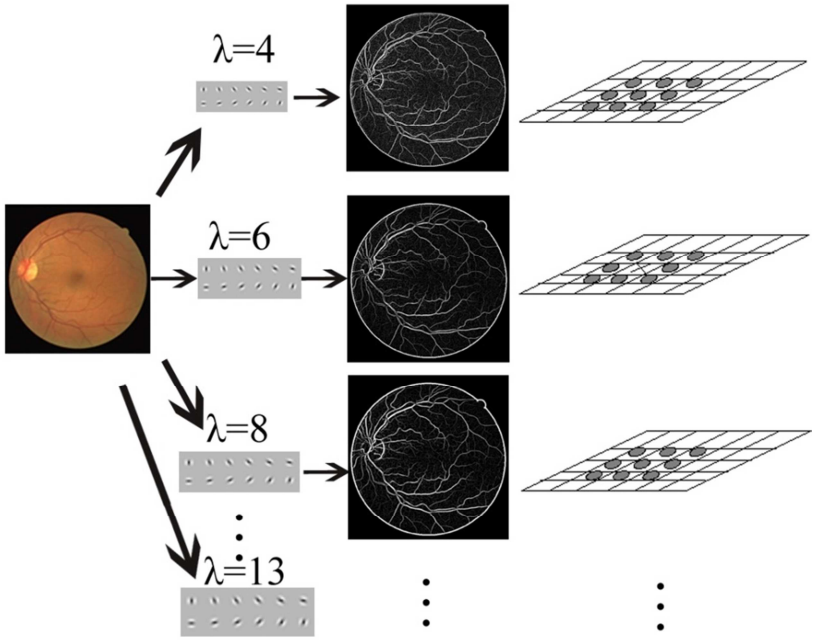

Figure 6.8 Vessel features extraction and key points selection in DSIFT

Given a significant natural characteristic of retinal vessels is the wide range of vascular widths presented in fundus images (see Figure 2.1), applying a filter bank using only a single scale may not be sufficient to detect various widths of vessels exactly. So although applying the filter at an optimal scale may provide good performance with regard to extraction of the main vessels, some tiny vessels may be miss-detected. However, using Gabor filters at each scale have their advantages and disadvantages. As we described in section 6.1.1, the value of lambda (λ) determines the value of sigma (σ), see equation 6.3. The value of σ determines the kernel size, thus different widths of vessels can be detected using various σ. In practice, while small values of σ (scale) are useful for detecting tiny vessels, they are also sensitive to image noise. With increasing value of σ, the filter may detect wider vessels, however, those tiny vessels may be miss-detected. With this in mind, in order to detect potential vessel key points which are further analysed to generate corresponding descriptors, we adopted Gabor filters at multiple scales in our experiment. Note: based on our earlier work we select the range of scales empirically i.e. $\lambda \in [4, 6, 8, 9, 13, 15]$.

Although the descriptors could be calculated for each pixel in the image, to reduce the computational cost, descriptors are only computed for a subset of the most representative vessel pixels. These so-called vessel key points were obtained by comparing the filter-bank response at a pixel (marked as cross in Figure 6.8) to its 8 neighbours (marked as circles) at the same scale and meanwhile comparing the pixel to its 18 neighbours at its adjacent scales.

The selection of the local maxima, inspired by SIFT, aims to identify a set of representative vessel pixel candidates, therefor the local minima were not taken into account.

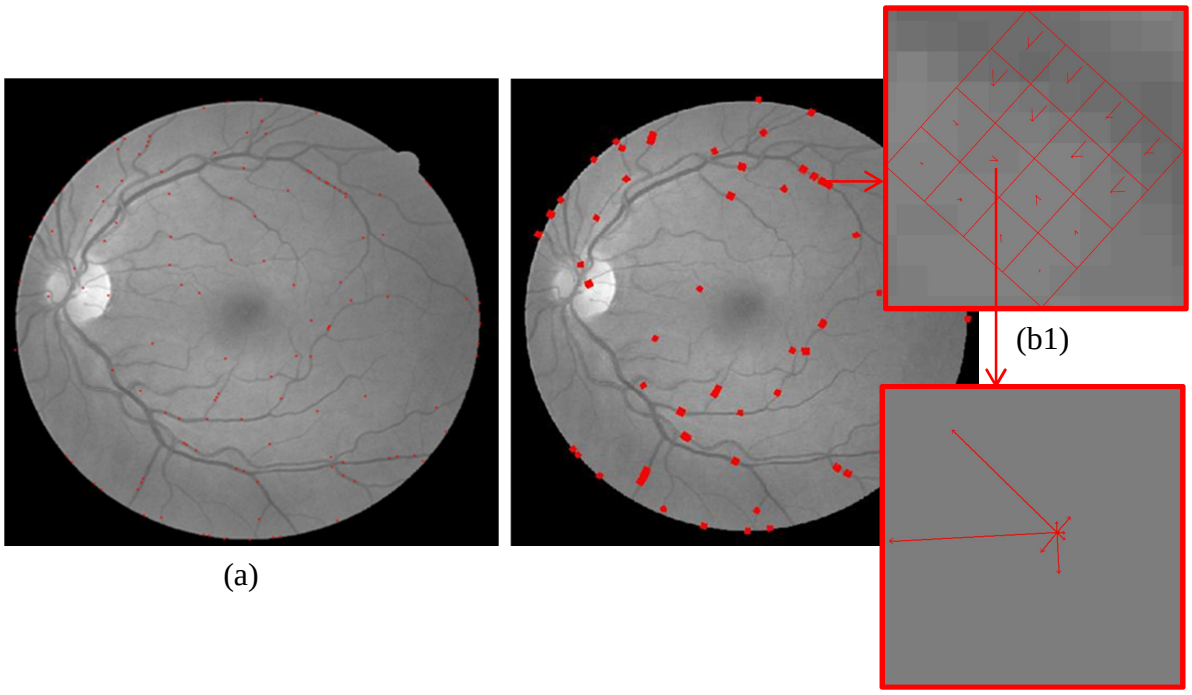

Figure 6.9 Examples of detected key points of vessels and corresponding descriptors. (a) illustrates the key points and (b) illustrates corresponding descriptors. One of the descriptors is zoomed in and presented in (b1); one of the orientation histograms presented in (b1) is illustrated in (b2).

Figure 6.9 (a) illustrates the potential key points. As we can see from the image, key points correspond not only to main vessels, but also a few key points are located in the areas around the end of some capillaries. This is because we apply the Gabor filter at multiple scales and each scale has a corresponding ability to extract various sizes of vessels. For instance, assuming λ equals 4, 6, and 8, the filter with λ=4 has an ability to extract thin vessels thus the responses of capillaries are evident. The filter with λ =8 has valid performance for detecting wide vessel however the responses of tiny vessels may not be evident. The performance of filter with λ=6 is intermediate between λ=4 and λ=8. In this case, these differences of responses among three scales may be detected and the maxima in both wide and thin vessels can be extracted when each pixel compares to its 26 neighbours. In the second stage, the detected maxima are used as potential vessel candidates. For each candidate, its location and corresponding scale are recorded. Note: low contrast points are removed. In the third stage, each key point is assigned to one or more orientation based on the local image

gradients around the key points. Image gradient magnitude $m(x,y)$ and corresponding orientation $\theta(x,y)$ are calculated using pixels differences at each scale. The equation can be expressed as follows:

$$m(x,y) = \sqrt{(R(x+1,y) - R(x-1,y))^2 + (R(x,y+1) - R(x,y-1))^2} \qquad (6.5)$$

$$\theta(x,y) = tan^{-1}\left(\frac{R(x+1,y)-R(x-1,y)}{R(x,y+1)-R(x,y-1)}\right) \qquad (6.6)$$

where R is the Gaussian smoothed image at a specific scale which is determined by the scale of the key points. The calculated gradient orientations are further formed as an orientation histogram which covers 360 degrees range of orientations. The computation of gradients and orientations are weighted by a Gaussian window. The different sizes of the Gaussian circular window are determined by the scales of selected key points. These scales (σ) are also inherited by the parameters of the Gaussian envelope of the Gabor function. In our experiment, the radius of the Gaussian circular window is determined by σ, where values of σ are calculated based on the parameter lambda $\lambda \in [4, 6, 8, 9, 13, 15]$, consequently, referring to equation 6.3, a range of σ values is [0.96, 1.45, 1.93, 2.17, 3.13, 3.61]. Note, here, in our experiment the appropriate scales of key points include $\lambda \in [6, 8, 9, 13]$, so the employed σ values are [1.45, 1.93, 2.17, 3.13]. Employing a circular window allows an orientation histogram to be generated within the specific region located around the vessels. At the final stage, all generated gradients and orientations are accumulated into a representation (descriptor) by summing the gradient magnitudes near that orientation in the region (see Figure 3.8). Each descriptor is formed as a 4x4 grid, of which each sub-grid contains an orientation histograms that contains 8 direction bins. An example of vessel key points' descriptors is shown in the Figure 6.9 (b). To see it clear, one of the descriptors in (b) is zoomed in and presented in (b1). The descriptor is presented as a 4×4 grid. An orientation histogram in each grid contains 8 direction bins. This histogram is presented in (b2) derived from (b1).

In our experiment, we trained vessel relative descriptors from a subset of training samples and stored them into a descriptors library. For images in the training subset which are used to generate textons, we detect key points in the same way, and apply the same scheme to generate their descriptors. Up to this point, each key point is represented by its descriptor which is formed as a 4x4x8=128 dimensional vector. The matching process is implemented by finding the best candidate match for each key point from the key point library using

corresponding descriptor. The factor to identify the best candidate is based on its nearest neighbor which is defined as the key point with minimum Euclidean distance for the invariant descriptor vector. In the original SIFT algorithm, the second-closest neighbor is defined as being the closest neighbor considering that there are multiple training images of the same object. In [202], the objects in a natural image could be any structures which are not known in advance, thus the adopted difference of Gaussian filter in the feature extraction stage is not designed for a particular object (e.g. a cup, a car or a house etc.). This results in some features from an image may have incorrect match in the training database because they may arise from background cluster or were miss detected in the training images. Instead, in our experiment, the object of interest (vessel) is known explicitly that motivates us to design a specific Gabor filter bank (see section 6.1.1) to detect vessel features. Therefore at the key point detection stage, the detected key points and corresponding calculated descriptors are completely relevant to the vessels. In an extreme condition, we can even use all of detected key points derived from a novel image without matching process. However, in order to use the most representative candidates to initialize the clustering process, detect key points were matched according to the minimum Euclidean distance between the novel descriptors and the descriptors stored in descriptors library following by a global distance thresholding procedure. The matched key points are used in the next stage to identify seed candidates which are subsequently used to initialise the clustering algorithm when generating textons (Figure 6.7). We will describe texton based vessel segmentation using the multi-scale Gabor filter in the next subsection.

6.2.2 Textons generation and segmentation

Textons are learnt from the responses of multi-scale Gabor filters which are applied to each image in the training set. Here, the scales used are derived from the scales of which contain the matched key points, found during training. The combined filters can extract both tiny and wide vessel features and this results in more accurate segmentation. The *k*-means algorithm is informed by key points, in which, initially, instead of selecting *k* random points as default means (centroids) as we did in the previous scheme (see Figure 5.4), initial pixels are selected from matched vessel key points as initial candidates, then the new means of pixels located in the areas of the remaining matched key-points are computed in preference to other pixel candidates in the image. This computing procedure not only improves the stability of the *k*-means algorithm, but also allows the clustering procedure to start from more salient

vessel elements and has the advantage that the vessel texton dictionary can be constructed without the assistance of ground truth.

In our experiment, we chose *k*=5 to reflect significant classes of objects that are visible in the images, i.e. vessels, bifurcations, optic disc (OD), vessel reflection, and background. To determine texton classes, we first rank the clusters based on their size. The largest cluster in the list maps onto the background texton class, since the background has the most number of pixels in an image. The remaining clusters are considered as textons that relate to vessels.

In the texton training stage, only those Gabor filters at more appropriate scales are employed to extract vessel features. The scales are determined by the scales of detected key points which are generated using the DSIFT algorithm. We store generated textons and corresponding scales (in our experiment, these scales are λ=6, 8, 9, 13) into a texton dictionary which can be used in the test stage. Each texton in the dictionary is formed as a 4-dimensional vector which is indexed by the corresponding scale. This scale information is stored in the first column of texton dictionary matrix, and the remaining rows record clustering centroids according to corresponding scales. We call it meta-textons. In our experiment, five meta-textons are trained, therefore, a total 5×4 numbers of clustering centroids are composed in the dictionary. Table 6.3 illustrated a schematic matrix of the meta-textons which is trained from the training set in the DRIVE database. The first column of the matrix shows the scale information. Each grid in the rest matrix contains a clustering mean value related to each texton ID [1,…, 5].

Table 6-3 A schematic diagram of the meta-texton trained from the DRIVE database

Scales\Id	1	2	3	4	5
6	0.180189	2.612138	1.371923	10.78716	4.293368
8	0.198127	1.455655	1.28509	9.580782	3.988796
9	0.155359	5.88564	1.561048	11.87148	4.670367
13	0.170376	11.3539	2.054979	10.70356	4.549439

In the test phase, we filter each novel image with the texton filter bank to generate corresponding responses at each pixel, where firstly, scales are selected by loading the meta-textons and reading its scales. In this case, the novel image doesn't need to convolve with

filter at all pre-defined scales (e.g. $\lambda \in [4, 6, 8, 9, 13, 15]$), therefore reducing the computational cost of the system. Then corresponding vessel textons relating to selected scales are assigned based on the filter responses. The memberships of each texton are calculated that from the corresponding textons maps, segmentation results are obtained by combining various vessel texton maps.

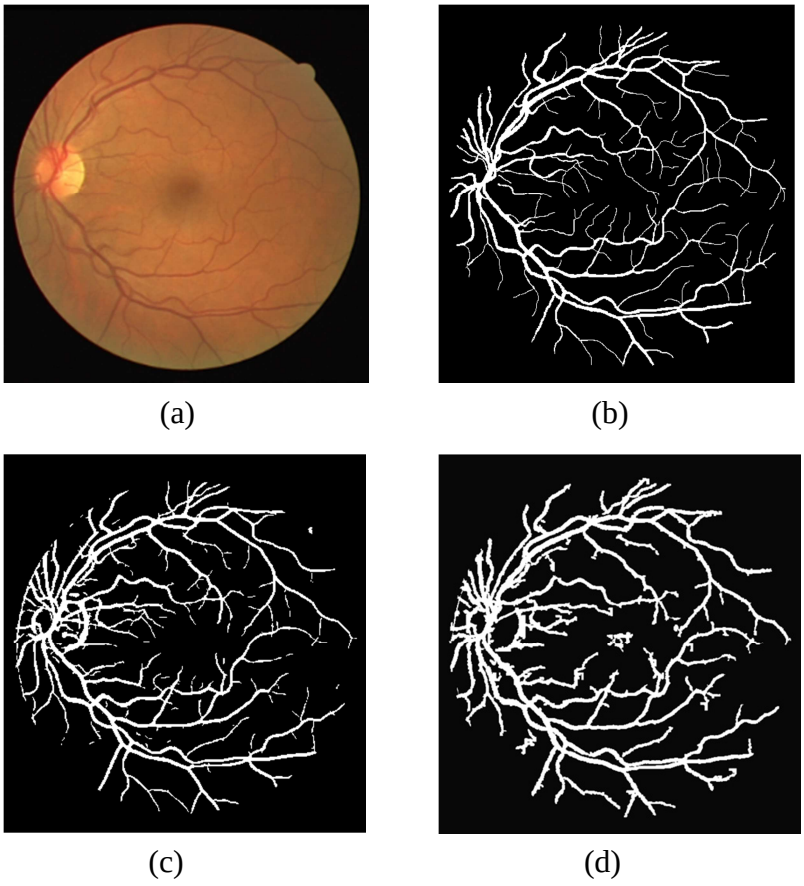

(a) (b)

(c) (d)

Figure 6.10 More accurate diameters of veins, arteries and capillaries in segmentation results using multi-scale Gabor filter. (a) is an original fundus image, (b) is its ground truth (c) is the vessel segmentation using our method and (d) is the segmentation using Cinsdikici [88] method

The advantages of adopting multi-scale Gabor filters is that it provides useful functions for the algorithm, in which the tiny and wide vessels can be distinguished, thus the detected diameters of vessels are more accurate. For instance, a segmentation result using a state-of-the-art method present in published work [88] is shown in figure 6.10-d. The result shows the diameters of the tiniest vessels are wider than the actual diameters in the corresponding

ground truth (Figure 6.10-b). In contrast, the vessel segmentation using multi-scale Gabor filters (Figure 6.10-c) produced much better results than results presented in Figure 6.10 -d.

We hope to emphasize that the diameter of segmented vessels is a significant property for automated detection of corresponding diseases. For instance, in reality, a decreased ratio between diameters of arteries to those of veins also known as A/V ratio is used to assess the risk of hypertension (see section 1.3 for more details).

6.2.3 Experimental results and evaluation

The proposed method was tested and evaluated on the DRIVE data sets. Each image in the test set of the DRIVE database was segmented. The segmentation examples are shown in Figure 6.10 -c and Figure 6.11-a2, -b2. We can see from these results that our method extracts veins and arties (vessels with wide diameter) accurately while many capillaries (tiny vessels) are segmented. Note: many tiny vessels at the end of vessel network are detected, in which the diameter of those vessels are close to the real width of vessels (shown in ground truth). In order to qualify the performance of the proposed method, each segmentation result was compared to its ground truth. Standard metrics (sensitivity, specificity and accuracy) were employed to measure the performance. Table 6-4 illustrates measurements of each case, the average specificity reaches 0.9668 with 0.7812 sensitivity, the average accuracy is 0.9504.

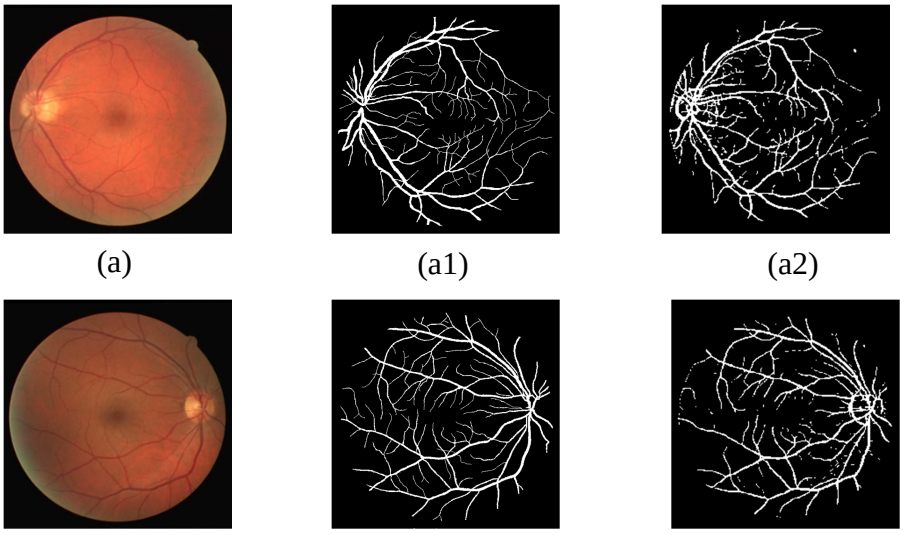

Figure 6.11 Unsupervised texton based vessel segmentation results using multi-scale Gabor filter. (a)(b) are original fundus images, their ground truths are shown in (a1)(b1), and (a2)(b2) are corresponding vessel segmentations using our method.

As we mentioned in the previous chapter, it's difficult to balance the sensitivity and specificity. The tiny vessels have extremely low contrast compared with the background, thus if the algorithm is particularly designed for extraction of tiny vessel elements in order to increase the sensitivity of segmentation, more non-vessel elements from the background may be detected as vessels. This will lead to a reduction in specificity and accuracy. In this experiment, the average sensitivity reaches 0.7812. This reveals the algorithm using DSIFT descriptors and multi-scale Gabor filters has more competitive performance for vessel extraction. The maximum sensitivity reaches 0.8833, whilst the average specificity of 0.9668. This confirms that the algorithm maintains good performance and is insensitive to features due to non-vessel elements in the background.

Table 6-4 Performance results on DRIVE database using multi-scale Gabor filter and DSIFT

Image	Sensitivity	Specificity	Accuracy
01test	0.8506	0.9670	0.9566
02test	0.7717	0.9799	0.9586
03test	0.7825	0.9513	0.9344
04test	0.8142	0.9549	0.9420
05test	0.7449	0.9800	0.9580
06test	0.7477	0.9696	0.9480
07test	0.7108	0.9750	0.9509
08test	0.7267	0.9559	0.9362
09test	0.7819	0.9676	0.9526
10test	0.8111	0.9623	0.9499
11test	0.7663	0.9640	0.9463
12test	0.7900	0.9678	0.9524
13test	0.7448	0.9707	0.9486
14test	0.8213	0.9466	0.9365
15test	0.7381	0.9810	0.9637
16test	0.7261	0.9835	0.9603
17test	0.7996	0.9519	0.9391
18test	0.7817	0.9752	0.9599
19test	**0.8833**	0.9640	0.9573
20test	0.8302	0.9676	0.9575
Average	**0.7812**	**0.9668**	**0.9504**

Our method was compared with other state-of-the-art approaches and the most recent work, sorted by published year in table 6.5. Most of methods presented in table 6.5 are supervised classifier based methods. A tracing-based method [101] and a graphic cut based method [128] are also included, as both of them are proposed very recently and have outstanding performance.

The comparative results show that our method has much better sensitivity than the best other methods. To the best of our knowledge, the maximum accuracy of previous method is 0.9595, proposed by Ricci and Perfetti [104], however they didn't report values of sensitivity and specificity. Relatively, the proposed tracing based method due to Ocbagabir et al. [101] has competitive accuracy (0.9583), the sensitivity of our method is about 7% better however the specificity is 1.5% worse. Although the lower specificity indicates that more non-vessel elements were segmented as vessels, the better sensitivity reveals that our method has better performance to detect vessels from background. In this field, the primary goal of vessel segmentation is to detect as many vessel elements as possible. Therefore we are inclined to improve the overall accuracy by pursuing higher sensitivity while maintaining the same specificity or sacrificing only a small fraction of it

Table 6-5 Comparative results between our unsupervised retinal vessel segmentation method and other state-of-the-art methods on the DRIVE database

Method	**Performance Results**				
	year	***categories***	***Sensitivity***	***Specificity***	***Accuracy***
2nd observer	-	Manual	0.7761	0.9725	0.9473
Staal [102]	2004	Supervised	0.7194	0.9773	0.9441
Soares [103]	2006	Supervised	0.7283	0.9788	0.9466
Ricci & Perfetti [104]	**2007**	Supervised	**-**	**-**	**0.9595**
Rezatofighi et al.[105]	2008	Supervised	0.7308	0.9723	0.9410
Salazar-Gonzalez[128]	2010	Graph cut	0.7197	0.9665	0.9479
Fraz [110]	2011	Supervised	0.7525	0.9722	0.9476
Marín et al. [108]	2011	Supervised	0.7067	0.9801	0.9454
Condurache & Mertins et al. [111]	2012	Supervised	0.9094	0.9591	**0.9516**
Ocbagabir et al.[101]	2013	Tracing	0.7131	0.9824	**0.9583**
Our method(Gabor)	2013	Supervised	0.7673	0.9602	0.9430
Our method (Multi-Gabor&DSIFT)	2014	Unsupervised	**0.7812**	**0.9668**	**0.9504**

We wish to emphasize that the primary goal of this experiment to develop an unsupervised method which has relatively good performance compared with supervised methods which requires ground truth. Our experimental results confirm that the texton based method using DSIFT and multi-scale Gabor filtering technique has significantly competitive performance compared to many other supervised methods.

6.3 Chapter conclusion and discussion

This chapter described two sets of experiments, in which an optimized Gabor filter for vessel feature extraction was proposed. The advantage of using this filter is that it reduces the dimension of feature vectors which will be clustered in a textons generation procedure. Thus it significantly saves the computational cost when we implement the application. The basis of a single parameter controlled Gabor filtering technique is using correlations between parameters λ and σ of the Gabor filter, in which the σ determines the spread of the Gaussian envelop of the Gabor function. This plays a significant role in determining the width of vessels. Therefore using λ determines sigma can detect more vessel features that can be used to generate corresponding textons. The experimental results revealed that performance of our Gabor filter is better than the matched filter based on the ROC analysis (see Figure 6.4). The corresponding parameters of the Gabor filter were optimized also using a ROC analysis of the filter performance on training data. Results of the first experiment demonstrated that vessel segmentation using optimized Gabor filer and textons enhances the true positive rate while maintaining a level of specificity that is comparable with other approaches.

In the second experiment, we proposed a new unsupervised retinal vessel segmentation method by developing a derivative of SIFT (DSIFT) to optimize the generation of vessel relative textons and determine more appropriate scales for extracting vessel features. In order to extract distinguishing vessel features for training vessel textons, we applied Gabor filters at multiple scales. As each scale is tuned to detect corresponding vessels with different diameters, the selection of scales was determined by the scales of selected key points, identified by DSIFT descriptors. The vessel related descriptors identified by applying DSIFT on a training set are stored in a descriptors dictionary. These trained descriptors are matched to novel descriptors generated from another set of training images used to generate textons. Textons corresponding to descriptors that most closely match descriptors in the dictionary are used as default means in a clustering process that identifies textons. The integration between the DSIFT descriptors computation and textons generation allows suitable scales to be selected automatically without manual intervention. Thus the method can be more automated and be invariant to scales. Here, the textons are formed as meta-textons which not only contains prototype responses vectors but also records corresponding appropriate scales for vessel feature extraction. The evaluation results verified that our proposed unsupervised retinal vessel segmentation have competitive performance, compared to the best other

supervised methods. Additionally, we believe that the proposed scheme for selecting potential vessel candidates based on DSIFT also can be used as a general tool to detect more appropriate initial seeds in some tracing based vessel segmentation methods.

Although the performances of both methods presented in sub-sections 6.1 and 6.2 in terms of sensitivity, specificity, and accuracy are comparable with the best published work, we can find some limitations and weaknesses from our methods. Visually, some false positive pixels appear in segmentation results, especially in areas around the optic disc (OD) and in the left part of the peripheral area. This is because the area surrounding the OD and the outer circle exhibits strong contrast and so there are significant gradient changes on its boundary. We believe that our method can be improved by removing these false positive pixels. A direct way to handle this limitation is adding a pre-processing stage to eliminate such influences. An alternative way is applying a post-processing stage on the segmentation results to remove them. We intend to address these limitations in our suggested further work.

Chapter 7

7. Conclusion and future work

In optometry, the appearance of blood vessels in the retina are routinely examined as their condition is indicative of disease, such as diabetes, hypertension, and glaucoma. However, the assessment of the retina vessel anomalies is a skilled time consuming task, and as such it has been the focus of research into automatic assessment techniques. Retinal vessel segmentation on fundus images is a critical stage in computer assisted diagnosis of systematic disease such as DR, AMD and Glaucoma etc. Measurements of vessel features also play an important role in the diagnosis of hypertension, obesity, arteriosclerosis, assessment of retinal artery occlusion and in computer-assisted laser surgery. Numerous approaches for automatic retinal vessel segmentation have been proposed. However, it is still a big challenge and remains a focus for ongoing research because of the complex nature of fundus images. The primary goal of our research is to investigate and developed accurate retinal vessel segmentation approaches in fundus images using texture feature extraction techniques and textons. This thesis presents a brief review of those diseases and also includes their current status, future trends and their automatic diagnosis techniques in routine clinical applications. The importance of retinal vessel segmentation is particularly emphasized in such applications. An extensive review of texture analysis methods that are especially useful for image segmentation is presented. Five automatic retinal vessel segmentation methods are proposed in this thesis, in which the experimental results suggested that our supervised and unsupervised texton based retinal vessel segmentation methods are more competitive than may other state-of-the-art methods.

In this thesis, the early chapters describe the motivation for the project and provide an introduction to the field, in which various forms of common diseases (e. g. Glaucoma, Age-related macular degeneration (AMD), vascular disorders, and Diabetic retinopathy) and corresponding automated detection techniques using fundus images are comprehensively reviewed. No such comprehensive review exists (as far as we’re aware) and this provides a valuable resource for those undertaking further work in the area. A comprehensive survey of

earlier and current retinal vessel segmentation methods was presented. Here, these approaches were divided into four categories: Matched filtering based segmentation; Vessel tracing/tracking based segmentation; Classifier based segmentation; and Model-based segmentation. Numerous such segmentation methods were briefly reviewed in each category and the advantages and disadvantages of methods in each category were discussed according to their corresponding comparative performance and summarized in tables 2.8 and 2.9. The classifier-based segmentation includes supervised and unsupervised methods. The advantage of supervised methods is that it provides more accurate segmentation results than other categories. However, its dependence on ground-truth requires a training stage and the problem of intra- and inter-observer variability amongst experts needs to be considered as in practice this limits the robustness of the application. Unsupervised classifier-based methods are seen to be a more appropriate way to segment the retinal vessels, but limitations (e.g. high computational costs and relatively poorer performance) need to be solved. In addition, this thesis presents an extensive review of texture analysis techniques which may be appropriate for retinal vessel segmentation. This may also provide a useful resource for medical image segmentation using various texture analysis techniques.

The later chapters of this thesis described five automatic retinal vessel segmentation methods, in which the hybrid retinal vessel segmentation method is able to eliminate the interference caused by abnormalities in fundus images. Such anomalies (e.g. drusen) are the primary factor that influences the accuracy of segmentation in this field. The novel supervised texton based retinal vessel segmentation method is proposed which employs a new spatial filter bank design (MR11) for vessel feature extraction. This method significantly improves performance in terms of accuracy and efficiency compared to many other state-of-the-art methods. This method was further developed by optimizing the texton generation stage in order to reduce the computational costs. The experimental results on two benchmark databases (DRIVE and STARE) show that our improved texton based method performs well compared to other published work and the results of human experts. On the STARE database, average specificity reaches 0.9643 with 0.7517 sensitivity and the average accuracy is 0.9506. The values of specificity, sensitivity and accuracy for the DRIVE dataset are 0.9831, 0.7167 and 0.9591, respectively. In addition, we investigate the effect of different training regimes and provide an experimental basis for training a general textons library for vessel segmentation. Given that the lack of study materials (ground truth) is an open issue in this research field, we built a new dataset (using original data supplied from Manchester Eye

Hospital) that can be used as a resource for future vessel segmentation research. The data set includes 3 sets of ground truth, hand labelled by 3 ophthalmologists.

Building on experience gained during the development of the MR11 filter bank a supervised texton based vessel segmentation method using an optimized Gabor filter was described. We showed this approach to significantly enhance the true positive rate while maintaining a level of specificity that is comparable with other approaches. Finally, a new unsupervised texton based retinal vessel segmentation method using the derivative of SIFT (DSIFT) and multi-scale Gabor filters is proposed, which achieves a level of performance comparable with other supervised state-of-the-art methods. The performance of this method on the DRIVE database, in term of average sensitivity, specificity and accuracy are 0.7812, 0.9668 and 0.9504, respectively. In this method, the textons were formed as meta-textons which contain both prototype response vectors and appropriate scale information. This unsupervised segmentation method represents a significant contribution since it addresses the problems that arise due to inconsistent ground truth labels in the database and moreover, the DSIFT algorithm can be used to initialize seeds for many other categories of retinal vessel segmentation methods (e.g. tracing based method). The computer specifications and efficiencies of our proposed methods are reported in table 7.1.

Table 7-1 Computer specifications and efficiencies of our methods

Method	Time per image	Computer specifications	OS	Software
Improved method described in chapter 4	5.45s	Inter (R) Core(TM) i7-4770,3.40 GHz, 16 GB	Windows 8 64-bit	Matlab
Supervised texton based method using MR 11 described in chapter 5	21.31s	Inter (R) Core(TM) i7-4770,3.40 GHz, 16 GB	Windows 8 64-bit	Matlab
Improved Supervised texton based method using MR11 described in chapter 5	20.78s	Inter (R) Core(TM) i7-4770,3.40 GHz, 16 GB	Windows 8 64-bit	Matlab
Supervised texton based method using multi-scales Gabor filters described in chapter 6	8.93s	Inter (R) Core(TM) i7-4770,3.40 GHz, 16 GB	Windows 8 64-bit	Matlab
Unsupervised texton based method using multi-scales Gabor filters and D-SIFT described in chapter 6	12.66s	Inter (R) Core(TM) i7-4770,3.40 GHz, 16 GB	Windows 8 64-bit	Matlab, C++

Considering some issues have not been resolved in this field, and we believe that our proposed texton-based approaches have some potential improvements. We list our further work as follows:

1. The experimental results in section 5.3 have suggested that performances of two experts segmentations are statistically significantly different, which is some cause for concern and suggests that our approach may benefit from techniques for identifying ground truth that compensate for this inter-observer variability. We believe there is scope for further work focused on producing reliable ground truth from multiple experts.

2. Considering the robustness of our texton based vessel segmentation method, we believe that our method can be extended to segment several clinical structures simultaneously in fundus images by designing a new filter bank which not only contains filters for vessel and background feature extraction but also contains specific filters to extract features from different forms of anomalies in fundus images. This may allow our texton based segmentation method to be a more operationally useful tool for commercial applications. Moreover, we also would like to extend our method for segmentation in other medical image modalities.

3. Measure the diameter and tortuosity of segmented vessels to assess the disease (e.g. hypertensive retinopathy, DR, cardiovascular disease ect.) by A/V radio and mathematical terms of tortuosity. These should also be addressed in further work.

Reference

[1] H. Schneiderman, “The Funduscopic Examination”, Website access at http://www.ncbi.nlm.nih.gov/books/NBK221/, 2013.

[2] J. J. Kanski, “Clinical Ophthalmology: A Systematic Approach”, Butterworth-Heinemann, London, U.K., 1989.

[3] B. Julesz, “Textons, the elements of texture perception, and their interactions”, *Nature*, vol.290, no. 5802, pp. 91–97, 1981.

[4] Eye Anatomy, website access at: http://www.glaucoma.org/glaucoma/anatomy-of-the-eye.php, 2013.

[5] Helga Kolb, “Gross Anatomy of the Eye”, website access at: http://webvision.med.utah.edu/book/part-i-foundations/gross-anatomy-of-the-ey/, 2013.

[6] H. R. Novotny and D. L. Alvis, “A method of photographing fluorescencein circulating blood in the human retina”, *Circulation*, vol. 24, pp. 82–86, 1961.

[7] A. Gullstrand, “Neue methoden der reflexlosen ophthalmoskopie,” *Berichte Deutsche Ophthalmologische Gesellschaft*, vol. 36, 1910.

[8] P. J. Saine and M. E. Tyler, Ophthalmic Photography: Retinal Photography, Angiography, and Electronic Imaging, 2nd Edition, Butterworth-Heinemann, Boston, 2001.

[9] M. D. Abramoff, M. K. Garvin, and M. Sonka, "Retinal Imaging and Image Analysis", IEEE Reviews in Biomedical Engineering, vol.3, pp. 169 - 208, 2010.

[10] C. B. James and L. Benjamin, Ophthalmology: Investigation and Examination Techniques, Butterworth-Heinemann, London, 2007.

[11] Mikael Häggström, “File: Fundus photograph of normal right eye.jpg”, website access at http://en.wikipedia.org/wiki/File:Fundus_photograph_of_normal_right_eye.jpg, 2013.

[12] I. Georgalas, D. Papaconstantinou, C. Koutsandrea, et al., “Angioid streaks, clinical course, complications, and current therapeutic management”, website access at: http://openi.nlm.nih.gov/detailedresult.php?img=2697526_tcrm-5-0081f2&req=4, 2013.

[13] E. Corona, S. Mitra, M.Wilson, T. Krile, and Y. H. K. P. Soliz, “Digital stereo image analyzer for generating automated 3-D measures of optic disc deformation in glaucoma.”, IEEE Transactions on Medical Imaging, vol. 21, no. 10, pp. 1244–1253, 2002.

[14] L. Abrams, I. Scott, G. Spaeth,H.Quigley, R. Varma, “Agreement among optometrists, ophthalmologists, and residents in evaluating the optic disc for glaucoma”, *Ophthalmology*, vol.101,no.10, pp.1662-1667, 1994.

[15] D. T. Cook, L. M. Cook, “A 21st Century Retinal Camera”, website access at http://guthrieeyecare.com/icare/retinalcamera/, 2013.

[16] A. L. MacLean, and A.E. Maumenee. “Hemangioma of the choroid”, *American Journal of Ophthalmology*, vol.50, pp. 3-11, 1960.

[17] H. R. Novotny and D. L. Alvis, “A method of photographing fluorescence in circulating blood in the human retina,” *Circulation*, vol. 24, pp. 82–86, 1961.

[18] Retina Consultants of HAWAII, Diagnostic tests, website access at: http://retinahi.com/for-patients/diagnostic-tests/, 2013.

[19] C.A. Girkin, Principles of confocal scanning laser ophthalmoscopy for the clinician The essential HRT primer, M. Fingeret, J.G. Flanagan, J.M. Liebmann (Eds.), Heidelberg Engineering, Germany, pp. 1–9, 2005.

[20] J. S. Wolffsohn, L. N. Davies, “Advances in Ocular Imaging”, *Expert Review of Ophthalmology*, vol.2, no. 5, pp.755-767, 2007.

[21] J. R. Zelefsky, N. Harizman, R. Mora et al., “Assessment of a race-specific normative HRT-III database to differentiate glaucomatous from normal eyes”, *J. Glaucoma*, vol. 15, pp. 548-551, 2006.

[22] P. J. Saine, M. E. Tyler. Ophthalmic Photography: Retinal Photography, Angiography, and Electronic Imaging, 2nd ed., Butterworth-Heinemann, Boston, 2001.

[23] R. H. Choplin, J. M. Boehme II and C. D. Maynard, "Picture archiving and communication systems: an overview", *Radiographics*, vol.12, no.1, pp. 127-129, 1992.

[24] H. B. Chawla, Ophthalmology: A symptom-based Approach, 3rd ed., Butterworth-Heinemann, Oxford, 1999.

[25] P. Frith, R. Gray, S. Maclennan, and P. Ambler, The Eye in Clinical Practice, 2nd ed., Blackwell Science, HongKong, 2001.

[26] J. M. Tielsch, J. Katz, K. Singh, and H. A. Quigley et. al., "A population-based evaluation of glaucoma screening: The Baltimore eye survey", *American Journal of Epidemiology*, vol. 134, no. 10, pp. 1102–1110, 1991.

[27] G. Vafidis and S. Levin, "Clinical Review – Glaucoma", website access at: http://www.gponline.com/Clinical/article/1157782/clinical-review-glaucoma/, 2014.

[28] D. Edgar and A. Rudnicka, Glaucoma identification & co-management, Butterworth Heinemann, USA, 2007.

[29] C. Duanggate, B. Uyyanonvara. "A review of automatic Drusen detection and segmentation from retinal image", 3rd International Symposium on Biomedical Engineering, volume: 1, issue: d, pp.222-225, 2008.

[30] NHS, "Macular degeneration", Website access at: http://www.nhs.uk/conditions/macular-degeneration/Pages/Introduction.aspx, 2014.

[31] Eye Diseases Prevalence Research Group, "Prevalence of age-related macular degeneration in the united states", *Archives of ophthalmology*, vol. 122, no. 4, pp. 564–572, 2004.

[32] R. Priya , P. Aruna, "Automated Diagnosis Of Age-Related Macular Degeneration From Color Retinal Fundus Images", 3rd International Conference on Electronics Computer Technology (ICECT), vol.2, pp. 227 – 230, 2011.

[33] WillsEye Hospital, “Age-related Macular Degeneration (AMD)”, website access at: http://www.willseye.org/health-library/age-related-macular-degeneration-amd, 2014.

[34] A. R. Chowdhury and S. Banerjee, “Cellular Neural Network based Algorithm in Image Analysis of Age Related Macular Degeneration”, in IET Chennai 3rd International conference on Sustainable Energy and Intelligent Systems *(SEISCO*N 2012), pp.1-4, 2012.

[35] R. Priya, P. Aruna, “Automated Diagnosis Of Age-Related Macular Degeneration From Color Retinal Fundus Images”, in 3rd international conference on Electronics Computer Technology (*ICECT*), vol. 2, pp.227-230, 2011.

[36] P. Burlina, D.E. Freund, et al., “Automatic Screening of Age-Related Macular Degeneration and Retinal Abnormalities”, in 33rd Annual International Conference of the IEEE EMBS, pp.3962-3966, 2011.

[37] K. Rapantzikos, M. Zervakis, K. Balas, “Detection and segmentation of drusen deposits on human retina: Potential in the diagnosis of age-related macular degeneration”, *Medical image analysis*, vol. 7, issue 1, pp. 95-108, 2003.

[38] R. Jana, A. R. Chowdhury, and C. Ray, “Automatic Drusen Detection and Area Calculation from Color Retinal Images”, *International Journal of Engineering Research & Technology (IJERT)*, vol.1, issue 6, 2012.

[39] A. Bhuiyan, C. Karmakar, et. al., “Drusen Quantification for Early Identification of Age Related Macular Degeneration (AMD) Using Color Fundus Imaging”, in 35th Annual International Conference of the IEEE EMBS, pp. 7392 – 7395, 2013.

[40] T. Y. Wong, A. Shankar, R. Klein, B. E. K. Klein, and L. D. Hubbard, “Prospective cohort study of retinal vessel diameters and risk of hypertension”, *BMJ*, vol. 329, pp. 799–800, 2004.

[41] Grosso A, Veglio F, Porta M, Grignolo FM and Wong TY. “Hypertensive retinopathy revisited: some answers, more questions”, *British Journal of Ophthalmology*, vol.89, pp. 1646-1654, 2005.

[42] A. D. Henderson, V. Biousse, N. J. Newman et al., “Grade III or Grade IV Hypertensive Retinopathy with severely elevated blood pressure”, *Western Journal of Emergency Medicine*, vol. 13, no.6, pp.529-534, 2012.

[43] WHO, “Definition and diagnosis of diabetes mellitus and intermediate hyperglycaemia”, website access: http://whqlibdoc.who.int/publications/2006/9241594934_eng.pdf, 2014.

[44] S. Wild, G. Roglic, A. Green, R. Sicree, H. King, “Global Prevalence of Diabetes: Estimates for the year 2000 and projections for 2030”, *Diabetes Care.*, vol. 27, pp.1047-1053, 2004.

[45] DHHS, “Summary health statistics for U.S. adults: National health interview survey, 2012”, *Vital and Health statistics*, Series 10, no. 260, 2014.

[46] J. Evans, “Causes of Blindness and Partial Sight in England and Wales 1990–1991”, in Studies on Medical and Population Subjects, vol. 57, 1988.

[47] C. Bunce, W. Xing and R. Wormald，“Causes of blind and partial sight certifications in England and Wales: April 2007–March 2008”, vol.24, no.11, pp.1692-1699, 2010.

[48] Prevent Blindness America, “vision problems in the U.S.”, website access at: http://www.visionproblemsus.org/diabetic-retinopathy/diabetic-retinopathy-by-age.html, 2014.

[49] L. Ferris, “how effective are treatment for diabetic retinopathy?”, JAMA, vol.269, pp.1290-1291,1993.

[50] Diabetic Retinopathy study, “photocoagulation treatment of proliferative diabetic retinopathy: the second report of diabetic retinopathy study findings”, *Ophthalmology*, vol. 85, pp.82-106, 1978.

[51] D. C. Klonoff and D. M. Schwartz, “An economic analysis of interventions for diabetes”, *Diabetes Care*, vol. 23, no. 3, pp. 390–404, 2000.

[52] D. Mcleod, “Reappraisal of the retinal cotton-wool spot a discussion paper”, *Journal of the Royal Society of Medicine*, vol.74, no.9, pp.682-686, 1981.

[53] R. Bock, and J. Meier, “Glaucoma risk index:Automated glaucoma detection from color fundus images”, *Medical Image Analysis*, vol. 14, pp. 471-481, 2010.

[54] K. P. Noronha et al. “Automated classification of glaucoma stages using higher order cumulant features”, *Biomedical Signal Processing and Control*, access at: http://dx.doi.org/10.1016/j.bspc.2013.11.006, 2013.

[55] J. Nayak et al. , “Automated Diagnosis of Glaucoma Using Digital Fundus Images”, *Journal of Medical Systems*, vol.33, pp.337-346, 2009.

[56] J. A. D. l. Fuente-Arriaga et al., “Application of vascular bundle displacement in the optic disc for glaucoma detection using fundus images”, *Computers in Biology and Medicine*, vol. 47, pp.27-35, 2014.

[57] M. S. Haleem, L. X. Han, et al. “Automatic extraction of retinal features from colour retinal images for glaucoma diagnosis: A review”, *Computerized Medical Imaging and Graphics*, vol. 37, pp.581-596, 2013.

[58] M. Zarbin and D. Chu, “Diagnostic and surgical techniques”, *survey of ophthalmology*, vol.52, no.6, pp.655-671, 2007.

[59] A. Bhuiyan, C. Karmakar, et al.,“Drusen quantification for early identification of age related macular degeneration (AMD) using color fundus imaging”, in 35rd Annual International Conference of the IEEE EMBS, pp:7392-7395, 2013.

[60] K. Rapantzikos, M. Zervakis, K. Balas, “Detection and segmentation of drusen deposits on human retina: Potential in the diagnosis of age-related macular degeneration”, *Medical Image Analysis*, vol.7, pp: 95-108, 2003.

[61] A. R. Chowdhury and S. Banerjee, “Cellular Neural Network based Algorithm in Image Analysis of Age Related Macular Degeneration”, in 3rd Inter. Conf. on SEISCON, pp.1-4, 2012.

[62] C. Kösea, U. Sevik, et al., “Automatic segmentation of age-related macular degeneration in retinal fundus images”, *Computers in Biology and Medicine*, vol.38, pp.611-619, 2008.

[63] P. Burlina, D.E. Freund, et al., “Automatic Screening of Age-Related Macular Degeneration and Retinal Abnormalities”, in 33rd Annual International Conference of the IEEE EMBS, pp.3962-3966, 2011.

[64] K. Narasimhan, V. C. Neha, and K.Vijayarekha, “Hypertensive retinopathy diagnosis from fundus images by estimation of AVR”, *Procedia engineering (in ICMOC)*, vol.38, pp. 980-993, 2012.

[65] M. Niemeijer et al., “Automated Measurement of the Arteriolar-to-Venular Width Ratio in Digital Color Fundus Photographs”, in IEEE transactions on medical imaging, vol. 30, no. 11, pp.1941-1950, 2011.

[66] D. Ortíz et al., “Support System for the Preventive Diagnosis of Hypertensive Retinopathy”, in 33rd Annual International Conference of the IEEE EMBS, pp.5649-5652,2010.

[67] W. Lotmar, A. Freiburghaus, and D. Bracher, “Measurement of vessel tortuosity on fundus photographs”, *Graefe's Archive for Clinical and Experimental Ophthalmology*, vol. 211, pp. 49–57, 1979.

[68] K. V. Chandrinos, M. Pilu, R. B. Fisher, and P. Trahanias, “Image processing techniques for the quantification of atherosclerotic changes,” presented at the MEDICON98, 1998.

[69] E. Grisan, M. Foracchia and A. Ruggeri, “A Novel Method for the Automatic Grading of Retinal Vessel Tortuosity”, in IEEE transactions on medical imaging, vol. 27, no. 3, pp. 310-319, 2008.

[70] B. Dupas, T. Walter, and A. Erginay et al., “Evaluation of automated fundus photograph analysis algorithms for detecting microaneurysms, haemorrhages and exudates, and of a computer-assisted diagnostic system for grading diabetic retinopathy”, *Diabetes & Metabolism*, vol.36, pp.213-220,2010.

[71] C. Sinthanayothin, J. F. Boyce, et al. “Automated localization of the optic disc, fovea, and retinal blood vessels from digital colour fundus images”, *British Journal of Ophthalmology*, vol.83, pp.902–10, 1999.

[72] R. Klein, et al., “Retinal Vascular Abnormalities in Persons with Type 1 Diabetes The Wisconsin Epidemiologic Study of Diabetic Retinopathy: XVIII”, *Ophthalmology*, vol.110, no.11, 2003.

[73] W. L. Yun, U. R. Acharya, and Y.V. Venkatesh, “Identification of different stages of diabetic retinopathy using retinal optical images”, *Information Sciences*, vol.178, pp.106-121, 2008.

[74] N. Larsen, J. Godt, and M. Grunkin, et al., “Automated Detection of Diabetic Retinopathy in a Fundus Photographic Screening Population”, *Investigative Ophthalmology & Visual Science*, vol. 44, no. 2, pp.767-771, 2003.

[75] D. Usher, M. Dumskyj, and M. Himaga, et al. “Automated detection of diabetic retinopathy in digital retinal images: a tool for diabetic retinopathy screening”, *Diabetic Medicine*, vol. 21, pp.84-90, 2003.

[76] T. Walter, P. Massin, and A. Erginay, et al. “Automatic detection of microaneurysms in color fundus images”, *Medical Image Analysis*, vol.11, pp.555-566, 2007.

[77] L. Giancardo, F. Meriaudeau, and T. P. Karnowski, et al., “Exudate-based diabetic macular edema detection in fundus images using publicly available datasets”, *Medical Image Analysis*, vol.16, pp.216-226, 2012.

[78] C.I. Sanchez, et al., “Retinal image analysis based on mixture models to detect hard exudates”, *Medical Image Analysing*, vol. 13, no. 4, p. 650-8. 2009.

[79] F. Zana and J. C. Klein, “A Multimodal Registration Algorithm of Eye Fundus Images Using Vessels Detection and Hough Transform”, in IEEE Transactions on Medical Imaging, vol. 18, pp. 419-428, 1999.

[80] N. Patton, et al., “Retinal image analysis: concepts, applications and potential”, *Progress in Retinal and Eye Research*, vol. 25, issue 1, pp. 99-127, 2006.

[81] M. Preethi, and R. Vanithamani, “Review of retinal blood vessel detection methods for automated diagnosis of Diabetic Retinopathy”, in International Conference on ICAESM., pp. 262 – 265, 2012.

[82] C. Kirbas, and F. K. H. Quek, “A Review of Vessel Extraction Techniques and Algorithms”, *ACM Computing Surveys (CSUR)*, vol. 36, Issue 2, pp. 81-121, 2004.

[83] K. Bühler, P. Felkel, and A.L. Cruz, "Geometric Methods for Vessel Visualization and Quantification - A Survey", in Geometric Modeling for Scientific Visualization, pp. 399-419, 2004.

[84] M. M. Fraz, et al., "Blood vessel segmentation methodologies in retinal images: a survey", *Computer Methods and Programs in Biomedicine*, vol. 108, issue 1, pp. 407-33, 2012.

[85] S. Chaudhuri, et al., “Detection of blood vessels in retinal images using two-dimensional matched filters”, in IEEE Transactions on Medical Imaging, vol. 8, no.3, pp.263-269, 1989.

[86] L. Gang, O. Chutatape, and S. Krishnan, “Detection and measurement of retinal vessels in fundus images using amplitude modified second-order Gaussian filter”, in IEEE Transactions on Biomedical Engineering, vol. 49, no. 2, pp. 168–172, 2002.

[87] M. Al-Rawi, M. Qutaishat, M. Arrar, “An improvement matched filter for blood vessel detection of digital retinal images”, *Computers in Biology and Medicine*, vol.37, pp.262–267, 2007.

[88] M. Cinsdikici, D. Aydin, “Detection of blood vessels in ophthalmoscope images using MF/ant (matched filter/ant colony) algorithm”, *Computer Methods and Programs in Biomedicine*, vol. 96, pp. 85–95, 2009.

[89] B. Zhang and L. Zhang et al., “Retinal vessel extraction by matched filter with first-order derivative of Gaussian”, *Computers in Biology and Medicine*, vol.40 no.4, pp.438-445, 2010.

[90] A. Hoover, V. Kouznetsova, M. Goldbaum, “Locating blood vessels in retinal images by piecewise threshold probing of a matched filter response”, in IEEE Transactions on Medical Imaging, vol. 19, no.3, pp.203–210, 2000.

[91] C. H. Wu, G. Agam, P. Stanchev. “A general framework for vessel segmentation in retinal images”, in Proceedings of CIRA, pp.37-42, 2007.

[92] Q. Li, J. You, and D. Zhang, "Vessel segmentation and width estimation in retinal images using multiscale production of matched filter responses", *Expert Systems with Applications*, vol. 39, issue. 9, pp. 7600-7610, 2012.

[93] J. Odstrcilik, et al., “Retinal vessel segmentation by improved matched filtering: evaluation on a new high-resolution fundus image database”, *IET Image Process*, vol. 7, issue 4, pp.373-383, 2013.

[94] P. Echevarria, T. Miller and J. O'Meara, “Blood Vessel Segmentation in Retinal Images”, website access at: http://robots.stanford.edu/cs223b04/project_reports/P14.pdf, 2004.

[95] D. Wu, et al., “On the adaptive detection of blood vessels in retinal images”, in IEEE Transactions on Biomedical Engineering, vol. 53, no. 2, pp. 341–343, 2006.

[96] Y. Tolias, S.M. Panas, “A fuzzy vessel tracking algorithm for retinal images based on fuzzy clustering”, in IEEE Transactions on Medical Imaging, vol.17, no.2, pp.263–273, 1998.

[97] O. Chutatape, L. Zheng, S.M. Krishnan, “Retinal blood vessel detection and tracking by matched Gaussian and Kalman filters”, in: Proc. of 20th Annu. Int. Conf. IEEE Eng Med. Biol., pp. 3144–3149, 1998.

[98] M. Vlachos and E. Dermatas, “Multi-scale retinal vessel segmentation using line tracking”, *Computerized Medical Imaging and Graphics*, vol. 34, issue 3, pp. 213-227, 2010.

[99] K. K. Delibasis, et al., “Automatic model-based tracing algorithm for vessel segmentation and diameter estimation”, *Computer Methods and Programs in Biomedicine*, vol. 100, issue 2, pp. 108-22, 2010.

[100] S. You, et al. “Principal Curved Based Retinal Vessel Segmentation towards Diagnosis of Retinal Diseases”, in IEEE inter. Conf. on Health. infor., Imag. and syst. Bio., pp:331-337, 2011.

[101] H. Ocbagabir, et al., “A novel vessel segmentation algorithm in color images of the retina”, in IEEE Long Island Systems on App. and Tech. Confe. (LISAT), pp. 1 – 6, 2013.

[102] J. J. Staal, et al., “Ridge based vessel segmentation in color images of the retina”, in IEEE Transactions on Medical Imaging, pp. 501–509, 2004.

[103] J. V. B. Soares, et al., “Retinal vessel segmentation using the 2D Gabor wavelet and supervised classification”, in IEEE Transactions on Medical Imaging, vol. 25, no. 9, pp. 1214–1222, 2006.

[104] E. Ricci and R. Perfetti, Retinal blood vessel segmentation using line operators and support vector classification, in IEEE Transactions on Medical Imaging, vol.26, no.10, pp. 1357 –1365, 2007.

[105] S. H. Rezatofighi, A. Roodaki, and H. A. Noubari, “An Enhanced Segmentation of Blood Vessels in Retinal Images Using Contourlet”, in IEEE EMBS Conference, pp.3530-3533, 2008.

[106] M. S. Moin, H. R. Tavakoli, and A. Broumandnia, “A new retinal vessel segmentation method using preprocessed Gabor and local binary patterns”, Machine Vision and Image Processing (*MVIP*), pp:1 – 6, 2010.

[107] C.A. lupascu, D. Tegolo and E. Trucco, “FABC: Retinal vessel segmentation using adaboost”, in IEEE Transactions on Info. Tech. in Biomed., vol. 14, no. 5, pp. 1267 – 1274, 2010.

[108] D. Marín, et al., “A New Supervised Method for Blood Vessel Segmentation in Retinal Images by Using Gray-Level and Moment Invariants-Based Features”, in IEEE Transactions on Medical Imaging, vol.30, pp: 146 – 158,2011.

[109] D. Selvathi and P. Lalitha Vaishnavi, “Gabor Wavelet based Blood Vessel Segmentation in Retinal images using Kernel Classifiers”, in international conference on ICSCCN, pp. 830-835, 2011.

[110] M.M. Fraz, P. Remagnino, et al., “A Supervised Method for Retinal Blood Vessel Segmentation Using Line Strength, Multiscale Gabor and Morphological Features”, in IEEE international conference on ICSIPA, pp.410-415, 2011.

[111] A. P. Condurache and A. Mertins, “Segmentation of retinal vessels with a hysteresis binary-classification paradigm”, *Computerized Medical Imaging and Graphics*, vol.36, no.4, pp.325-335, 2012.

[112] S. Salem, N. Salem, A. Nandi, “Segmentation of retinal blood vessels using a novel clustering algorithm (RACAL) with a partial supervision strategy”, *Medical and Biological Engineering and Computing*, vol. 45, pp.261–273, 2007.

[113] G.B. Kande, P.V. Subbaiah, T.S. Savithri, “Unsupervised fuzzy based vessel segmentation in pathological digital fundus images”, *Journal of Medical Systems*, vol. 34, pp. 849–858, 2010.

[114] W. S. Oliveira, T. I. Ren and G. D. C. Cavalcanti, “An Unsupervised Segmentation Method for Retinal Vessel Using Combined Filters”, in IEEE 24th International Conference on Tools with Artificial Intelligence, pp.750-756,2012.

[115] Y. F. Wang, G. R. Ji, et al., “Retinal vessel segmentation using multi-wavelet kernels and multi-scale hierarchical decomposition”, *Pattern Recognition*, vol. 46, pp.2117-2133, 2013.

[116] M. Kass, A. Witkin, D. Terzopoulos, “Snakes: active contour models”, *International Journal of Computer Vision*, vol.1, Issue 4, pp.321-331, 1988.

[117] S. Osher and J. Sethian, “Fronts Propagating with curvature-dependent speed: algorithms based on Hamilton-Jacobi formulations”, *Journal of Computational Physics*, vol. 79, pp.12-49, 1988.

[118] L. Wang, A. Bhalerao, and R. Wilson, “Analysis of Retinal Vasculature Using a Multiresolution Hermite Model”, In IEEE Transactions on Medical Imaging, vol. 26, no. 2, 2007.

[119] B. S. Y. Lam, Y. S. Gao, and A. W. Liew, “General Retinal Vessel Segmentation Using Regularization-Based Multiconcavity Modeling”, In IEEE Transactions on Medical imaging, vol. 29, no. 7, 2010.

[120] L. Espona, M.J. Carreira, M. Ortega, M.G. Penedo, “A snake for retinal vessel segmentation”, in Proceedings of the 3rd Iberian conference on Pattern Recognition and Image Analysis, Part II, pp.178-185, 2007.

[121] B. Al-Diri, A. Hunter, and D. Steel, “An Active Contour Model for Segmenting and Measuring Retinal Vessels”, In IEEE transaction on medical imaging, vol. 28, no. 9, pp. 1488-1497, 2009.

[122] Z. L. Szpak and J. R. Tapamo, “Automatic Retinal Vessel Segmentation”, in proceedings of PRASA, pp. 51-55, 2007.

[123] J. Ng, S.T. Clay, and S.A. Barman, et al., “Maximum likelihood estimation of vessel parameters from scale space analysis”, *Image and Vision Computing*, vol. 28, issue 1, pp. 55-63, 2010.

[124] Y. Shi, and W. C. Karl, “A fast level set method without solving PDEs”, in IEEE International Conference on Acoustics, Speech and Signal Processing, vol. 2, pp.97-100, 2005.

[125] F. Zana and J.-C. Klein, “Segmentation of vessel-like patterns using mathematical morphology and curvature evaluation”, IEEE Transactions on Image Processing, vol. 10, pp. 1010-1019, 2001.

[126] A. M. Mendonca, A. Campiho, “Segmentation of retinal blood vessels by combining the detection of centrlines and morphological reconstruction”, In IEEE transaction on medical imaging, vol. 25, no. 9, pp: 1200-1213, 2006.

[127] M. S. Miri and A. Mahloojifar, “Retinal Image Analysis Using Curvelet Transform and Multistructure Elements Morphology by Reconstruction”, In IEEE Transactions on Biomedical engineering, vol. 59, no. 5 , pp. 1183-1192, 2011.

[128] A. G. Salazar-Gonzalez, Y. M. Li and X. H. Liu, “Retinal blood vessel segmentation via graph cut”, in 11th International Conference on Control Automation Robotics & Vision, pp. 225 – 230, 2010.

[129] W. Cai and A. C. S. Chung, “Multi-resolution vessel segmentation using normalized cuts in retinal images”, In Proceedings of International Conference on Medical Image Computing and Computer-Assisted Intervention, vol.1, pp.928–936, 2006.

[130] A. H. Asad, E. El amry, A. E. Hassanien, “Retinal vessels segmentation based on water flooding Model”, in 9th international Computer Engineering conference (ICENCO), pp. 43-48, 2013.

[131] T. Fawcett, “An introduction to ROC analysis”, *Pattern Recogn. Lett.*, vol. 27, no. 8, pp. 861–874, 2006.

[132] Image Sciences institute, “DRIVE: Digital Retinal Images for Vessel Extraction”, website access at: http://www.isi.uu.nl/Research/Databases/DRIVE/, access in 2012.

[133] Shiley Eye Center, “Structured Analysis of the Retina”, website access at: http://www.ces.clemson.edu/~ahoover/stare/, access in 2010.

[134] J. R. Smith, “Integrated Spatial Feature Image Systems: Retrieval, Analysis and Compression”, Ph.D. thesis, School of Arts and Sciences, Columbia University, 1997.

[135] Y. N. Deng, B. S. Manjunath and H. Shin, “Color Image Segmentation”, Proc. of IEEE Computer Society Conf. on Computer Vision and Pattern Recognition, vol. 2, pp.446-451, 1999.

[136] M. R. Blas, M. Agrawal, et al. “Fast color/texture segmentation for outdoor robots”, IEEE International Conference on Intelligent Robots and Systems, pp. 4078-4085, 2008.

[137] M. F. A. Fauzi and P. H. Lewis, “Automatic texture segmentation for content-based image retrieval application”, *Pattern Analysis and Applications*, vol. 9, issue 4, pp. 307-323, 2006.

[138] W. D. He, I. Muhimmah, et al., “Mammographic segmentation based on texture modelling of Tabár mammographic building blocks”, *Lecture Notes in Computer Science*, vol. 5116, pp. 17-24, 2008.

[139] M. Varma and A. Zisserman. “Unifying statistical texture classification frameworks”, *Image and Vision Computing*, vol. 22, pp.1175 – 1183, 2004.

[140] D. A. Adjeroh, U. Kandaswamy, J. V. Odom, “Texton-based segmentation of retinal vessels”, *J. Opt. Soc. Am. A Opt. Image. Sci. Vis.*, vol. 24, issue 5, pp. 1384-1393, 2007.

[141] T. R. Reed and J.M.H. Dubuf, “A review of recent texture segmentation and feature extraction techniques”, *CVGIP: Image Understanding*, vol. 57, issue 3, pp. 359-372, 1993.

[142] A. Materka, M. Strzelecki, “Texture Analysis Methods: A Review”, COST B11 Report, Technical University of Lodz, 1998.

[143] M. Tuceryan and A. K. Jain, “Texture Analysis”, in The handbook of Pattern Recognition and Computer Vision (2nd Edition), by C. H. Chen, L. F. Pau, P. S. P. Wang (Eds.), World Scientific Publishing Co., 1998.

[144] X. H. Xie, “A Review of Recent Advances in Surface Defect Detection using Texture analysis Techniques”, *Electronic Letters on Computer Vision and Image Analysis*, vol. 7, no. 3, pp.1-22, 2008.

[145] A.Dixit and N. P. Hegde, “Image texture analysis-survey”, in Third international conference on ACCT, pp. 69-76, 2013.

[146] G. H. Srinivasan and G. Shobha, “Statistical texture analysis”, in Proc. of word acade. of sci., eng. and tech., vol. 36, pp.1264-1269, 2008.

[147] J. G. Zhang, T. Tan, “Brief review of invariant texture analysis methods”, *Pattern Recognition*, vol.35, pp. 735-747, 2002.

[148] W. H. Nailon, “Texture analysis methods for medical image characterisation”, in Biomedical imaging, by Y. X. Mao (Eds.), pp. 75-100, InTech, 2010.

[149] A. Kassner and R. E. Thornhill, “Texture analysis: a review of neurologic MR imaging application”, *AJNR Am J Neuroradiol*, vol. 31, no. 5, pp. 809-816, 2010.

[150] L. S. Davis, “Image texture analysis techniques-A survey”, in Digital image processing, by J. C. Simon and R. M. Haralick (Eds), D. Reidel, pp. 189-201,1980.

[151] B. Julesz, E. N. Gilbert, et al. “Inability of humans to discriminate between visual textures that agree in second-order statistics - revisited”, *Perception*, vol. 2, pp. 391-405, 1973.

[152] B. Julesz, “Experiments in the visual perception of texture”, *Scientific American*, vol. 232, pp. 34-43, 1975.

[153] S. C. Zhu, C. E. Guo, et al., “What are textons”, *International Journal of computer vision*, vol. 62, pp.121-143, 2005.

[154] T. Leung and J. Malik, “Representing and Recognizing the Visual Appearance of Materials using Three-dimensional Textons”, *International Journal of computer vision* , vol. 43, no. 1, pp. 29-44, 2001.

[155] J. Malik, S. Belingie, et al., “Textons, Contours and Regions: Cue Integration in Image Segmentation”, in Proc. IEEE Intl. Conf. Computer Vision, pp.918-925, 1999.

[156] Y. Chen and E. Dougherty, “Grey-Scale Morphological Granulometric Texture Classification”, *Optical Engineering*, vol. 33, no. 8, pp.2713-2722, 1994.

[157] D. Wang, H. C. Veronique, et al. “Texture classification and segmentation based on iterative morphological decomposition”, *J. Visual Comm. and Image Rep.*, vol.4, no. 3, pp. 197-214, 1993.

[158] W. K. Lam, C. K. Li, “Rotated texture classification by improved iterative morphological decomposition”, in IEE Proc. On Vis., Imag. and Sig. Proc., vol. 144, Issue 3, pp. 171-179, 2002.

[159] B. A. Olshausen and D. J. Field, “Sparse coding with an overcomplete basis set: A strategy employed by V1”, *Vision Res.*, vol. 37, no. 23, pp. 3311-3325, 1997.

[160] J. C. Mao and A. K. Jain, “Texture classification and segmentation using multiresolution simultaneous autoregressive models”, *Pattern Recognition*, vol. 25, Issue 2, pp. 173-188, 1992.

[161] O. Alata, C. Ramananjarasoa, “Unsupervised textured image segmentation using 2-D quarter plane autoregressive model with four prediction support”, *Pattern Recognition Letters*, vol. 26, issue 8, pp. 1069-1081, 2005.

[162] C. Cariou and K. Chehdi, “Unsupervised texture segmentation/classification using 2-D autoregressive modelling and the stochastic expectation maximization algorithm”, *Pattern Recognition Letters*, vol. 29, issue 7, pp.905-917, 2008.

[163] B. B. Mandelbrot, The Fractal Geometry of Nature, W. H. Freeman, San Francisco, 1982.

[164] A. P. Pentland, “Fractal-based description of natural scenes”, in IEEE trans. on Pattern Anal.and Mach. Intell., vol. 6, no. 6, pp. 661-674, 1984.

[165] P. Shanmugavadivu and V. Sivakumar, “Fractal Dimension Based Texture Analysis of Digital Images”, *Procedia Engineering*, vol. 38, pp.2981-2986, 2012.

[166] H. W. Deng, D. A. Clausi, “Unsupervised image segmentation using a simple MRF model with a new implementation scheme”, *Pattern Recognition*, vol. 37, issue 12, 2004.

[167] S. Z. Li, Markov Random Field Modeling in Computer Vision, Springer, 2001.

[168] Z. Kato, T. C. Pong, “A Markov random field image segmentation model for color textured images”, *Image and Vision Computing*, vol. 24, issue 10, pp. 1103–1114, 2006.

[169] M. Varma and A. Zisserman, “Texture Classification: Are Filter Banks Necessary?”, In Proceedings of the IEEE Conference on Computer Vision and Pattern Recognition, vol. 2, pp. 691-698, 2003.

[170] N. Aggarwal and R. K. Agrawal, “First and Second order statistics features for cassificaiton of magnetic resonance brain images”, *Journal of signal and information processing*, vol. 3, no. 2, pp. 146-153, 2012.

[171] R. Haralick, K. Shanmugan, and I. Dinstein, “Textural features for image classification”, in IEEE trans. On sys., man, and Cybernetics, vol. 3, no. 6, pp. 610-621, 1973.

[172] M. Bartels and H. Wei, et al. “Wavelet packets and co-occurrence matrices for texture-based image segmentation”, in IEEE conference on AVSS, pp. 428-433, 2005.

[173] B. S. Marron, “co-occurrence matrix and fractal dimension for image segmentation”, *Revista de Matemática: Teoría y Aplicaciones*, vol. 19, no.1, pp. 49-63, 2012.

[174] J. Besag, “Spatial Interaction and the Statistical Analysis of Lattice Systems,” *Journal of Royal Statistical Society. Series B (Methodological)*, vol.36, no. 2, pp. 344-348, 1974.

[175] D. Martin, C. Fowlkes, J. Malik. "Learning to Detect Natural Image Boundaries Using Local Brightness, Color and Texture Cues", In IEEE Transactions on Pattern Analysis and Machine Intelligence, vol. 26, no. 1, pp.530-549, 2004.

[176] M. Varma and A. Zisserman, “A Statistical Approach to Texture Classification from Single Images”, *International Journal of Computer Vision*, vol. 62, no. 1-2, pp. 61-81, 2005.

[177] R. De Valois, D. Albrecht, et al., “Spatial-frequency selectivity of cells in macaque visual cortex”, *Vision Research*, vol. 22, pp. 545-559, 1982.

[178] R. L. De Valois and K. K. De Valois, Spatial vision, Oxford University Press., New York, 1988.

[179] F. W. Campbell and J. G. Robson, “Application of Fourier Analysis to the Visibility of Gratings,” *Journal of Physiology*, vol. 197, pp. 551-566, 1968.

[180] D. Gabor, “Theory of communication”, *Journal of the Institute of Electrical Engineers*, vol. 93, pp.429- 457, 1946.

[181] J. G. Daugman, “Uncertainty relation for resolution in space, spatial frequency, and orientation optimized by two-dimensional visual cortical filters”, *Journal of the Optical Society of America*, vol. 2, no. 7, pp.1160–1169, 1985.

[182] C, Schmid, “Constructing models for content-based image retrieval”. In Proceedings of the IEEE Conference on Computer Vision and Pattern Recognition, vol. 2, pp. 39-45, 2001.

[183] T. Ojala, M. Pietikäinen, and D. Harwood, “A comparative study of texture measures with classification based on featured distributions,” *Pattern recognition*, vol. 29, no. 1, pp. 51–59, 1996.

[184] T. Ojala, M. Pietikäinen and T. Mäenpää, “Multiresolution Gray-scale and Rotation Invariant Texture Classification with Local Binary Patterns”, in IEEE Transaction on Pattern Analysis and Machine Intelligence, vol. 24, no. 7, pp. 971-987, 2002.

[185] M. Pietikäinen, T. Ojala and Z. Xu, “Rotation invariant texture classification using feature distributions”, *Pattern Recognition*, vol. 33, pp.43–52, 2000.

[186] D. Connah and G. D. Finlayson, “ Using Local Binary Pattern Operators for Colour Constant Image Indexing”, In 3rd European Conference on Colour in Graphics, Imaging and Vision, 2006.

[187] S. Liao and A. Chung, “Texture classification by using advanced local binary patterns and spatial distribution of dominant patterns”, in IEEE International Conference on Acoustics, Speech and Signal Processing, vol. 1, pp. I-1221-I-1224, 2007.

[188] C. He, T. Ahonen and M. Pietikäinen, “A Bayesian Local Binary Pattern Texture Descriptor”, in 19th International conference on Pattern Recognition, pp. 1-4, 2008.

[189] A. Suga and K. Fukuda, et al., “Object Recognition and Segmentation Using SIFT and Graph Cuts”, in 19th International Conference on Pattern Recognition, pp. 1-4, 2008.

[190] J. Sobek, D. Cetnarowicz, and A. Dabrowski, “Fingerprint Classification using Scale-invariant Feature Transform”, in Signal Processing Algorithms, Architectures, Arrangements and Applications Conference Proceedings, pp. 1-6, 2011.

[191] P. Kamencay, M. Breznan, et al., “Improved Face Recognition Method based on Segmentation Algorithm using SIFT-PCA”, in 35th International Conference on Telecommunications and Signal Processing, pp. 3-4, 2012.

[192] T. Chanwimaluang and G. L. Fan, “An efficient algorithm for extraction of anatomical structures in retinal images”, in International Conference on Image Processing, vol.1, pp. 1093-1096, 2003.

[193] S. S. Parvathi and N. Devi, “Automatic Drusen detection from colour retinal images”, in international conference on computational intelligence and multimedia application, pp. 337-381, 2007.

[194] M.C. Morrone and R. Owens, “Feature detection from local energy”, *Pattern Recognition Letters*, vol. 1, pp. 103–113, 1987.

[195] D. J. Field, “Relation between the statistics of natural images and the response properties of cortical cells”, *Journal of the Optical Society of America A*, vol. 4, no. 12, pp.2379-2394, 1987.

[196] N. R. Pal and S. K. Pal, “Entropic thresholding”, *Signal processing*, vol. 16, pp. 97.108, 1989.

[197] D. A. Adjeroh et al. “Texton-based segmentation of retinal vessels.” *Journal of the Optical Society of America*, vol. 24, issue 5, pp.1384-1393, 2007.

[198] X. H. Gao, A. Bharath, A. Stanton, A. Hughes, N. Chapman, and S. Thom, “A method of vessel tracking for vessel diameter measurement on retinal images,” in Proceedings of IEEE International Conference on Image Processing, vol. 2, pp. 881–884, 2001.

[199] X. Li et al. “Estimating the ground truth from multiple individual segmentations incorporating prior pattern analysis with application to skin lesion segmentation”, in Proc. IEEE Int. Symposium on Biomedical Imaging: From Nano to Micro”, pp.1438-1441, 2011.

[200] N. Petkov, “Biologically motivated computationally intensive approaches to image pattern recognition”, *Future Gen. Comput. Syst.*, vol. 11, pp. 451–465, 1995.

[201] N. Petkov, P. Kruizinga, “Computational models of visual neurons specialized in the detection of periodic and aperiodic oriented visual stimuli: Bar and grating cells”, *Biol. Cybern.*, vol. 76, pp. 83–96, 1997.

[202] D. G. Lowe, “Distinctive Image Features from Scale-Invariant Keypoints”, *International Journal of Computer Vision*, vol. 60, no. 2, pp. 91-110, 2004.

[203] T. Fawcett, “An introduction to ROC analysis”, *Pattern Recognition Letters*, vol. 27, pp. 861-874, 2006.

[204] M. Varma and A. Zisserman, “Classifying images of materials: Achieving viewpoint and illumination independence”, in Proceedings of the 7th European Conference on Computer Vision, vol. 3, pp. 255–271, 2002.

[205] S. G. Mallat, “A theory for multiresolution signal decomposition: The wavelet representation”, *IEEE Transactions on Pattern Analysis and Machine Intelligence*, vol. 11, no. 7, pp. 674–693, 1989.

[206] T. Chang and C.-C. J. Kuo. Texture analysis and classification with tree-structured wavelet transform. *IEEE Transactions on Pattern Analysis Machine Intelligence*, vol. 2, no. 4, pp. 429–441, 1993.

[207] M. Unser. “Texture classification and segmentation using wavelet frames”, *IEEE Transactions on Image Processing*, vol. 4, no. 11, pp. 1549–1560, 1995.

[208] R. Porter and N. Canagarajah, “A Robust Automatic Clustering Scheme for Image Segmentation Using Wavelets”, *IEEE Transactions on Image Processing*, vol. 5, no. 4, pp. 662-665, 1996.

[209] D. Tsai and B. Hsiao. “Automatic surface inspection using wavelet reconstruction”, *Pattern Recognition*, vol. 34, no. 6, pp. 1285–1305, 2001.

[210] S. Glock, E. Gillich, J. Schaede, V. Lohweg, “Feature Extraction Algorithm for Banknote Textures Based on Incomplete Shift Invariant Wavelet Packet Transform”, *Lecture Notes in Computer Science*, vol. 5748, pp. 422-431, 2009